Generalizable Methodology for Measurement and Analysis of Nutritional Intake

Sepehr Makhsous

A dissertation

submitted in partial fulfillment of the

requirements for the degree of

Doctor of Philosophy

University of Washington
2020

Reading Committee:

Alexander V. Mamishev (Chair)

Igor V. Novosselov (Chair)

Payman Arabshahi

Program Authorized to Offer Degree:

Electrical and Computer Engineering

University of Washington

Abstract

Generalizable Methodology for Measurement and Analysis of Nutritional Intake

Sepehr Makhsous

Chair of the Supervisory Committee:
Alexander V. Mamishev
Department of Electrical and Computer Engineering
Igor V. Novosselov
Department of Mechanical Engineering

According to the American Cancer Society (ACS), in 2018, more than 17 million people were diagnosed with cancer, and over 9 million patients died of cancer. Recent studies show that diet and lifestyle were two of the most common risk factors for related diseases and cancer. In Epidemiologic studies, enhanced dietary measurement tools are used to collect and analyze nutritional data. Traditional nutritional measurement methods include manual measurements and self-reporting, which introduce problems such as: 1) misreporting, 2) human error, and 3) involuntarily change of dietary habit. Recent advancements in sensing technologies have allowed for the development of various 3D measurement techniques for different applications. However, epidemiologists are still using self-reporting systems rather than automated 3D measurement tools, which demonstrates that there is significant room for improvement in this field. The volumetric measurement of a 3D object requires an accurate depth calculation using reference-based or depth

sensing estimation techniques. This dissertation is a study of the design, modeling, and integration of a 3D measurement system based on the structured light system (SLS) theory. The system was designed, developed, and evaluated in dietary assessment applications, such as cancer and diabetes, using both a customized 3D scanner and a commercial off the shelf (COTS) depth sensor. The participants were selected randomly to test the system in different use-cases. When compared to similar systems, the results showed an average increase in accuracy of 30% and a reduction in measurement time by more than a factor of three. Based on the results and feedback from the researchers and users, the use of low-cost depth sensors in 3D measurement have drastically improved the quality of automated nutritional analysis. In addition to dietary assessment applications, the system was further developed and tested in other epidemiological fields, such as wound care management, air quality monitoring, and environmental disease tracking.

TABLE OF CONTENTS

LIST OF FIGURES

LIST OF TABLES

ACKNOWLEDGMENTS

Over the past eight years, I have been blessed to have the opportunity to conduct part of my undergraduate and graduate research under the direction of Professor Alexander Mamishev, Professor Alexander Mamishev, who is the director of the Sensors, Energy, and Automation Laboratory (SEAL) at the University of Washington's Department of Electrical and Computer Engineering, and Professor Igor Novosselov at the Department of Mechanical Engineering. I would like to thank my advisors for always pushing and demanding the best in many different aspects of my work. I would also like to thank them for supporting me in pursuing my interest in entrepreneurship by completing a concurrent master's degree in business and association (MBA). Also, I would like to thank Professor Igor Novosselov for introducing me to the field of aerosol research and giving me the opportunity, as well as the resources, to work with his team at the Department of Mechanical Engineering.

I would also like to express my gratitude to my thesis committee members, Dr. Payman Arabshahi, Dr. Shwetak Patel, Dr. Scott Meschke, and Dr. Edmund Seto for their contributions of advice and time. I would also like to thank Professor Arabshahi for all his support, guidance, and advice in both my Engineering and Entrepreneurship studies.

DEDICATION

This thesis is dedicated to my parents Sorour Abdi and Mojtaba Makhsoss

Chapter 1. INTRODUCTION

The work presented in this thesis is motivated by the growing concerns regarding health problems related to diet, such as cancer and diabetes [1]. It is estimated that the number of new cancer cases will increase to 30 million annually by 2040 [2]. Diabetes is a global health issue, with an estimated 30.3 million people affected in the United States alone [3, 4]. Current nutritional research is hindered by the low accuracy of traditional dietary intake estimation methods used for portion size assessment. Improved dietary assessment techniques are necessary for epidemiological studies that investigate the relationship between diet and disease [5]. This dissertation is a study of the design, modeling, and integration of a small-scale smartphone add-on, as well as an image processing algorithm for measuring the nutritional intake of a given meal. In addition to dietary assessment, the system was also tested for post-operative wound case management. This work is based on publications by the author [6-10].

1.1 INTRODUCTION TO 3D MEASUREMENT

3D Measurement is a visual-based measurement (VBM) technique which uses a visual sensor and 3D reconstruction algorithm to calculate volume, dimensions, and surface texture. 3D modeling is done in two standard methods, single-view and multi-view [11, 12]. A single-view method uses a single image of an object and a reference point to reconstruct the 3D image, and a multi-view method uses a set of images covering a 360-degree view of an object.

Recently, more advanced and sophisticated methods propose using sensors, high-quality cameras, and image processing to reduce user burdens and increase the accuracy of the measurements. The recent improvements to mobile devices and their growing infrastructure has allowed researchers to use smartphones as their primary recording tool, especially due to the

smartphone's accessibility and convenience of recording information. These methods generally estimate the volume of the meal using 3D modeling. Regardless of the 3D reconstruction approach, to calculate nutritional intake, it is required to calculate the volumetric information of the object.

1.2 Introduction to Dietary Measurement Techniques

Enhanced dietary assessment techniques are critical for maintaining a healthy living for dietary disease-related patients. Moreover, hospitals must monitor their diabetic patients' food intake to prescribe an exact amount of insulin. Malnutrition is also a long-standing issue for hospitalized patients; up to 50% of patients are diagnosed with it nationwide. Malnutrition significantly increases patient mortality, the duration of the hospital stay, and medical costs [13].

Considerable work has been accomplished in the field of dietary intake measurement and calculation. Some of the methods are well established in the field of nutritional research, such as 24-Hour Recall (24HR) [14]. 24HR is a questionnaire that enables users to record detailed information about their dietary intake.

Despite current technological advancements, current dietary assessment methods are still predominantly inaccurate. Lack of precision in estimating energy intake and, more specifically, portion size has hindered nutritional research [15]. This dissertation describes an innovative approach to calculating an amount of food using multi-view 3D reconstruction while addressing volumetric measurements using a novel image processing algorithm.

1.3 Advantages and Disadvantageous of Dietary Measurements for Nutritional Assessment

Nutritional assessment is of keen interest to both research and industry. Advanced dietary measurement techniques can help improve epidemiological studies in cancer, diabetes, and

obesity. Recently, there has been considerable work done in the field of dietary analysis that introduces the use of integrated sensors instead of traditional paper-based methods. The discussion below reviews the major advantages and disadvantages of using advanced dietary measurement methodologies in nutritional assessment.

1.3.1 Advantages of Dietary Measurements for Nutritional Assessment

Complete nutritional intake information: One of the main advantages of using dietary measurements is collecting the exact consumed nutrition directly from the user. Accurate nutritional intake measurement allows researchers to conduct large scale studies by providing dietary assessment tools to subjects for self-measurement while maintaining the requirements of a scientific study [16].

Dietary intake monitoring and analysis: The ability to share dietary intake with a physician or a nutritionist is a crucial step, specifically for patients who suffer from cancer, diabetes, allergies, and heart disease. The use of dietary assessment allows for constant monitoring of patients' nutritional intake outside of the hospital environment.

Reducing the duration of the patient's hospital stay: Enhanced dietary assessment techniques are critical for maintaining a healthy living for an admitted patient. Moreover, hospitals must monitor their patients' food intake to prescribe an exact amount of medicine. Malnutrition is also a long-standing issue for hospitalized patients and, nationwide, up to 50% of patients are diagnosed with it. Malnutrition greatly increases patient mortality, the duration of the hospital stay, and medical costs [13].

1.3.2 Disadvantages of Dietary Measurements for Nutritional Assessment

User error: User error is one of the main issues when using dietary measurements in nutritional assessment. Most methods require users to enter all ingredients for any meal, including

the exact weight of each food item. However, this is a complicated process, and the majority of the users make many mistakes during their calculations [17]. A majority of dietary measurement techniques require estimation either from the user or automation. Researchers can only rely on the information reported by the users, which affects the overall results of any study.

Change of dietary habits: In most cases, users often change the way they eat when they are using dietary measurements, which no longer reflects their "typical diet" [18]. Some dietary measurement tools require the user, after a training process, to measure their dietary intake manually and write down all the information in a food diary. However, due to the amount of work, users tend to change their diet to reduce the burden of recording time. The change of the user's eating habits introduces the inconsistency of data and misrepresentation of dietary patterns.

1.4 Scientific and Engineering Challenges

The research work presented in this thesis overcomes several scientific and engineering challenges, which can be classified into several categories detailed below.

1.4.1 3D Reconstruction with Accurate Depth Measurement

One of the main challenges in 3D reconstruction-based measurement is obtaining the depth analysis from a multi-point reference. The existing solutions only use a single plane reference, which limits the system when measuring meals with multiple items. This dissertation develops a novel 3D-based dietary measurement technique using the structured light system (SLS) theory. The design of the SLS-based system allows the projection of a multilayer structured light plane onto an object to get a multipoint reference of the depth. Once the depth measurement is obtained, the algorithm needs to perform the following steps to calculate the volumetric information: object segmentation, food recognition, and 360-degree modeling of the scanned object [19].

1.4.2 Calculating a Volumetric Measurement

Over the past decade, image processing techniques in 3D reconstruction have improved drastically. Current 3D reconstruction techniques mainly focus on the resolution of the 3D model; however, calculating the volume from the 3D model has its challenges. One of the main challenges is to close the 3D model spatially. In most cases, when an object is 3D scanned, there are sections that the sensor and camera are unable to capture; these sections are called 3D holes. Current methodologies use estimation algorithms or user input to fill the open areas; however, this requires high computational power and, in some cases, customized hardware. Using an SLS-based algorithm reduces the occurrence of 3D holes; however, if any holes are detected, the system uses 3D scans captured from different angles of the meal to address and close these 3D holes. This algorithm is called 3D mesh hole-filling [20].

1.4.3 Software Compatibility to Time of Flight (ToF) Sensors

Time of Flight (ToF) sensors have the distinct advantage of being able to produce depth information without much additional processing. However, the biggest challenge with ToF sensors is software compatibility. ToF sensors are required to be calibrated to customized hardware, which limits cross-platform compatibility of the system. The trend of newer mobile phones coming with an inbuilt ToF sensor is very promising for the field of dietary measurement. However, the algorithm is required to be compatible with different smartphones. Creating an algorithm, which can adapt to different ToF sensors and operate without customized hardware, can drastically move the field of dietary measurement forward.

1.4.4 Location-Based Data Processing

Location tracking is crucial for capturing meteorological data, local time, and other environmental variables. Meteorological data is commonly used in dietary measurement research

to understand the environmental impacts on dietary habits [21]. In addition to the environmental impacts, location tracking data can be used to automate dietary assessments. One of the biggest challenges in dietary assessment is identifying the food type or the list of ingredients. Most hospitals and medical clinics measure and record the nutritional information of any meal given to the patients; obtaining the location of the patient allows the system to access the facility's food database. This dissertation discusses the use of location-based automation to integrate the facility's food database.

1.5 Scope of the Dissertation

Figure 1.1 demonstrates the scope of this dissertation in a visual format. This dissertation demonstrates the theoretical, functional, and experimental design of a generalizable methodology for measurement and analysis of nutritional intake. An accurate dietary intake measurement design is a balancing act between the performance requirements, user compatibility, and common engineering challenges related to visual-based measurement technologies This dissertation strives to develop a better understanding of the design balances for the measurement of dietary intake, provide algorithms for volumetric estimation, and demonstrate the feasibility of a portable smartphone-based food scanner for a dietary intake assessment. Additionally, the dissertation aims to develop a better understanding of real-world challenges in the integration of dietary measurements into environments such as hospitals and medical clinics.

Theoretical design: A generalizable methodology for the measurement and analysis of nutritional intake is designed based on the structured light system theory. By using a customized enclosure, a laser module can be integrated onto a smartphone to create a small-scale 3D scanner. In addition to the 3D scanner, there is extensive design and development in the image processing

algorithm for calculating volume. This algorithm includes segmentation, automatic calibration, 3D reconstruction, volumetric measurement, and nutritional conversion.

Functional design: This dissertation develops a smartphone-based 3D scanner using the theoretical design of 11n SLS. The developed scanner consists of individual components, such as a smartphone for capturing sensor data and footage of the meal, a laser module with a customized diffraction lens for projecting a matrix plane onto the food item, and a printed circuit board (PCB) for communicating between the laser module and the smartphone. To estimate the nutritional intake, an image processing algorithm was developed to calculate the total volume of the scanned food.

The design of the image processing algorithm includes: the algorithm to calibrate a laser module for depth calculation, the image segmentation algorithm for cropping out the targeted food item from the background, and the 3D reconstruction algorithm to calculate the volumetric information.

Experimental design: The experimental design included both laboratory- and field-based studies. The system was tested in a laboratory environment on regular and irregular shaped objects. After improvements, the system went through multiple user-based and field-based tests to evaluate its performance and percentage of improvements compared to similar systems.

Future work and commercialization: There is a huge demand for an easy to use, accurate and reliable dietary measurement device. The road to commercialization for such a system is not far away and finding the right industry is the key to success.

In addition to the diet industry, this system has been tested in the wound care industry, more specifically in post-operative stoma management. Patients who suffer from an ostomy can

drastically improve their quality of life by using an automated tool to measure and help them cut their wound care wafers to the exact size.

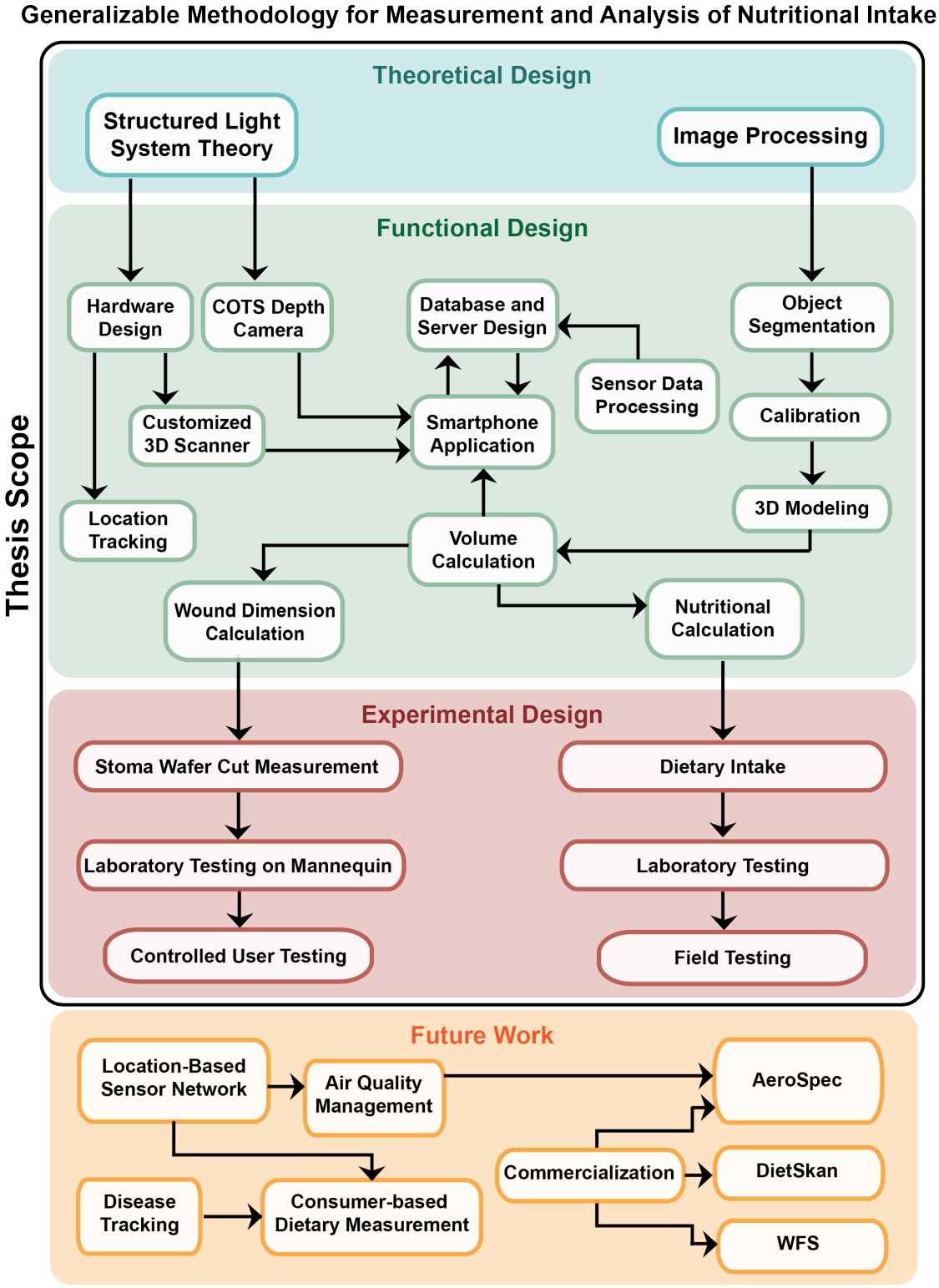

Figure 1.1. The visual presentation of the scope.

1.6 Integration of the Dietary Measurement in Other Applications

The dietary measurement system presented in this dissertation contains three main key features: 1) volumetric measurement, 2) location-based automation, and 3) cloud-based data processing. Each feature is designed to adapt to different applications of epidemiological studies. In this dissertation, the use of the system in wound care management, environmental disease tracking, and real-time air quality monitoring is discussed. Figure 1.2 demonstrates the design of these applications using the dietary measurement key features.

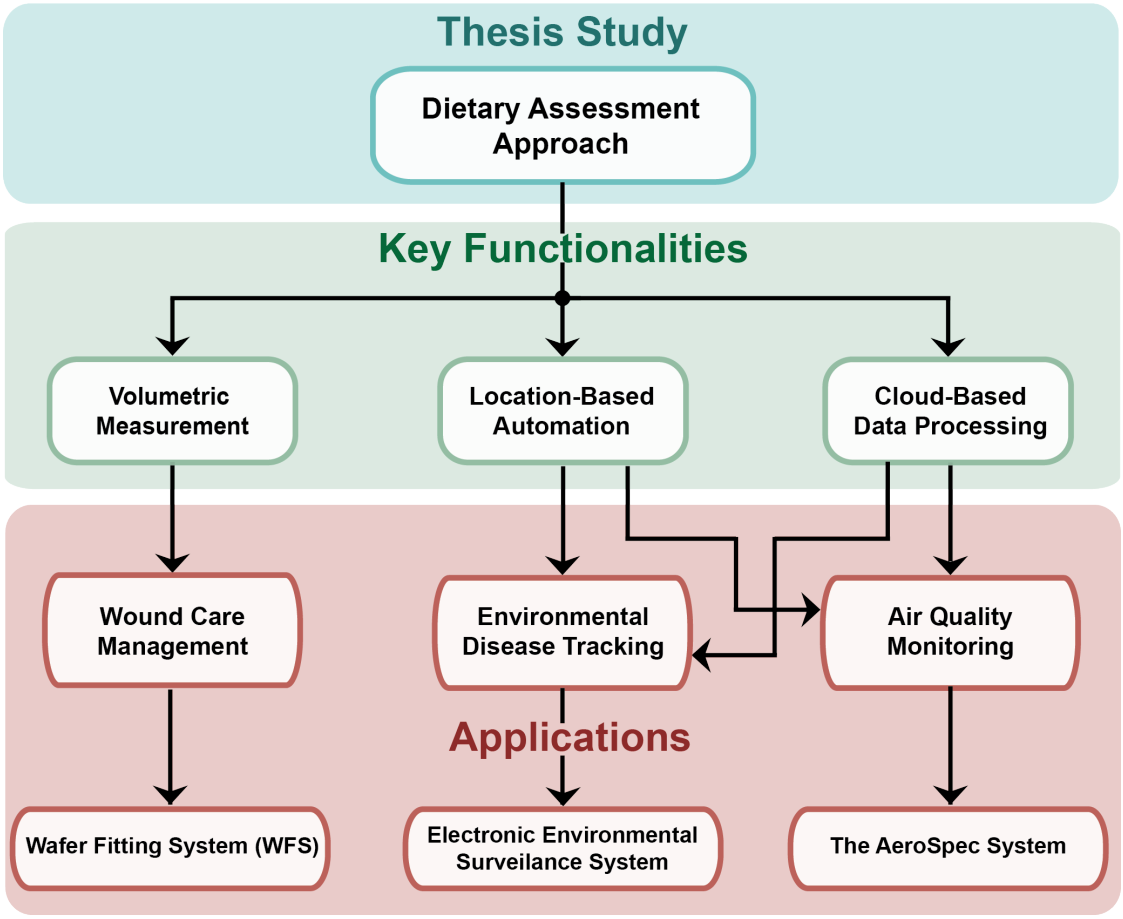

Figure 1.2. The visual presentation of the alternative applications discussed in this contribution using the dietary assessment approach key functionalities.

1.7 CONTRIBUTIONS OF THE DISSERTATION

The dissertation makes five major contributions. First, it develops methodologies and design know-how of 3D measurement and analysis using depth sensors, which can be used in dietary-related research and medical fields. The majority of existing academic literature focused on 3D reconstruction or referenced based measurement for improving the processing time rather than focusing on the underlying principles of dietary assessment to derive a higher performance system with minimal user involvement. Such know-how is critical in the design and optimization of any visual-based measuring instrument for commercial and industrial applications.

Second, it develops a validated image processing algorithm that can aid in the design and optimization of visual-based measurement systems. The cross-platform compatibility enables high scalability in the field of dietary assessment. Although the basic operation of 3D measurement can be described in a brief paragraph, the design complexity for real-world applications is significant. This dissertation has helped to move this area forward by creating an adaptable image processing algorithm.

Third, it presents the published demonstration of a functional smartphone-based dietary measurement device known to the author. The dissertation discusses the methodology and process to design and fabricate small scale smartphone add-on, as well as the challenges and opportunities of such a system.

Forth, it presents the published dietary scanner system known to the author, demonstrating the compatibility and potential for volumetric measurement algorithms and different smartphones. The dissertation discusses many of the design considerations and hurdles for integrating this algorithm as a smartphone application.

Fifth, it presents the published post-operative stoma care system known to the author, demonstrating the compatibility and potential for automation of stoma wafer cutting. The dissertation discusses many of the design considerations and hurdles for integrating a patient-friendly stoma care system.

1.8 SUMMARY OF CHAPTERS

This dissertation is a study of the design, development, and evaluation of a generalizable methodology for measurement and analysis of nutritional intake. Chapter 1 covers the background of instrumentational measurement techniques, specifically 3D measurement techniques in dietary assessment. Chapter 3 discusses the theoretical design of a dietary assessment technique using the SLS. Chapter 4 presents the functional design and what it takes to build such a system. Chapter 5 discusses the experimental process and design to evaluate and test the system in both lab-based and field-test environments. Chapter 6, Chapter 7, and Chapter 8 cover the alternative applications of the dietary measurement approach in wound care management, real-time air quality monitoring, and environmental disease tracking, respectively. The limitations and future work are presented in Chapter 9, and Chapter 10 discusses the conclusions of this contribution.

Chapter 2. USE OF 3D MEASUREMENTS BACKGROUND AND MOTIVATION

2.1 Introduction to Dietary Assessment Methods

Dietary assessments are tools and methodologies which researchers and patients use to calculate nutritional intake. Dietary assessments are commonly used in the medical industry when monitoring diabetic patients' nutritional intake, and in the research industry when investigating the relationship between diet and cancer [22, 23]. Considerable work has been accomplished in the field of dietary intake measurement and calculation. There are currently several approaches to track dietary consumption. Some of the methods are well established in the field of nutritional research, such as 24-Hour Recall (24HR) [14].

The recent improvements to mobile devices and their growing infrastructure has allowed researchers to use smartphones as their main recording tool, especially due to the smartphone's accessibility and convenience of recording information. In the field of instrumentation and measurement, a smartphone-based system is classified as a VBM tool. Calculating dietary intake using VBM techniques requires two sources of information: 1) the volume of the food, and 2) the ingredients of the food. The use of VBM in dietary assessment automates the food volume calculation, which gets converted into nutritional data using the ingredients reported by the user.

2.2 Review of Paper-based Dietary Intake Measurements

There are currently several paper-based methods to track dietary consumption. The most commonly used of these methods, the 24HR food journal technique, uses scales to measure weight and paper-based questionnaires to record the ingredients. However, 24HR has shown significant shortcomings due to inaccurate estimations and complex processes, which has caused

inconsistencies and user burden. One of the major criticisms of paper-based food recording methods is the change of dietary habits; users tend to change their regular diet to reduce the recording burden and avoid mistakes. The change of dietary habits is a common drawback to nutritional food diaries, which require users to manually measure (after a training process) their dietary intake and then write down all of this information into a food diary [24, 25]. The average caloric intake using the 24HR method has a 400 calories per day error, which, in most cases, drops the data accuracy to below 85%, the acceptable threshold.

To overcome these issues, developers have come up with a means of tracking diet with different sensors, cameras, and image processing techniques. Many of these methods can address the drawbacks of 24HR and are often more accurate.

2.3 Review of Digital Dietary Intake Measurement

In the past years, with the improvements in image processing and smartphone sensors, VBM-based dietary intake measurement methods have become more popular. One of the most recent techniques, developed by a team at the University of Ottawa, uses high-quality images taken by a handheld camera (smartphone or any other digital camera) to calculate a user's dietary intake. The proposed method uses the user's thumb to calibrate the system and to estimate the overall portion size [26]. This method has shown great promise in using VBM in dietary assessment. However, there are many limitations with this approach, as using a human thumb as a reference point requires repeat calibrations and does not work for plates with multiple food items.

The Ottawa system uses a graph-cut segmentation method to isolate the food from the rest of the image, allowing for more precise volume estimations. To do this, they establish an undirected graph to create a coordinate system, which, in turn, will enable them to isolate the food in the

image better. By using a 0 and 1 matrix approach, this method segments the food item and removes the background. This process is demonstrated briefly in Figure 2.1 [27].

Although the graph-cut segmentation method is an improvement over the previous color-texture segmentation approaches, it is limited in its accuracy of scanning mixed food plates [28]. One problem here is that the Ottawa method classifies food items after they have been segmented. For complex mixed foods, this process is more complicated because the algorithm has to correctly predict which food item it is analyzing to ensure an accurate measurement. Thus, when food is mixed together on the plate, the system has difficulties determining features particular to food and is unable to determine the food item.

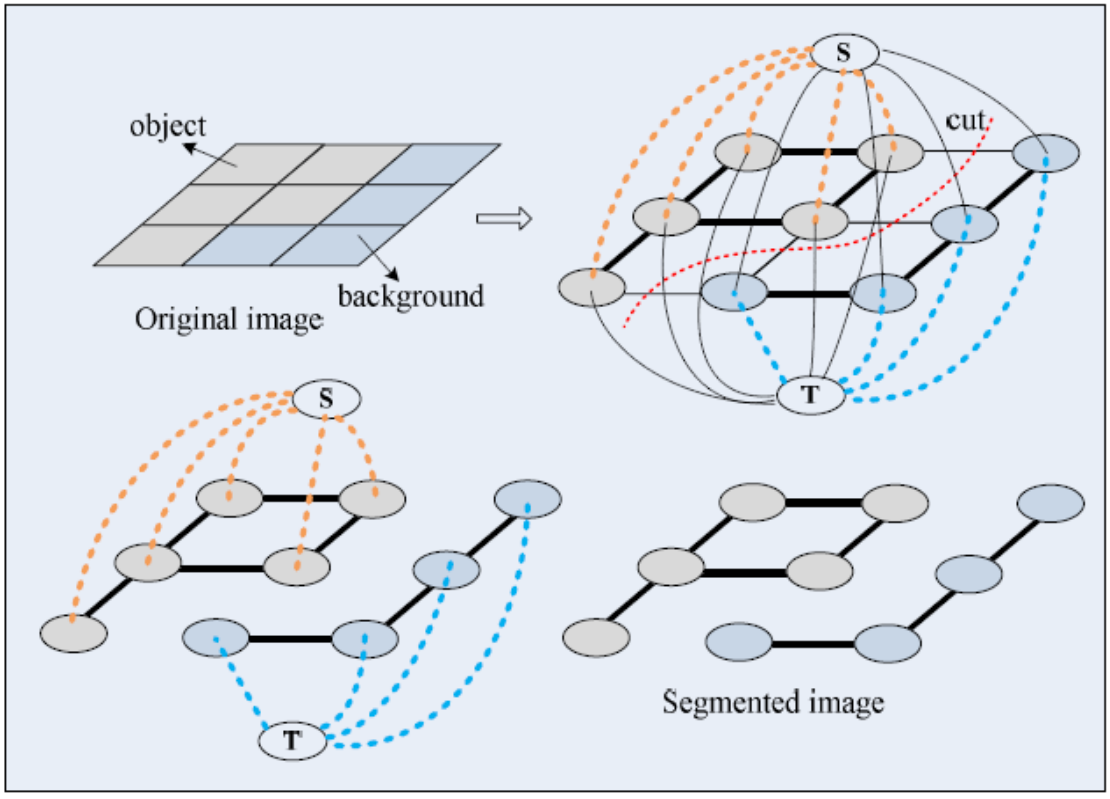

Figure 2.1. Demonstration of the graph-cut process for segmentation of an image.

2.3.1 Review of 3D Reconstruction from Food Image

Most digital dietary measurement methods use a 3D reconstruction approach to find the volume of the scanned item. However, the reconstruction of a 3D model in space requires the actual dimensions of the object, which is calculated using the distance from the camera to the object from multipoint perspectives. The Ottawa approach uses the user's thumb in the picture as a reference point to calculate the distance from food to the camera. Although this provides a reference for calculating the exact dimensions, it lacks the rotational and multipoint reference. Other methods include an index card, which provides distance, rotational data, and a multipoint reference. However, the index card method does not give enough reference points and can only at a single place in space; this causes a decrease in the accuracy of the calculated volume.

3D reconstruction is usually done in two standard methods, single-view and multi-view. A technique developed by a team at the University of Pittsburgh and Cheng Kung University uses a single-view method. It estimates the volume based on previously captured model-based objects [11, 12]. The advantages of this method are the decrease in scanning time and not needing a reference object. The developed method contains three main sections: base plane localization, food segmentation, and volume estimation. The base plane localization is the stage in which the actual measurements are modeled based on the dimensions of the plate itself. This method requires the user to measure the diameter and the depth of the plate before or after the scan. Overall, this method has shown a very low error rate; however, with irregularly shaped meals, the single-view approach might be limiting.

One of the most recent techniques, developed by a team at Michigan Technical University, uses a smartphone camera to calculate the calorie intake [29, 30]. The DietCam method contains an image manager, a food classifier, and a volume estimator, which uses the 3D reconstruction of

the food to calculate the volume. This method is very similar to the Digital Dietary Recorder System (DDRS) method, which is presented in this dissertation. However, the DietCam method uses an external reference point and requires the user to calibrate the smartphone camera before the scan. The external reference object is a credit card, which allows the algorithm to calculate the actual dimensions of the meal. The use of a credit card limits the algorithm to capture an accurate calculation of the volume, which could be satisfactory for consumer use; however, for medical use such as diabetes dietary monitoring, it is not instrumental due to low accuracy of calorie intake. Figure 2.2 shows the process of camera calibration, as well as the scanning process.

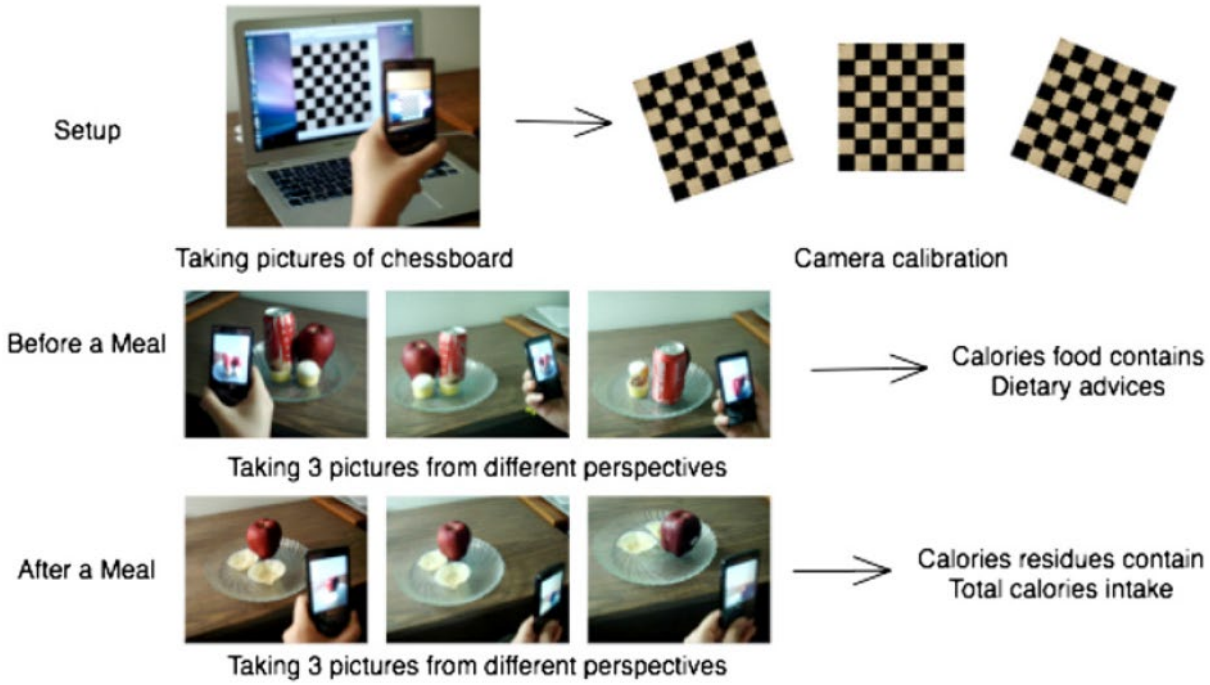

Figure 2.2. DietCam calibration process and scanning using the multi-view feature [29].

A reference-based 3D dietary assessment method was introduced in 2009 and published in the Journal of the American Dietetic Association using the architecture shown in Figure 2.3 [31]. A smartphone application is used to take a before and after picture of the food, while placing a

fiducial marker next to the plate [31]. Image analysis is used to generate metadata and automatically identify characteristics features in the food such as color, texture, and intensity. These characteristics are then compiled together, compared against a database, and the processed data is sent to the user. The test examples used to evaluate this system were done in a lab setting with little to no food interacting with one another.

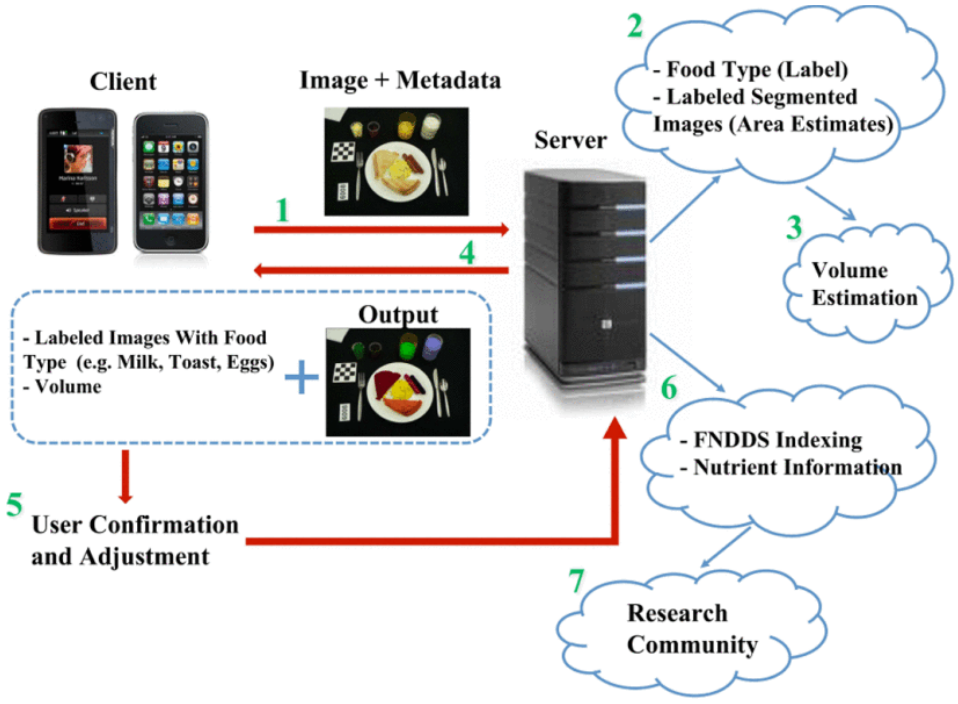

Figure 2.3. 3D dietary Assessment System Architecture (ADA) using a fiducial marker proposed by Purdue University in 2009.

Introduction of a fiducial marker allowed further improvement of the dietary measurement techniques using 3D reconstruction. In 2010 and 2011, researchers at Purdue University published a dietary measurement methodology using a colored index card as a fiducial marker, which is then used as a reference for the image analysis step [32-35]. The system architecture required the user's smartphone to be connected to a server, where all the 3D mesh construction, comparison, and volume estimation is calculated [2]. Then, the estimated volume, food, and nutritional data would be returned to the user. The exact system architecture is outlined in Figure 2.3 (Assessment System

Architecture (ADA)). The fiducial marker is a 2-dimensional (2D) reference point which disables the algorithm from capturing depth and texture for accurate volume measurements. In addition to the index card, this method uses a single image of the meal to calculate the volume estimation of the food while factoring in the geometric properties using shape templates to reconstruct the 3D map of the food. Figure 2.4 shows a sample scanning frame of a beverage. The overall error rate reported for the known templates is reported at 11% for beverages and liquids. Despite the accuracy of the proposed method, it is limited to the database of shape templates.

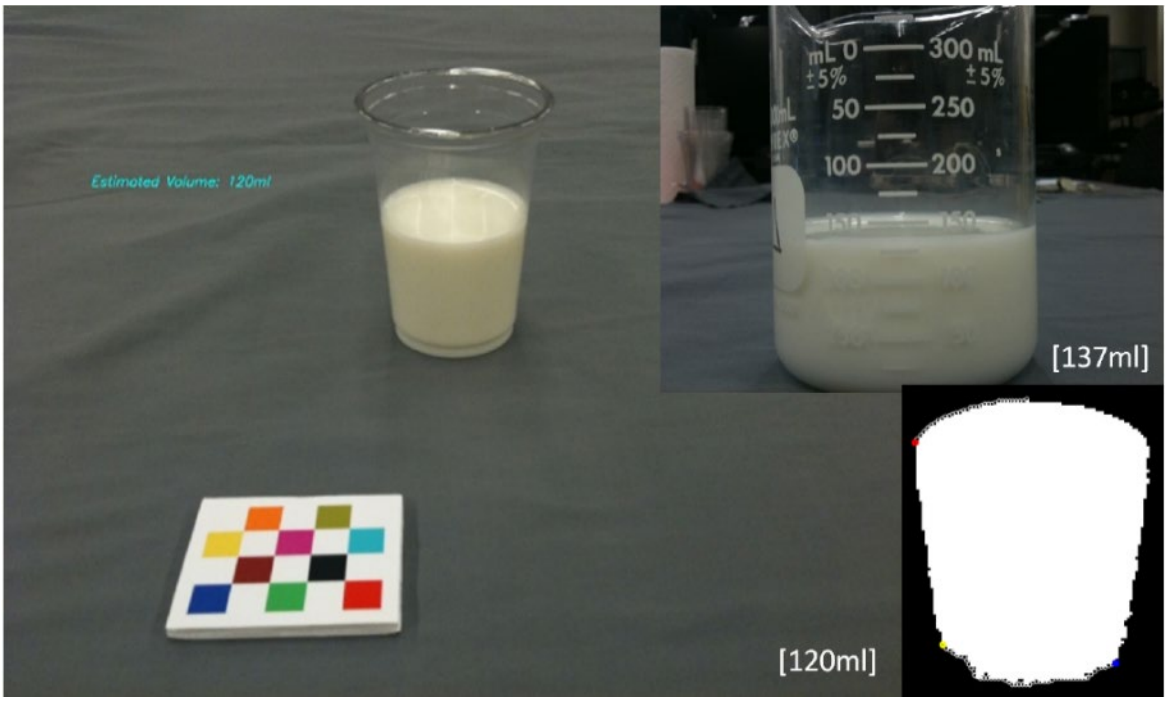

Figure 2.4. A sample image, which was taken with the 3D reconstructed image and the estimated volume vs. the actual volume [33].

2.3.2 Review of 3D Reconstruction Using the Structured Light System

3D reconstruction using SLS presents a compromise between the previously mentioned methods by projecting a multi-layer reference place using structured light [8, 36, 37]. The projection of structured light or depth sensor solves the problem of calibrating the image as well

as the differences in textures in different food items. For low distance sensing, this results in more accurate 3D models with low computational time.

Depth sensors have the distinct advantage of being able to produce depth information without much additional processing. There are a variety of sensor technologies for this task, with ToF sensors being the most common. A popular ToF sensor popular in research is the Kinect sensor V2, which has been used in a variety of research fields [38]. However, a common issue with ToF sensors is the warm-up time and temperature compensation of the sensor, as shown in [39, 40].

2.4 CHAPTER SUMMARY

The field of nutritional assessment is directly linked to the performance of dietary measurement techniques. For many groups of research applications, such as dietary-related cancer, the minimum accuracy level is required to be higher, and the system must be more adaptable.

With current technology advancements in 3D reconstruction, VBM techniques have become more popular in the research field. The use of VBM techniques requires high computational power and repeated calibration due to a change in background and lighting. There is currently no comprehensive dietary intake solution that eliminates the need for a paper-based questionnaire. Hence, despite the advancements in digital dietary measurement, a 24HR food questionnaire has been the dominant method of dietary measurement in the nutritional assessment field and will be for the foreseeable future due to its relative comprehensiveness and adaptability.

With no obvious methodology for dietary intake measurement for future research, the market is open and in search of new dietary measurement solutions using VBMs.

Chapter 3. THEORETICAL DESIGN OF VBM SYSTEMS IN DIETARY MEASUREMENT

This chapter discusses the initial framework used in developing a VBM system for dietary intake measurement. The presented framework addresses the main challenges in the field of dietary assessment by utilizing smartphone technology and structured light system theory.

3.1 STRUCTURED LIGHT-BASED VBM SYSTEM

In recent years, VBM systems have been introduced to the field of dietary measurement [41]. The design of the VBM framework consists of a measurement instrument, a communication module, an image processing algorithm, and a web server (cloud computing.)

Figure 3.1 demonstrates the general system design of a dietary measurement system as a framework. This framework has been used to develop both the DDRS and DietSkan systems.

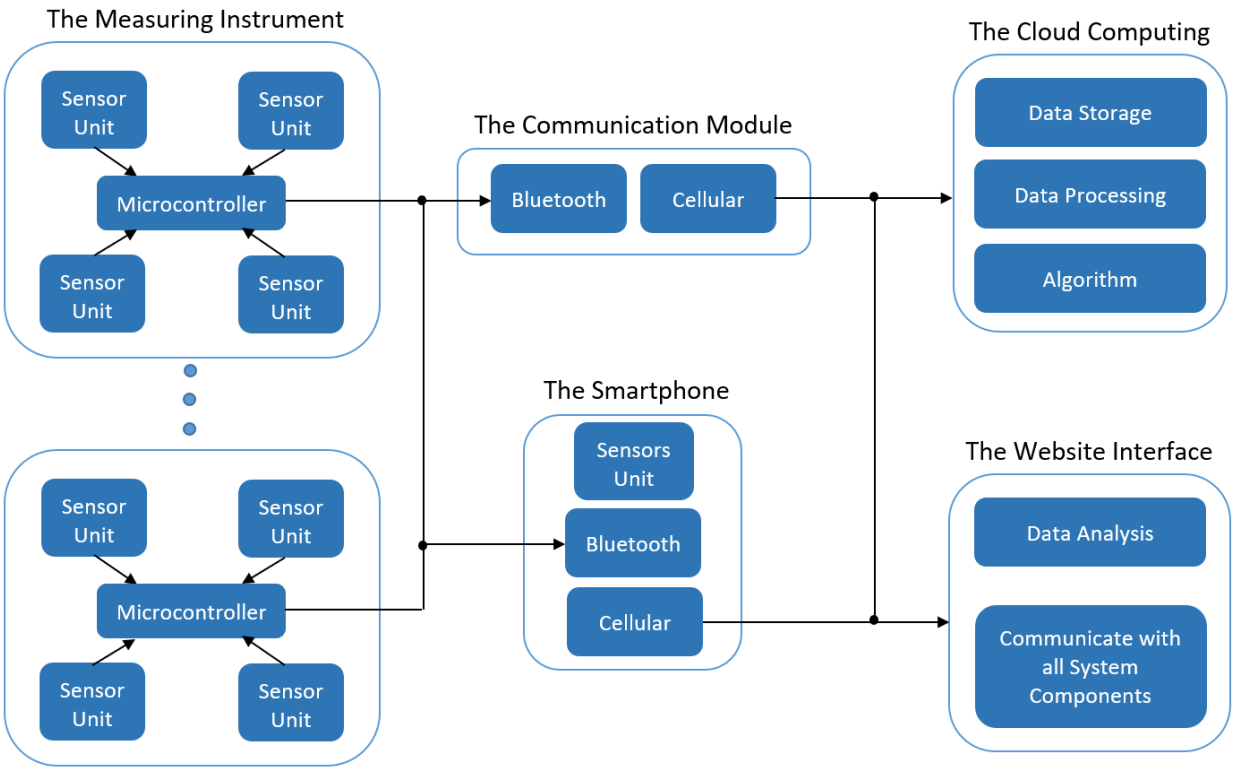

Figure 3.1. The dietary measurement framework design, including all the components.

The SLS-based sensors are the preferred type of ToF sensing category due to higher accuracy, in-depth acquisition, simple optical arrangement, easy feature extraction of light patterns, low cost, and robustness to ambient light sources on the spot [42-46].

Using SLS, a mathematical model can be created to estimate the depth or the distance from the camera to the specific object. A VBM SLS system for dietary measurement includes a visual sensor (camera), motion sensors (accelerometer and gyroscope), and a laser projector. Figure 3.2 demonstrates the triangulation of a 3D point, P. Once the system is calibrated, the relative distance between the projected point and the camera is determined using (1).

$$|PO| = \frac{|PO| \times \sin(PLO°)}{\sin(LPO°)} \quad (1)$$

where $|PO|$ is the depth or absolute distance from the camera to the projected laser beam on the surface, (PLO°) is the angle of the laser projector with respect to the camera and the laser beam, and (LPO°) is the angle of the laser beam with respect to the camera and the laser projector.

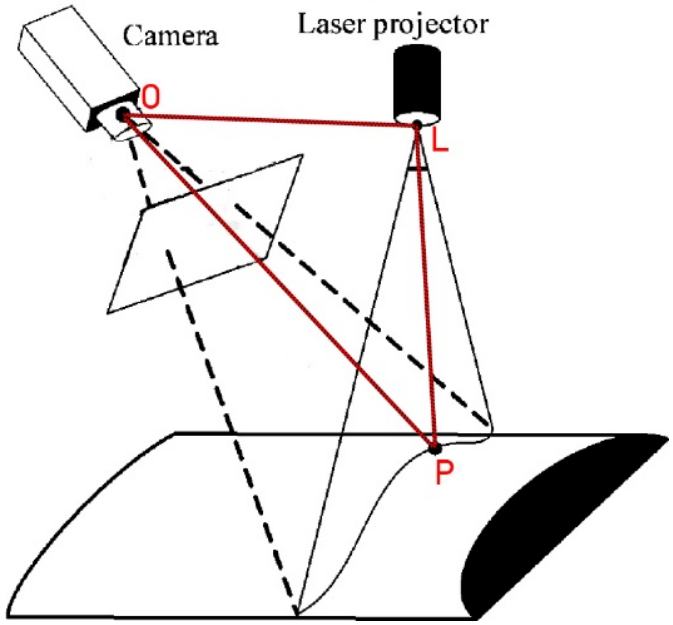

Figure 3.2. Triangulation method utilized in a structured light system for capturing depth and texture [47].

The Digital Dietary Recorder System (DDRS): Figure 3.3 demonstrates the process of 3D reconstruction using DDRS. The device is rotated around the food slowly, the laser module is switched on and off rapidly, the phone collects videos, and the volume is reconstructed. Video is used for volume estimation instead of a single image from one direction because prior shape information for the object is not assumed.

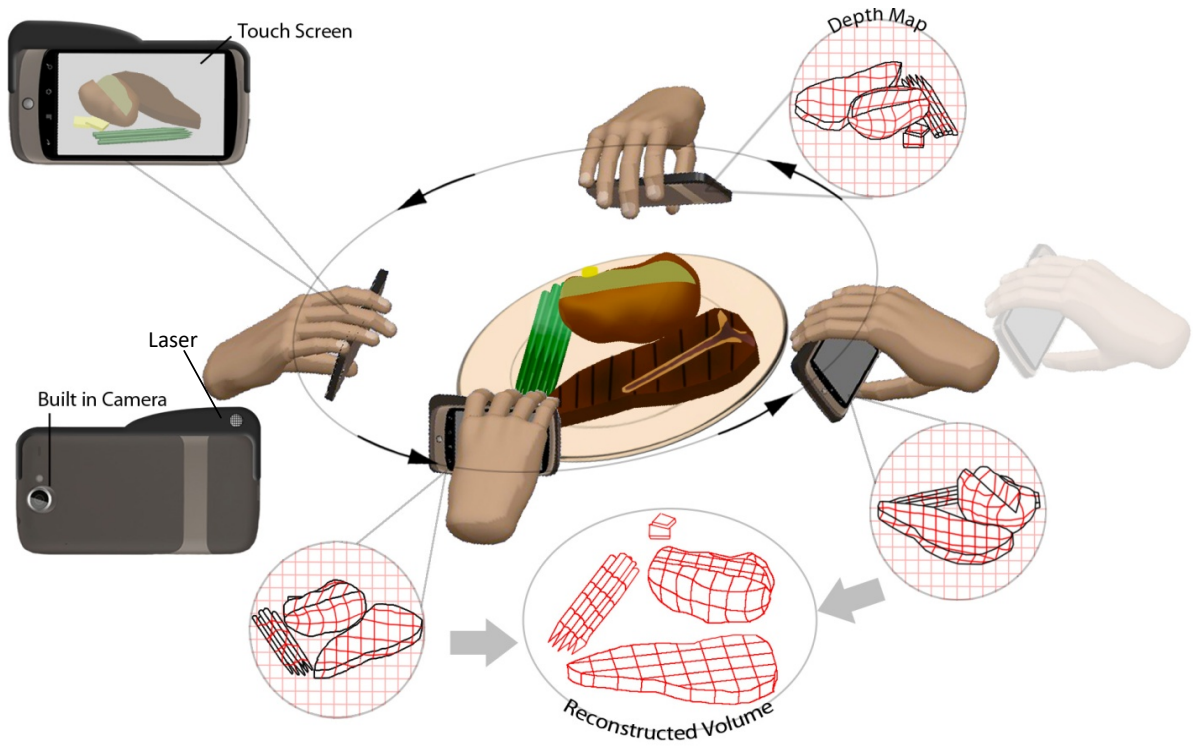

Figure 3.3. Concept of volume reconstruction in DDRS.

The DietSkan System: The recent development of SLS-based ToF systems as a real-time vision sensor has the potential of improving 3D measurement applications, including dietary assessment techniques. The ToF vision sensor can calculate depth by measuring the phase delay (time of flight) and the infrared light (IR) reflection from the object. Popular systems using this approach include the Kinect and the Structure Sensor by Microsoft and Occipital, respectively. These systems use the triangulation method to determine depth and detect texture [48-55]. Figure 3.4 shows a popular and small-sized ToF sensor called the Structure Sensor.

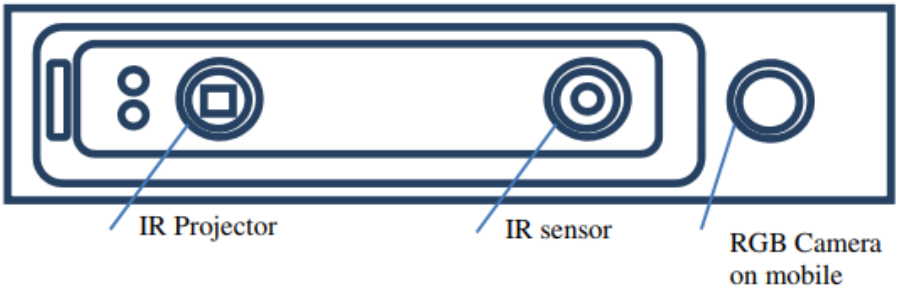

Figure 3.4. The Structure Sensor created by Occipital used in the DietSkan System.

3.2 Image Processing Algorithm Theory and Design

The image processing algorithm presented in this dissertation consists of four primary steps: 1) object isolation and segmentation, 2) SLS depth acquisition, 3) 3D reconstruction modeling, and 4) volumetric calculation.

Object Isolation and Segmentation Algorithm: The first step toward dietary measurement is to isolate the food object from the image of the video frame. It is crucial to remove the background in this step to eliminate any inaccuracies in the 3D reconstruction modeling process. There are many variables, which could alter the results, such as light intensity, background color, food color, and food complexity. Hence, user input is required to ensure accurate detection of the edges of the selected food object.

SLS Depth Acquisition: The next step is to acquire the depth or the distance from the camera to the object. This is crucial for the system to calculate the actual dimensions and scaling of the image. Specifically, if the SLS hardware is customized, it requires an in-depth calibration to create a list of reference space coordinates. One of the main challenges is repeated calibrations, which are addressed in the DietSkan system using an initial one-time calibration.

3D Reconstruction Modeling: Once the depth data for each space coordinate is calculated, the overall 3D reconstruction of the image can be modeled numerically using computer vision. This process needs to be done from all the frames (minimum of 6 frames from a 360-degree scan).

The stitching algorithm connects the individual 3D frames by integrating the accelerometer and the gyroscope sensor data. The integration of the sensors and the individual frame 3D models allows for the determination of the spatial positioning and outputs a 360-degree 3D model of a given object. The fully reconstructed model is still incomplete and includes missing sections or holes.

Volumetric Calculation: The obtained model has imperfections due to blind spots during image capture, as well as the boundary between individual food items and the plate; hence, the volume cannot be calculated accurately. The data is post-processed to obtain the elements of interest, eliminate the remaining regions of the scan, and fix any imperfections that are present. Finally, the volume is calculated on the processed 3D model. The hole-filling algorithm is used to fill all the missing sections by applying the Advanced Front Mesh (AFM) technique [56].

3.3 CHAPTER SUMMARY

The lack of accurate and adaptable 3D-based VBM systems in dietary assessment is due to the complexity of volumetric analysis. To successfully measure volumetric data, the VBM system must include a hardware component, which consists of a variety of sensors, and an image processing algorithm, which consists of image segmentation, depth calculation, 3D modeling, and volumetric calculation. The volumetric calculation must be done once the 3D model of the object is spatially closed. Hole-filling is one of the main shortcomings of the existing 3D measurement tools.

Chapter 4. FUNCTIONAL DESIGN OF VBM SYSTEMS IN DIETARY MEASUREMENT

The functional design of a dietary measurement system presented in this chapter discusses the development of a smartphone add-on called Digital Dietary Recorder System (DDRS) to be used in the nutritional assessment field. In addition to the hardware development, this chapter discusses the development of the image processing algorithmic information of a given meal.

The current technological advancements in ToF sensing lead to the development of a new software-based system called DietSkan. The DietSkan system takes advantage of SLS-based ToF sensors to calculate the nutritional value of a meal using 3D reconstructed modeling.

4.1 DIGITAL DIETARY RECORDER SYSTEM (DDRS) DESIGN

By following the general VBM framework shown in Figure 3.1, the design of the DDRS is developed using a structured laser patterning, a Bluetooth module, a smartphone, and the main DDRS algorithm. The central system is composed of a smartphone, a hardware add-on, a smartphone application, and a web server. Figure 4.1 shows the overall design of the DDRS system.

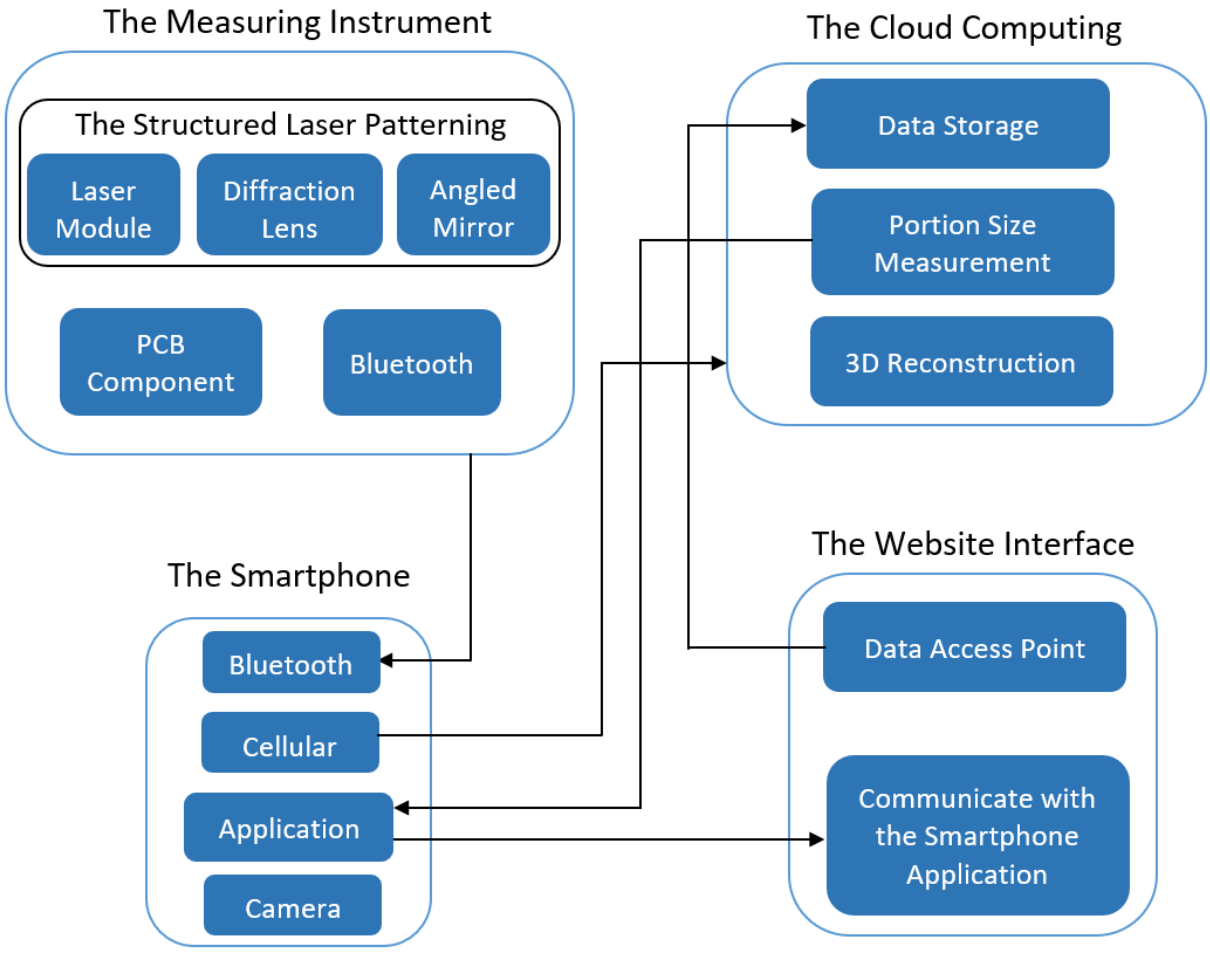

Figure 4.1. The DDRS flowchart design, which consists of depth-sensing hardware, a smartphone, and the cloud server.

4.1.1 The Hardware Design of the DDRS

The DDRS hardware consists of a laser module, a diffraction lens, and a circuit design component to connect the laser module to the smartphone. The hardware is mounted on a 3D-printed housing made of ABS plastic.

4.1.1.1 The Design of the DDRS Enclosure.

The housing is designed using a 3D computer-aided design (CAD) software, SolidWorks [57]. In most structured lighting systems, the camera is kept far from the projector. However, the mobile client cannot tolerate a very large camera-to-laser distance due to the portability requirement.

The camera-to-distance angle needs to be carefully designed, although it does not affect the error much in a pinhole model. During the structured light scanning, the depth from the camera to the food is usually not large, as the participant is generally right in front of their meal. A valid distance range is typically tens of centimeters. If the optical center lines of the camera and laser are parallel, a 70 mm distance will make the laser pattern away from the center of the collected videos. A common depth between the camera and food is set to 40 cm, resulting in a 10˚ angle toward the camera. The housing is designed to hold the laser module parallel with the phone to reduce the housing size, shown in Figure 4.2

Figure 4.2. (Left) The distance and angle between the camera and laser, and (Right) the DDRS enclosure. The red circle highlights the 2-dimensional angled mirror.

4.1.1.2 The Laser Module of the DDRS System.

The measuring instrument of the DDRS is an SLS-based projector, which uses a 532 nm wavelength diode to project a laser beam through a customized diffraction lens to produce an 11×11 matrix of laser dots [46, 58]. The DDRS hardware is classified as a VBM due to its visual sensor (smartphone camera) and the SLS-based projector. The DDRS uses a smartphone digital camera to capture the 2D images with projected laser dots [59].

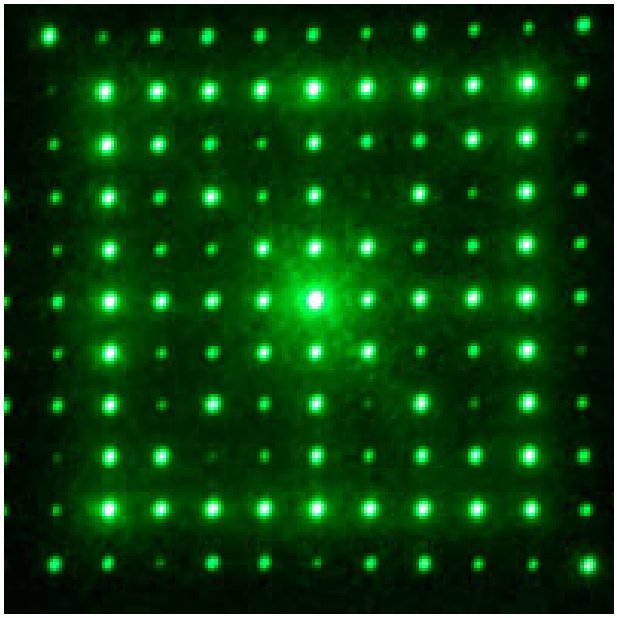

Figure 4.3. The 532 nm wavelength diode to project a laser beam through a customized diffraction lens to produce an 11×11 matrix of laser dots.

The laser module used to create the structured laser system is a 5 mW, 532 nm diode purchased from Laser Components [60]. Choosing a 532 nm laser diode allows for better visibility for both the user and the algorithm. Additionally, using a 5 mW instead of 1 mW module ensures enough power for the laser beam to pass through the diffraction lens and project onto the food items. A more detailed specification on the laser module is presented in Table 4.1.

Table 4.1. FLEXPOINT 532 nm green laser module specifications

Specification	**Measurement**
Wavelength	532 nm
Output power max	10 mW
Output power stability	< 5% after warming up at 25 °C
Beam divergence	< 1 mrad
Beam angle error	< 1°
Lifetime	5000 hrs. (at < 4 mW)
Input voltage	5 - 30 VDC
Operating current	< 300 mA
Operating temperature	15 - 35 °C
Mechanical	length 57 mm, diameter = 11.5 mm
Housing	aluminum

4.1.1.3 The Design of the DDRS Printed Circuit Board (PCB).

To communicate between the laser module and the smartphone, a printed circuit board (PCB) was designed and developed. The PCB consists of a Bluetooth module, a lithium battery to act as a power source for the laser module, a micro USB charger to charge the battery, and other miscellaneous electronic components for the circuitry. Figure 4.4 shows the schematic of the DDRS printed circuit board. The Bluetooth enables the DDRS smartphone app to communicate to the laser module, which allows the DDRS smartphone app to turn the laser off and on to optimize the power consumption.

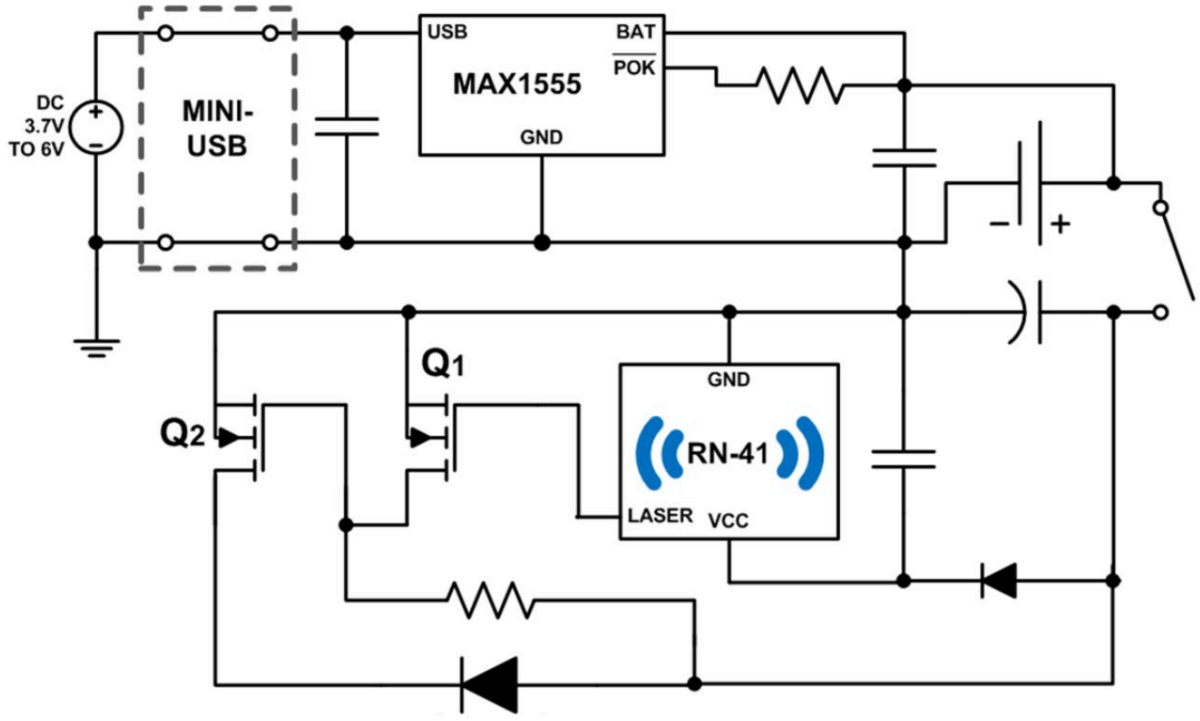

Figure 4.4. Schematic design of the printed circuit board.

The PCB includes overcharging protection to keep the battery from burning, as well as the power option to work while connected to the power. Figure 4.5 shows the PCB design of the board.

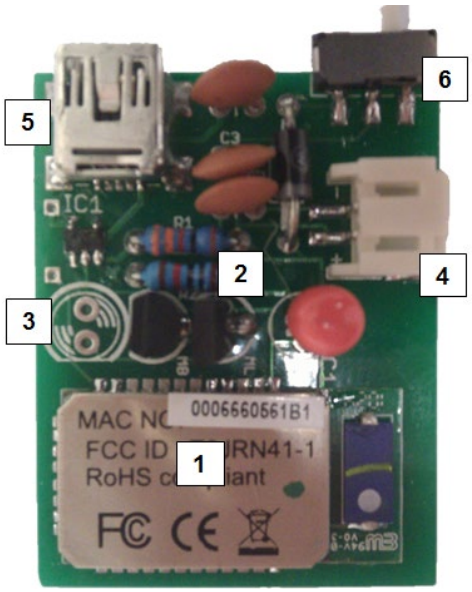

Figure 4.5. The DDRS circuit module, which includes: 1) The Bluetooth module, 2) PNP MOSFET, 3) output signal (to the laser module), 4) Battery plug, 5) USB charger, and 6) On/Off switch.

4.1.1.4 Assembling of the DDRS 3D Scanner

As shown in Figure 4.6 and Figure 4.7, the housing provides an appropriate fitting of all the components in a wearable size. The smartphone is the component that connects the physical portion to the software piece. By having a customized smartphone app, the DDRS can upload the captured video, as well as the sensor data (including accelerometer and gyroscope) onto the cloud for volumetric analysis. The algorithm starts by selecting the best six frames from the captured video and then processes each frame by segmenting and 3D mapping the individual items of the plate. While this process completes, the user inputs the names of each item on the plate, which allows parallel computation and distracts the user from waiting too long.

Figure 4.6. DDRS enclosure with the structured light system demonstrating all the electronics included.

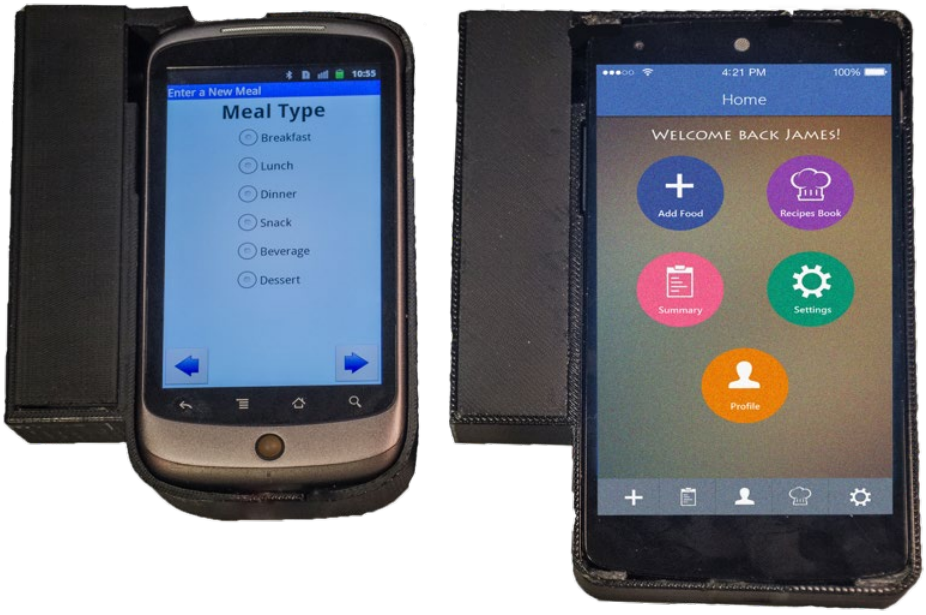

Figure 4.7. (Left) The first DDRS prototype, and (Right) the second DDRS prototype

The recording process of the DDRS system is as follows: 1) the user takes a 360-degree video of their food on the plate, 2) the recorded video uploads to the servers, 3) the image processing algorithm uses the scan to calculate the nutritional information, and 4) the nutritional information

gets transferred to the user's smartphone application. [61]. Figure 4.8 shows the overall process of dietary intake: recording and analysis using the DDRS device, and the DDRS web-based software.

Figure 4.8. DDRS overall system overview.

4.1.2 The Functional Design of the DDRS Image Processing Algorithms

The DDRS software includes four main algorithms: object isolation (image segmentation), SLS depth acquisition (auto dot detection), 3D reconstruction modeling, and volumetric calculation. Figure 4.9 shows the flowchart of the DDRS software and how all the pieces connect to calculate the volume of the food item.

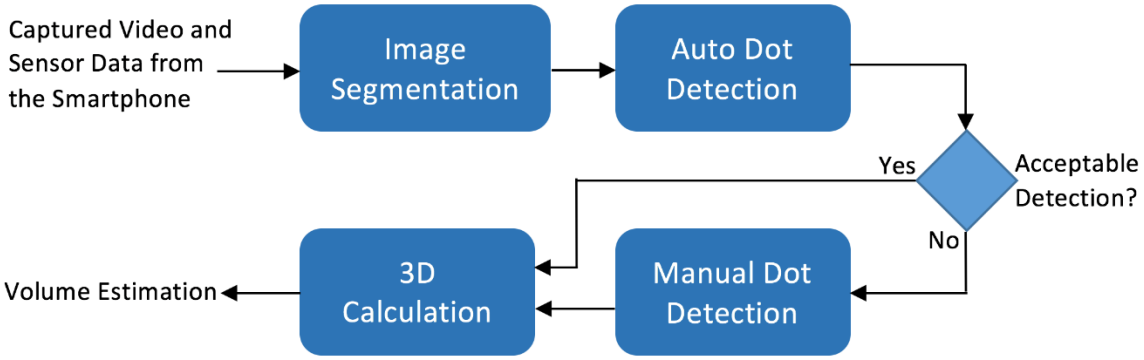

Figure 4.9. The DDRS volume calculation software flowchart.

4.1.2.1 The Design of the Image Segmentation Algorithm.

The current approach utilizes saliency detection via the graph-based manifold ranking algorithm and automatic image cropping to increase the efficiency of the algorithm and to automate image segmentation by locating only the food on a plate [62]. Since researchers at Fred Hutchinson Cancer Research Center were the primary users of this application, this algorithm was tailored to work best with foods placed on the white or brightly colored plates used at the facility. Figure 4.10 shows an overview of the stages of the algorithm.

Figure 4.10. The segmentation algorithm flowchart.

Auto-cropping of the plate: To utilize saliency detection for image segmentation in a fast and accurate manner, the image of the food should ideally only contain the object of interest [63]. The goal of this stage is to isolate the plate and remove the background.

The first step is to take a picture of the entire plate of food, which can contain much more background than just the plate and the food itself. Once this image is taken, plate cropping is made possible by the fact that the plate is brighter than its background, (limited to lighter colored plates.)

The image is first converted into the grayscale domain by applying weighted sums. This is computed using the RGB weighted conversion formula, shown in (2),

$$GS = 0.2989R + 0.5870G + 0.1140B \quad (2)$$

where GS stands for grayscale, R is the value of the red pixel, G is the value of the green pixel, and B is the value of the blue pixel.

The conversion equation is based on the SDTV standard BT.601; a thresholding value is then set to separate pixels that are considered to be bright (the plate) from dim (background) pixels. This creates a binary image that works as a mask. At this stage, several noise-reduction steps are applied to improve the image. First, to ensure that the entire plate is captured, we fill in all of the holes in the binary image. By using the previously created mask, the black pixels enclosed by connecting borders of each object are filled in. This is done to mask the bright objects in the image completely, shown in Figure 4.11.

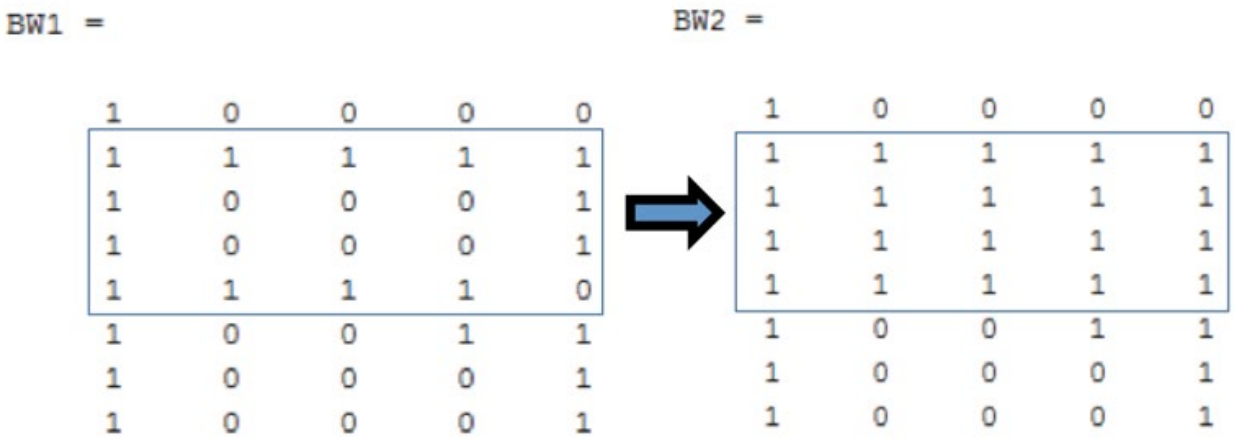

Figure 4.11. The binary holes noise reduction process (binary masking).

These existing masks represent all of the bright individual objects in the picture; the areas are calculated by adding up the connected pixels. The object with the largest area is isolated, and the remainder of the image is flagged as the background and removed. This isolated object is assumed to be the plate, as it is expected to be the main focus of the image.

With this information, the boundaries of the plate can be located and extracted from the image. This is done by finding the minimum and maximum indices in both the horizontal and vertical dimensions, which we use to resize the image and bound the image size to the plate of food. Figure 4.12 shows the steps of this process.

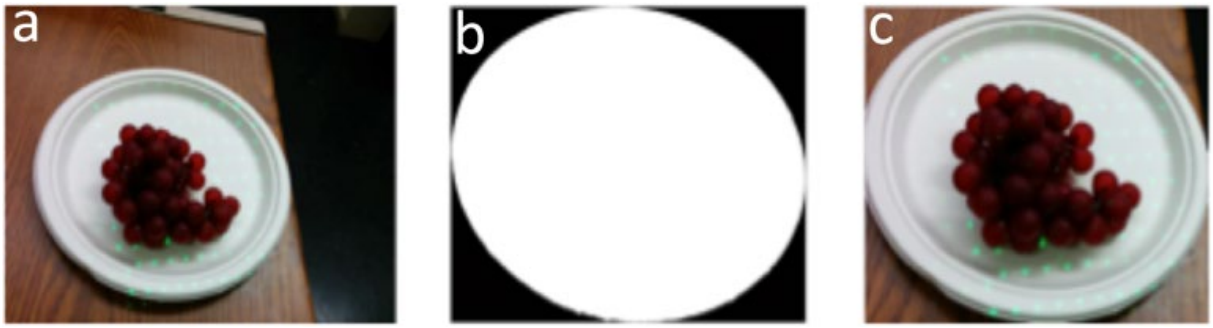

Figure 4.12. The transition of a plate of grapes from the original image (a), to binary mask image (b), to the minimized model bounded by the plate (c). In step (c), the size of the image has been significantly reduced. However, it still has more pixels than just the food itself. Since the salience mapping function requires the image to be tightly bounded by just the food to work, the image still needs to be cropped further.

Secondary image cropping: With the first iteration of the image cropping completed, the image is reduced to be strictly bound to the plate, as shown in Figure 4.12 (c). The secondary cropping is performed using image erosion and analyzing the image in the HSV domain [64]. The first step of the algorithm is to apply a binary erosion to the image in the grayscale domain. The binary erosion of an image A with a structuring element B is defined as the set operation shown in (3):

$$A \ominus B \equiv [Z|BZ \subseteq A.] \tag{3}$$

where A is the binary erosion of the image, B is the structuring element, and Z is the pixel location.

This is the set of pixel locations, Z, where the structuring element overlaps only with the foreground pixels in A. The gray-scale erosion of $A(x, y)$ by $B(x, y)$ is defined in (4):

$$(A \ominus B)(x, y) = \min[\{A(x + x', y + y')] - B(x', y')|(x', y') \in D_E\} \tag{4}$$

where D_E is the domain of the structuring element B and $A(x, y)$, and is assumed to be $+\infty$ outside the domain of the image.

The structuring element does not need to be a specific shape, but it must contain the food and background to reduce the segmentation threshold value. The result of this erosion provides the backdrop of the image. The background is then subtracted from the original image. We apply thresholding again to highlight just the significant borders of the object and to remove as much of the noise as possible from the surrounding objects. The holes in the binary image from the thresholding are then filled in, and the remaining noise is removed from the image. This creates a rough segment that is not meant to bound the image to only the food but to reduce the image's size yet again for further processing.

The next step in the algorithm is to apply a filter to the previously segmented mask, which is done by locating the food on the plate. This filter converts the image to the HSV domain. The process we use to convert from RGB to HSV is shown in (5) – (9)

$$R' = \frac{R}{255}, \qquad G' = \frac{G}{255}, \qquad B' = \frac{B}{255} \tag{5}$$

$$H = \begin{cases} 0°, & \Delta = 0 \\ 60° \times \left(\frac{G' - B'}{\Delta} mod 6\right), & C_{max} = R' \\ 60° \times \left(\frac{B' - R'}{\Delta} + 2\right), & C_{max} = G' \\ 60° \times \left(\frac{R' - G'}{\Delta} + 4\right), & C_{max} = B' \end{cases} \quad (6)$$

$$C_{max} = \max(R', G', B'), \qquad C_{min} = \min(R', G', B') \quad (7)$$

$$V = C_{max}, \qquad \Delta = C_{min} \quad (8)$$

$$S = \begin{cases} 0, & C_{max} = 0 \\ \frac{\Delta}{C_{max}}, & C_{max} \neq 0 \end{cases} \quad (9)$$

where H, S, and V are each the RGB value in HSV (hue, saturation, value) domains. R', G', and B' are the pixel values calculated from the original RGB data. C_{max} and C_{min} are the thresholding values to distinguish the background from the image itself.

At this stage, the image can be decomposed and analyzed in each of the three domains (hue, saturation, value). The image is considered in the saturation domain if the food contrasts significantly with its background. In this case, we use a white background to fulfill this goal. By applying a thresholding value, the food itself can thus be separated from the plate and background that remains after segmentation.

This results in a binary image with the food outlined and significantly less background noise. At this stage, the first automatic-cropping process can be applied to this binary image. This is done to bind the image tightly to the object and reduce the image size before passing it to the Manifold Ranking Saliency Detection function.

Manifold Ranking and Saliency Detection: The image is now fully cropped and ready to be mapped by the saliency algorithm. Since the image size has been minimized, the runtime of the saliency function will be improved significantly by running it on the original image.

We now apply the graph-based manifold ranking and saliency detection function on the fully cropped image. The saliency is found by ranking the similarity of image elements with foreground and background cues. This is represented as a close-loop graph with superpixels as nodes. This algorithm returns a saliency map image, which is used in the final step of the segmentation process.

The saliency map removes most of the additional noise that the original cropping process may have missed. Since the saliency map is a grayscale image rather than a binary image, a thresholding value must be computed again to segment just the food on the plate. The original image, the saliency map, and the final output result are shown in Figure 4.13.

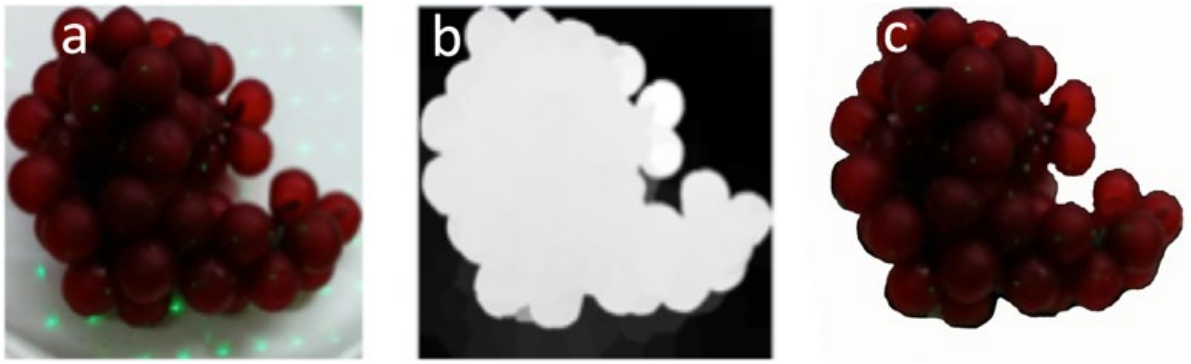

Figure 4.13. The transition of a plate of grapes from the fully cropped image (a), to a saliency map (b), to a completely segmented image (c).

4.1.2.2 The Design of the Automatic Laser Dot Detection Algorithm

The approach of automatic laser dot detection on a segmented image adapts computations of several successive image filtering and masking operations. The primary objective of the algorithm is to find the pixel location of each laser dot on the food in a picture and output a multilayer

reference plane. Given that all the laser dots used for this application are bright green, color properties and mathematical modeling are used to create filtering and detection methods that work best with green laser dots. The three primary filters implemented for the algorithm are the HSV filter, the cosine similarity, and luminance masking. Figure 4.14 shows the high-level block diagram overview of the Automatic Dot Detection.

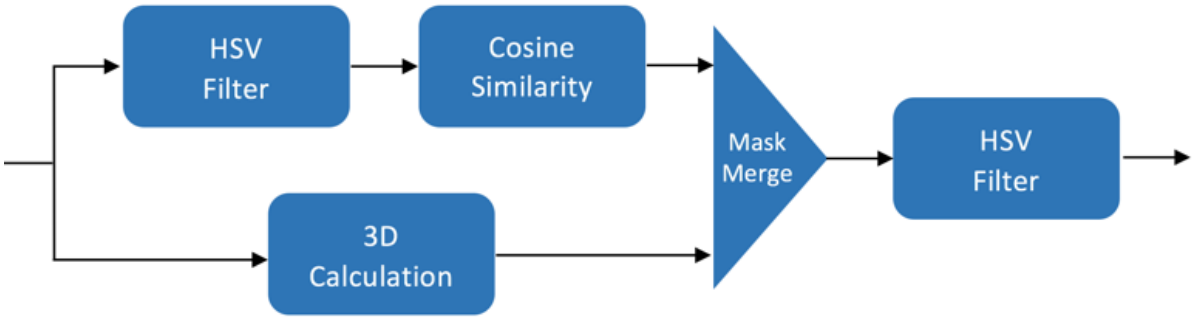

Figure 4.14. The automatic dot detection algorithm flowchart.

HSV Filter: The first filtering technique applied to the segmented image is an HSV filter that intensifies the brightness of green pixels in the image. This is a necessary step since the cosine similarity mask (detailed in the next section) relies on the difference between the green pixels and all other pixels in the image. The image below illustrates the relationship between color information and intensity in the HSV domain.

The computations used for calculating the hue and saturation values utilized for this filter are shown in (10) and (11).

$$GH = 90° \leq PH \leq 180° \tag{10}$$

$$LCI = PS \geq 90\% \tag{11}$$

where GH is green hue, PH is pixel hue, LCI is laser color intensity, and PS is pixel saturation.

Since laser dots tend to be the most saturated color in the image, the green image pixels are defined by the hue values between 90 and 180 degrees and with a color intensity greater than 90%.

Once the HSV filter is applied, the image is converted from the HSV domain back to the RGB domain to be processed by further filtering and masking techniques.

Cosine Similarity Mask: Once the HSV filter has been applied, the image shows the laser dots with more intensity. At this stage, cosine similarity masking is used to isolate the laser dots further in the image.

The approach begins by removing most of the background of the image (non-laser dots). This process is mathematically computed by determining the similarity of every pixel in the image to the determined color of the laser dots (filtering mask image). The equation for this similarity is known as cosine similarity, denoted by (12):

$$S = \cos(\theta) = \frac{A \times B}{[[A] \times [B]]} \tag{12}$$

where S is cosine similarity, A and B are vectors, and θ is the angle of the device held at that moment.

An iterative process is executed to determine the color of the dots dynamically. Figure 4.15 shows two iterations: one with a value of pure green, and the second with the adjusted value.

Figure 4.15. (a) Original image (a croissant), (b) croissant image after the luminance mask, (c) second iteration of cosine similarity using dynamic thresholds.

For the iterative process to function, the result is required to converge to a particular value. Hence, the threshold must be set to a value that eliminates as much noise as possible. The value

that is selected for the threshold must be chosen carefully; if the wrong value is selected, the output does not converge. Therefore, a value with a low threshold should be selected to help filter out the noise in the image. Creating a dynamic threshold would be ideal here, but it does not guarantee to isolate these dots in different image types. Hence, images that contain objects with high contrast to the dots would require additional maskings such as cosine similarity and luminance (which are both detailed further in the next section).

Luminance Mask: Since applying the cosine similarity mask is not enough to isolate the dots in the image, a combination of the cosine similarity mask the luminance mask are used to achieve more accurate results. The two masks are applied to the original image separately and then combined (multiplied) to produce a final mask with highly accurate dot locations. The luminance mask takes into account the intensity of the light in the image to isolate the dots.

This luminance filter begins by first isolating the background of the image, which, in this case, includes everything that is not a laser dot. This is accomplished by performing a morphological opening operation using a structuring element of a disk. In this scenario, a morphological opening means the dilation of the erosion of a set A by a structuring element B. (13) shows this operation.

$$A \circ B = (A \ominus B) \oplus B \tag{13}$$

where A is the image, B is the structuring element of a disk; $\ominus$ represents erosion, and $\oplus$ represents dilation.

This calculation leaves us with the image background and with some noise of the original laser dots. The background is subtracted from the image to isolate the border and the laser dots of the object.

With the foreground now somewhat isolated, the next step is to reduce the overall noise in the image. This is done by converting the image to a luminance matrix, and thresholding the

acceptance value at a certain cutoff to retain the brightest parts of the image. The resulting image contains laser dots and some of the border but does not remove the noise that consists of darker pixels. (14) shows how the luminance is calculated.

$$L = 0.2126R + 0.7152G + 0.0722B \tag{14}$$

where L is luminance, R is red color value, G is green color value, and B is blue color value.

Final Error Catching: Although the algorithm by itself is highly accurate since it is also critical that the 3D calculation algorithm get the correct values, the Manual Dot Selection algorithm was added to help users manually add or remove laser dots in the image that might not have been captured. This feature includes a graphical user interface (GUI) that allows the user to add dots to the image not caught by the algorithm, as well as removing false positives detected in the image. This final error-catching step can be seen in Figure 4.16.

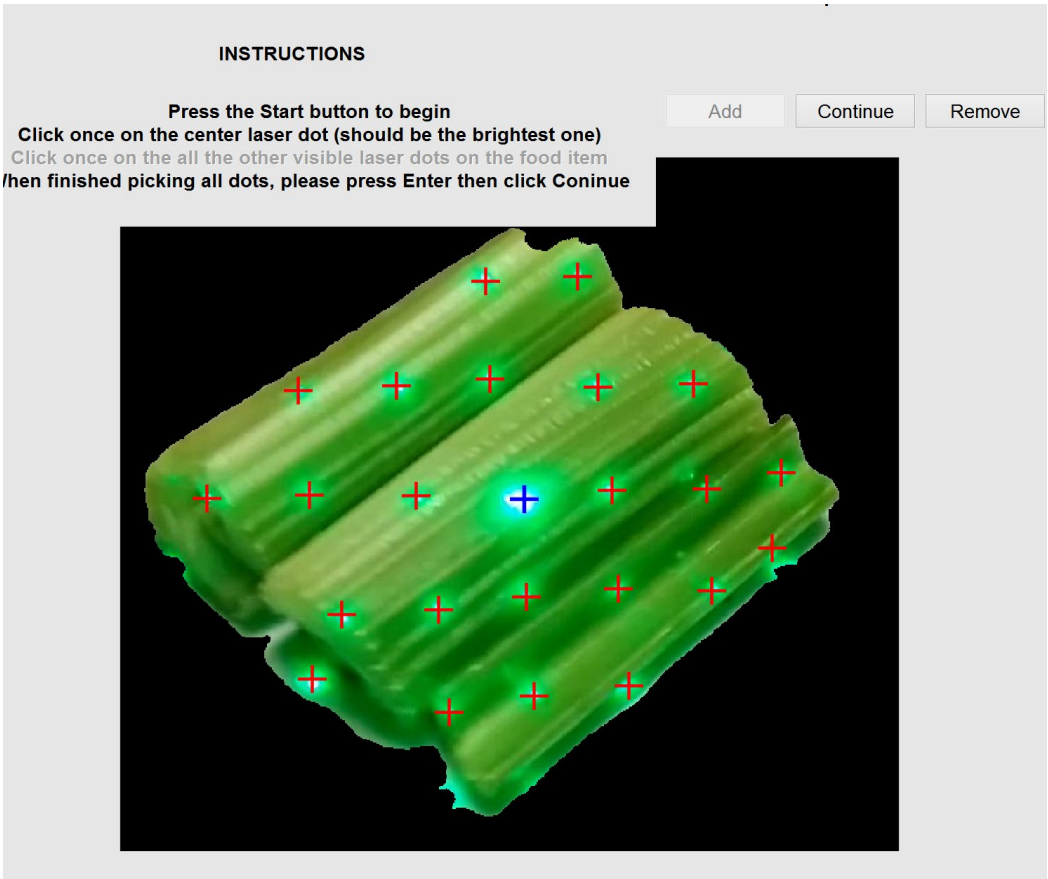

Figure 4.16. The final step, the Manual Dot Selection GUI, corrects the automation algorithm's errors. The user can correct the errors by using add, remove, and continue buttons. The red cross points on the image are the regular laser dots, while the blue cross point represents the center dot.

4.1.2.3 The Design of the 3D Reconstruction Modeling.

The calibration process plays an essential role in the accuracy of the 3D reconstruction. Unlike other calibration methods that consist of finding intrinsic and extrinsic parameters of the camera, this calibration method uses SLS in coordination with lasers to reconstruct the 3D object. The calibration process aims to determine the depth map of a white plane at a known distance. This reference depth map will aid in the construction of the depth map of any object scanned.

The calibration process is a set of initial recordings in a controlled environment with as many known variables as possible. This process on a DDRS unit is done by taking pictures of the laser

grid at different distances from the phone while measuring the 3D angle and maintaining the same accelerations. A white planar surface is used to project the laser grid and determine the pixel values of each dot in the image. Figure 4.17 shows the calibration system, which is called the DDRS calibrator, which operates automatically and eliminates human error. DDRS calibrator consists of a robotic mapping algorithm, which is based on the model of a single axis computer attached to a controlled cutting machine (CNC). A holder on a pair of rails driven by an Arduino-controlled stepper motor.

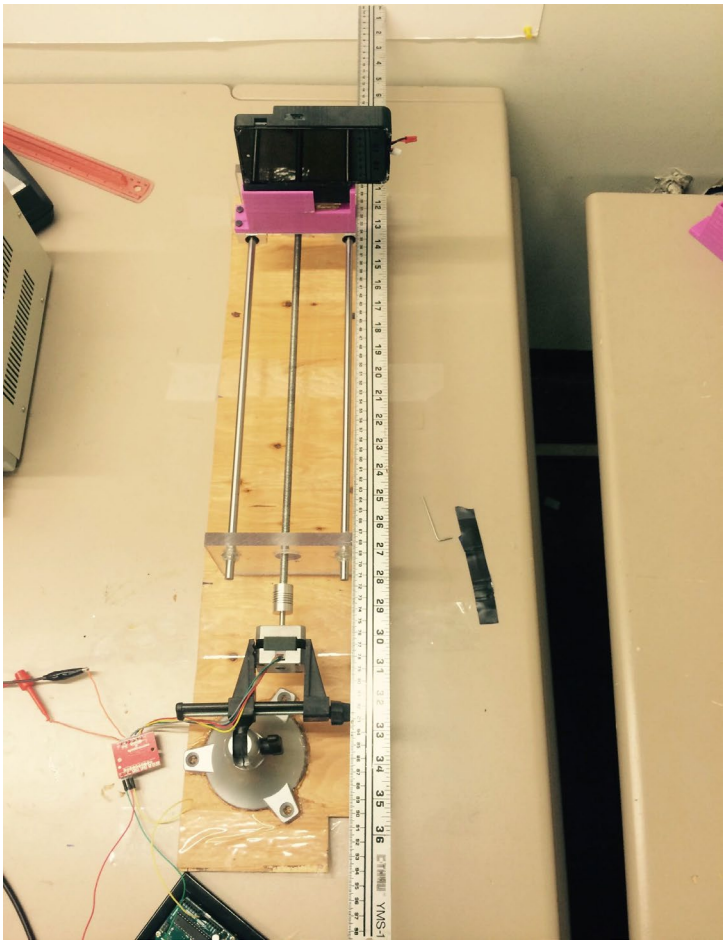

Figure 4.17. DDRS calibrator device. The DDRS device is mounted on the pink holder, which is then automatically operated by an Arduino microcontroller to move the device at a consistent speed (with respect to the recorder frame rate) and identical intervals.

Since accelerometer data is needed for later processing in the algorithm, a picture taken by the phone camera cannot be used. However, a picture can be easily extracted from a recorded video. At the beginning of the calibration, the phone must start far enough away from the white wall that all the laser dots on the plane can be seen on the screen, shown in Figure 4.18. Then, the video recording can begin by moving the phone 20 mm away from the plane and covering the camera to make the screen dark while the phone is moving. The black screen will serve as a delimiter for each video section related to a distance. This process is repeated by moving away from the plane in 20 mm increments up to 500 mm. After setting up the hardware and recording a video of the white plane at different distances, the algorithm is now ready to be used to process the image and generate calibration data.

Figure 4.18. A DDRS device in the process of calibration. The image of the projected SLS laser module is captured by the smartphone camera, which is then converted into calibration data for 3D reconstruction.

The average computational power of the smartphone affords a suitable resource for data collection, but it is not enough for the data processing. Therefore, acquired videos must be transferred to a cloud server for processing. The video sequence is first extracted to frames, and each frame is used to generate calibration data. Through calibration, a series of parallel and planar images within a valid range of depths are acquired from the camera, each containing a grid of dots. The laser dots' pixel positions in the image change as a function of distance from the image plane, forming a line segment that can be mapped in 3D space. The steps required to generate the calibration data are as follows:

1. Extract frames from the video.
2. Locate the center of the laser grid, and index the values of the neighboring points.
3. Generate calibration data.

Frames Extraction: The purpose of this algorithm is to extract frames from the video at varying distances. This process consists of converting video to frames and determines which frames contain the entire laser-pattern before the camera was covered. Next, only one image per delimiter is selected, and the results are saved with a name corresponding to the distance values (200.jpg, 220.jpg…. 500.jpg). The selected images will be processed by an algorithm to generate the calibration data.

Locating the Laser Coordinates and Index Positions: The rest of the calibration process requires locating the pixel coordinates of all the laser dots in each frame and mapping each laser dot to an index position. This will make it possible to keep track of the laser dot displacement as the camera moves away from the plane. An algorithm was designed specifically for locating the coordinates of green laser dots, which processes a single image containing the laser grid. It isolates

dots in the image by converting the image to grayscale and using the intensity of the light to distinguish dots from the image shown in Figure 4.19.

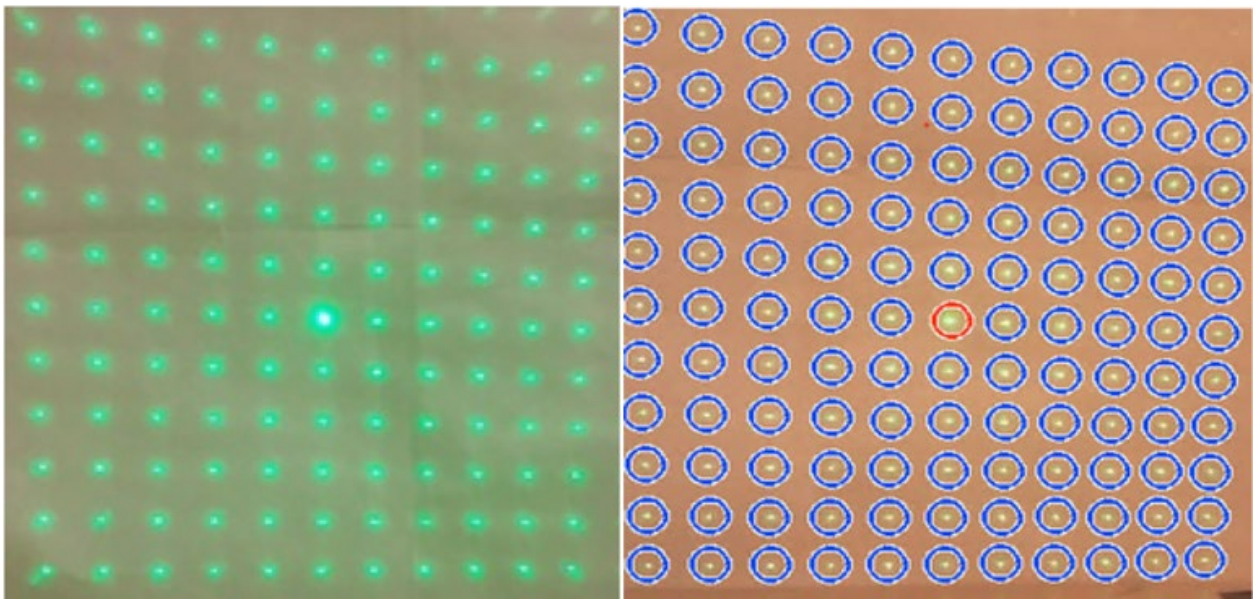

Figure 4.19. A snapshot of the laser point on the left, and a snapshot of the AutoDot detection algorithm processing the laser points for the calibration process on the right.

The algorithm generates a map that represents each dot as a field of a two-dimensional array. The idea is to find the distance from each point to the center. The smallest distance will be at the center point, so its assigned index is (0,0). The next four closest points are used to define the four quadrants (-1,0), (1,0), (0,-1), (0,1). Using these quadrants, each point can be mapped to an appropriate index, which will represent how far each point is located from the center (see Figure 4.20).

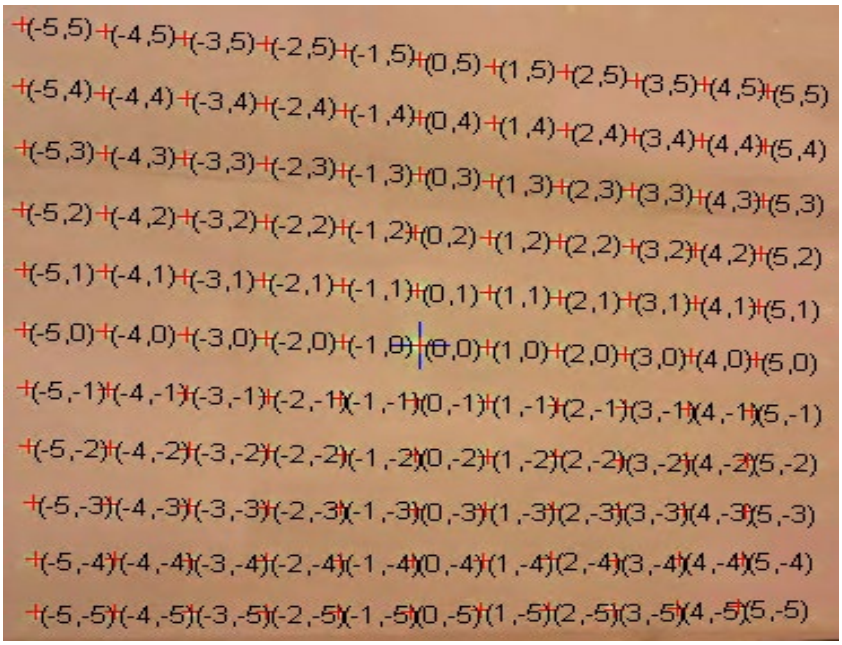

Figure 4.20. All coordinates assigned automatically for the calibration process by the algorithm.

Generating Calibration Data: The calibration data is a fundamental component for accurately calculating the position of the 3D points. The precision of the calibration data, especially the linear and nonlinear regression parameters, directly affects the accuracy of the 3D reconstructed shape. Assuming n images are extracted at equally spaced distances from the calibrating plane, the input data for generating calibration data are the sets of distances where frames are extracted, also explained further below in (15) - (17).

$$y = xm + b \tag{15}$$

$$Z = [Z_1, Z_2, Z_3, \dots, Z_n] \tag{16}$$

$$Z = \frac{G}{H + x} \tag{17}$$

where y, x, m, and b are the variables for the regression line; Z is the depth coordinate; G and H are the sensor data from the extracted frame.

There are then n structures, each of which has the 121 pairs of x and y values for each laser dot in the image. A single set of 121 coordinates can be visualized in Figure 4.21. The accumulated data is then used to calculate the calibration data.

11x11 struct with 12 fields

	1	2	3	4	5	6	7	8	9	10	11
1	1x1 struct	1x1 struct	1x1 struct	1x1 struct	1x1 struct	1x1 struct	1x1 struct	1x1 struct	1x1 struct	1x1 struct	1x1 struct
2	1x1 struct	1x1 struct	1x1 struct	1x1 struct	1x1 struct	1x1 struct	1x1 struct	1x1 struct	1x1 struct	1x1 struct	1x1 struct
3	1x1 struct	1x1 struct	1x1 struct	1x1 struct	1x1 struct	1x1 struct	1x1 struct	1x1 struct	1x1 struct	1x1 struct	1x1 struct
4	1x1 struct	1x1 struct	1x1 struct	1x1 struct	1x1 struct	1x1 struct	1x1 struct	1x1 struct	1x1 struct	1x1 struct	1x1 struct
5	1x1 struct	1x1 struct	1x1 struct	1x1 struct	1x1 struct	1x1 struct	1x1 struct	1x1 struct	1x1 struct	1x1 struct	1x1 struct
6	1x1 struct	1x1 struct	1x1 struct	1x1 struct	1x1 struct	1x1 struct	1x1 struct	1x1 struct	1x1 struct	1x1 struct	1x1 struct
7	1x1 struct	1x1 struct	1x1 struct	1x1 struct	1x1 struct	1x1 struct	1x1 struct	1x1 struct	1x1 struct	1x1 struct	1x1 struct
8	1x1 struct	1x1 struct	1x1 struct	1x1 struct	1x1 struct	1x1 struct	1x1 struct	1x1 struct	1x1 struct	1x1 struct	1x1 struct
9	1x1 struct	1x1 struct	1x1 struct	1x1 struct	1x1 struct	1x1 struct	1x1 struct	1x1 struct	1x1 struct	1x1 struct	1x1 struct
10	1x1 struct	1x1 struct	1x1 struct	1x1 struct	1x1 struct	1x1 struct	1x1 struct	1x1 struct	1x1 struct	1x1 struct	1x1 struct
11	1x1 struct	1x1 struct	1x1 struct	1x1 struct	1x1 struct	1x1 struct	1x1 struct	1x1 struct	1x1 struct	1x1 struct	1x1 struct
12											

Figure 4.21. Complete set of calibration data in an 11x11 struct format.

1x1 struct with 12 fields

Field	Value
minXIdx	-5
minYIdx	-5
xIdx	-1
yIdx	-5
aCoef	[5.1784e+04,-127.7267]
numPoint	18
m	0.5960
b	219.5237
r	0.9994
mRobust	0.5963
bRobust	219.4610
pointArray	*18x7 double*

Figure 4.22. Calibration data fields for each laser dot, which represents each cell of the full matrix shown in Figure 4.21.

4.1.2.4 The Volumetric Calculation.

Images of food samples on a plate are first captured using a smartphone. The images, with the smartphone's sensors information, are then imported to collect the depth data for 3D reconstruction. The food from the image is segmented with saliency mapping auto-cropping, and then a source pixel is located to construct a 3D line segment to a range of depth guesses. Then, the Automatic Dot Detection algorithm locates the laser dots in a segmented image using an HSV filtered cosine similarity mask and a luminance mask. The laser dot coordinates are then passed through the 3D rotation algorithm to model the object. The 3D points are first calculated, then the 3D image is reconstructed. Finally, the volume is calculated by closing the 3D model spatially (see Figure 4.23.) The following sections will describe the calibration process and the 3D reconstruction algorithm.

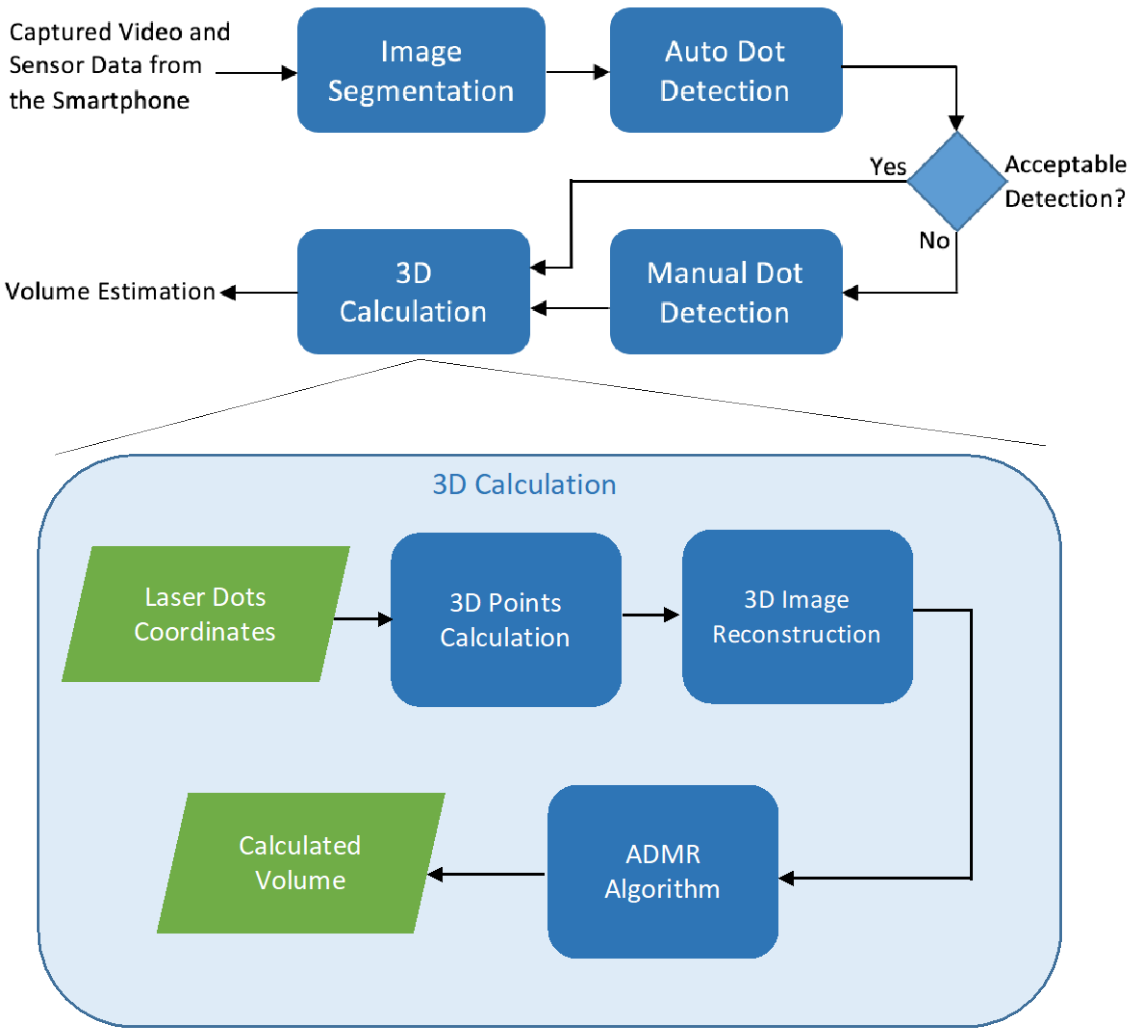

Figure 4.23. 3D Calculation flowchart. The figure shows the architectural design of the volumetric measurement algorithm.

4.1.3 The Functional Design of the DDRS Smartphone Application

Additional user input is required to estimate the dietary nutrients for a specific food or dish. The prompts have been simplified and designed for a 5th-grade education level. The user can identify food items through a variety of methods, including typing the names of the foods, using voice recognition to speak the names, or, if the food is known in the DDRS cloud library, then the user can simply click on the graphic icon. The user is prompted with the ability to scan relevant recipes or other information to assist with data collection; otherwise, the user can identify the

components of the meal, such as the name of the food item or dish, and, in some cases, the ingredients of a dish/recipe. The smartphone application stores, shares, and scans recipes; after scanning the plate of food, the user also has the opportunity to link the scan to preexisting recipes on the shared and local cloud database to get the ingredients of the scanned dish. The user can save new entries to the cloud and share their recipes with other users and nutritionists. Like similar technologies, the DDRS uses a cloud library of food items and has been designed to accommodate new foods through user input and crowdsourcing easily. The user is also able to manage all entries and organize them as different graphs focusing on chosen nutritional categories by the user. Representative screenshots of this process are shown in Figure 4.24.

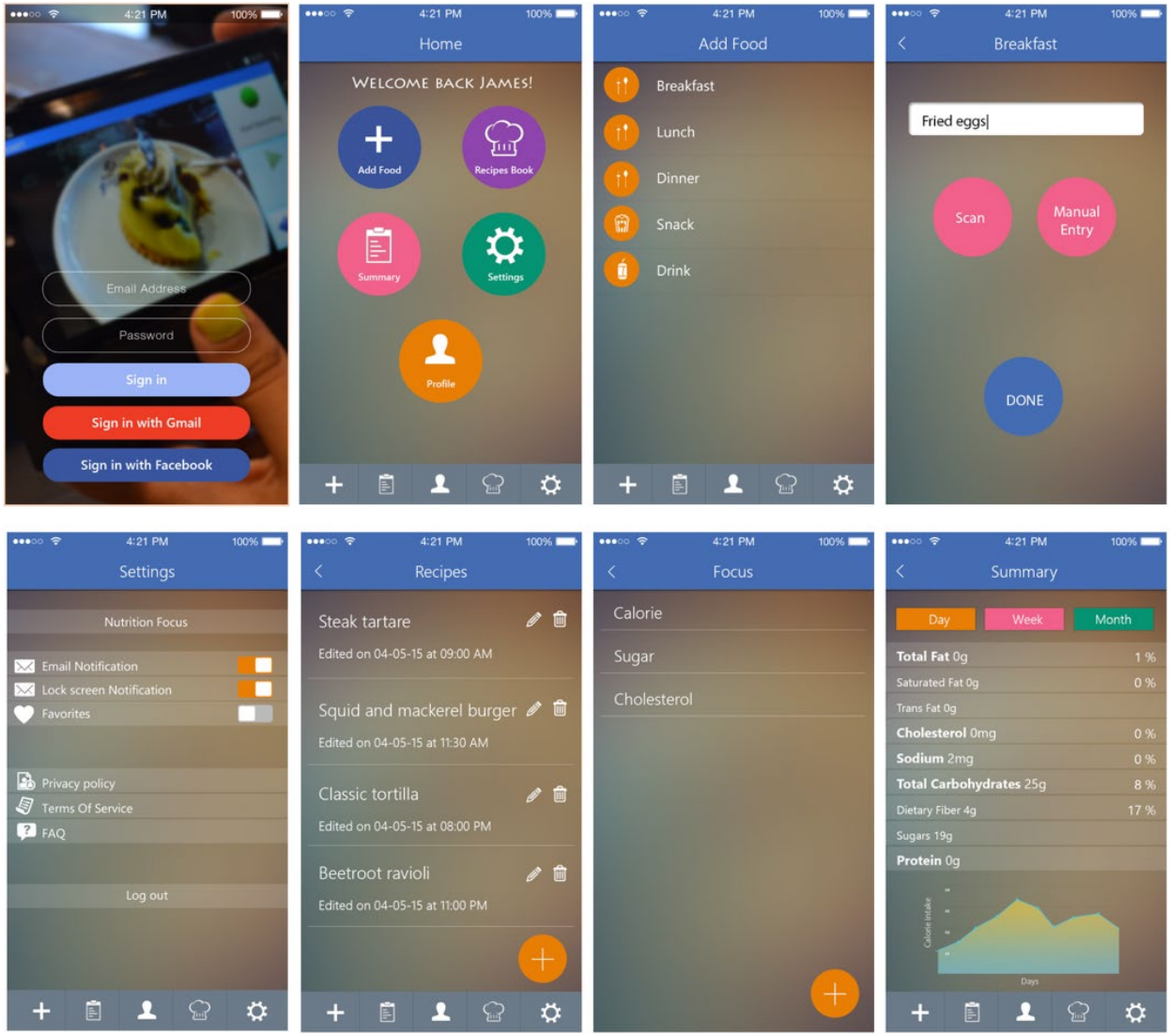

Figure 4.24. Demonstration of the process of entering food items and recipes using the DDRS smartphone app.

4.2 The Functional Design of the DietSkan System

Diabetes is a global health issue, with an estimated 30.3 million people affected in the United States alone [65]. Diabetes is a disease characterized by the body's impaired ability to produce or respond to insulin, resulting in abnormal metabolism of carbohydrates and elevated levels of glucose in the blood and urine. The associated conditions include cardiovascular diseases,

musculoskeletal disorders, and cancers [66]. Enhanced dietary assessment techniques are critical for maintaining a healthy life for a diabetic patient.

Moreover, hospitals must monitor their diabetic patients' food intake to prescribe the correct amounts of medication. Malnutrition is a long-standing issue for hospitalized patients, and, nationwide, 30 to 50% of patients are diagnosed with it [67]. Additionally, nursing and nutrition staff are only able to assess approximately 50% of meal trays due to the staffing levels and logistics involved in meal delivery and pickup (Harborview Medical Center internal data). This paper presents a novel method called the DietSkan system (shown in Figure 4.25), which uses 3-dimensional (3D) scanning technology to measuring the volume of a food item and calculate the exact nutritional intake.

The DietSkan system uses automatic 3D reconstruction using a Commercial Off the Shelf (COTS) depth camera and the existing nutritional database provided by the medical center's kitchen to determine the actual amount of consumed meal in less time and cost compared to similar solutions. The DietSkan smartphone application is used to capture the leftover food volume on a patient's plate, and the Volumetric Calculation Algorithm (VCA) is used to measure the nutritional data of the leftovers. Once the measurement is done, the DietSkan system uses the reported nutritional data provided by the medical center's kitchen to subtract and measure the consumed amount to be reported to the physician.

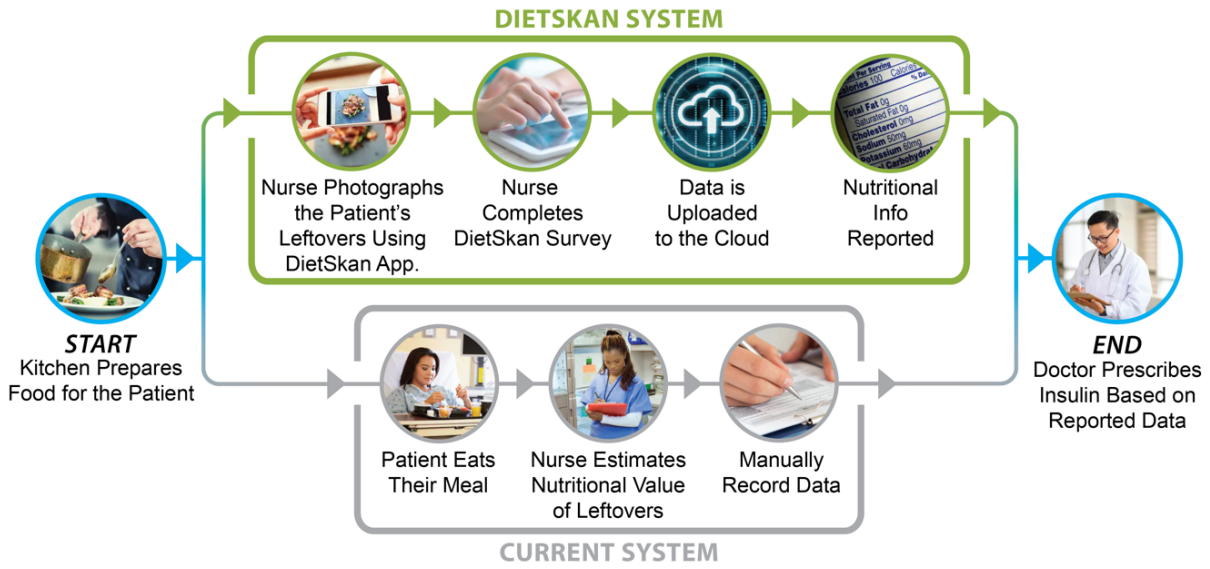

Figure 4.25 The DietSkan system replaces the existing estimation process by introducing an automated smartphone application to measure the leftover food volume on a patient's plate and subtracting the reported nutritional data provided by the medical center's kitchen to measure the consumed amount and report to the physician.

The DietSkan system looks to improve dietary measurement monitoring in hospitals by calculating the consumed nutritional data. Most U.S. hospitals measure the exact amount of food before sending it to the patient and record it to the facility's nutritional database. Access to this database allows the DietSkan system to obtain the base nutritional data of the meal. Once the patient is finished eating, the nurse or the nutritional staff scans the leftovers using the DietSkan smartphone application. The application collects the depth data from a COTS depth sensor called Structure Sensor (made by Occipital [68].)

Post-processing of the 3D models is done using the VCA algorithm, which outputs the volume of each segment of the mesh by filling any missing spatial holes. The obtained volumes are then subtracted from the originally recorded nutritional data by the kitchen to calculate the exact consumed nutrient by the patent. With this data, the person in charge can reliably prescribe and administer the required amount of insulin.

4.2.1 Structure Sensor

The structure sensor consists of an infrared (IR) projector and camera module to record depth information. The IR projector module projects a known scattering matrix of infrared light onto an object's surface. The scanner hardware used is the DietSkan system is shown in Figure 4.26.

Figure 4.26 A user is holding an iPhone with the Structure Sensor.

The IR camera receives the distorted matrix, which is warped by the object and sends the information to the device to calculate depth using the relative distance between the matrix's vertices. The hardware requires a smartphone application to operate. Structure IO provides an open-source algorithm for 3D reconstruction, which can be integrated into a smartphone application. During the scanning process, the user takes a live scan (video) of the plate from different points of view using the smartphone application. The application dynamically generates a 3D mesh using these frames and displays it on the screen. The system also uses the host device's gyroscope to gather orientation data, which is useful when composing the 3D mesh. Mesh formation occurs by capturing the scene in focus from multiple angles, ideally capturing the edges

on the bottom surface. Once the application determines that the mesh has been entirely generated, the mesh is ready to be uploaded to the server with the user's confirmation. The process of scanning and uploading an object using the DietSkan application takes under two minutes; the average time spent on each meal is over 15 minutes (Harborview Medical Center internal data.)

4.2.2 Volumetric Calculation Algorithm (VCA)

The 3D mesh data is obtained in the form of an object file containing the vertices that comprise the triangular mesh and a preview JPEG image taken by the camera during the scanning process. The obtained mesh has imperfections due to blind spots during image capture as well as the boundary between individual food items and the plate; hence, the volume cannot be calculated accurately. The data is post-processed to obtain the items of interest, eliminate the remaining regions of the scan, and fix any imperfections that are present. Finally, the volume is calculated on the processed mesh.

From the generated mesh, the plate is first segmented and removed, and then the resulting hole is filled, as shown in Figure 4.27. At this point, the user manually selects the individual food items, and this splits them into individualized volumes. When the mesh is divided in such a manner, it produces multiple smaller meshes with defects in them, primarily holes. These holes must be closed for the volume of the items to be accurately calculated. Each segment selected is closed by filling the holes generated, and the closed meshes are then used to calculate the volume for each item. Nutritional data is computed for each identified volume.

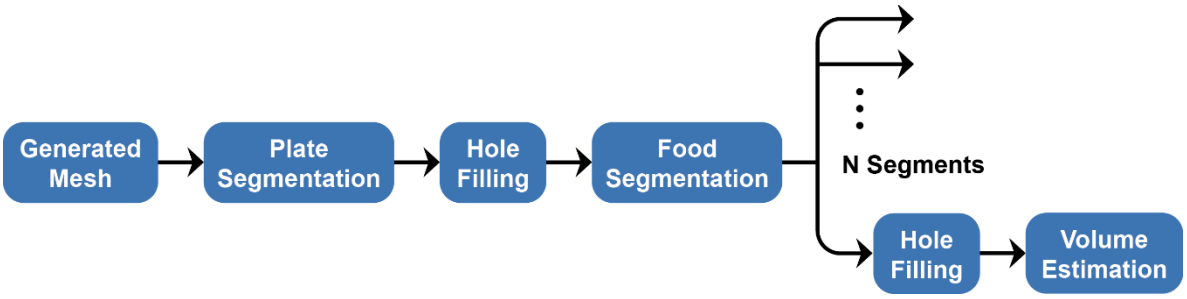

Figure 4.27. Flowchart of the DietSkan volume estimation pipeline. The generated mesh is passed as input to the pipeline, and the calculated volumes of each food segment are sent as output. Plate and food segmentation were done separately to reduce errors and ensure only a single hole was presented at any stage of the pipeline.

Most of the post-processing was done using Autodesk Meshmixer, a free 3D reconstruction tool [69]. This application was chosen over several other tools due to its simplicity to segment individual items in the scan and the ability to perform the volume calculation with high accuracy. While Meshmixer can also be used for filling holes, that was done independently to obtain better flexibility in this process and choose an algorithm best suited for the type of mesh being handled.

Segmentation of the plate, as well as the individual food items, were done within Meshmixer. After filling the generated holes, Meshmixer calculates the volume of the object. The post-processing time is typically between one to three minutes per food item; however, this process can be integrated into the main algorithm in the next version of the application.

While hole-filling is necessary for generating the volume, it is well known that it can introduce errors due to the inexact production of the hole [70]. Since hole-filling algorithms are used in a variety of situations, the requirements for such an algorithm can vary from application to application. The general criteria that such an algorithm should satisfy is given by:

1. Produce a non-self-intersecting watertight mesh.
2. Process arbitrary holes in complex meshes.
3. Avoid changing, approximating, or re-sampling the original data away from the holes.

4. Incorporate user-provided constraints to allow the selection of multiple topologically differing solutions.
5. Process large scanned meshes with a running time proportional to the size of the holes, rather than that of the input mesh.

For the DietSkan use-case, the focus was on the first three requirements when searching for a suitable algorithm. The input mesh is expected to be of a reasonably consistent size, and user input was kept to a minimum. Thus, points four and five were not of high priority.

To help identify an appropriate algorithm based on the specific application requirements, currently available methods were reviewed with the help of [71]. Algorithms based on polygonal representation were looked at specifically, and the comparison table was used to select the method of choice. Based on the features considered and tabulated in the comparison, the technique described in [72] was selected. As described in the paper, the main steps for the algorithm are:

1. Identify holes in the triangular mesh.
2. Generate the initial patch mesh using the Advanced Front Mesh (AFM) technique [56].
3. Refine the patch mesh based on the Poisson equation.

The generated meshes were scanned and analyzed to identify and characterize the holes present in them. Typically, holes appeared at the region of intersection between two neighboring food items as well as the plate. The processing pipeline was developed to ensure that there was only a single hole formed at any given stage, enabling the algorithm to work effectively. Once the hole is identified, Figure 4.28 shows the algorithm used to fill the holes.

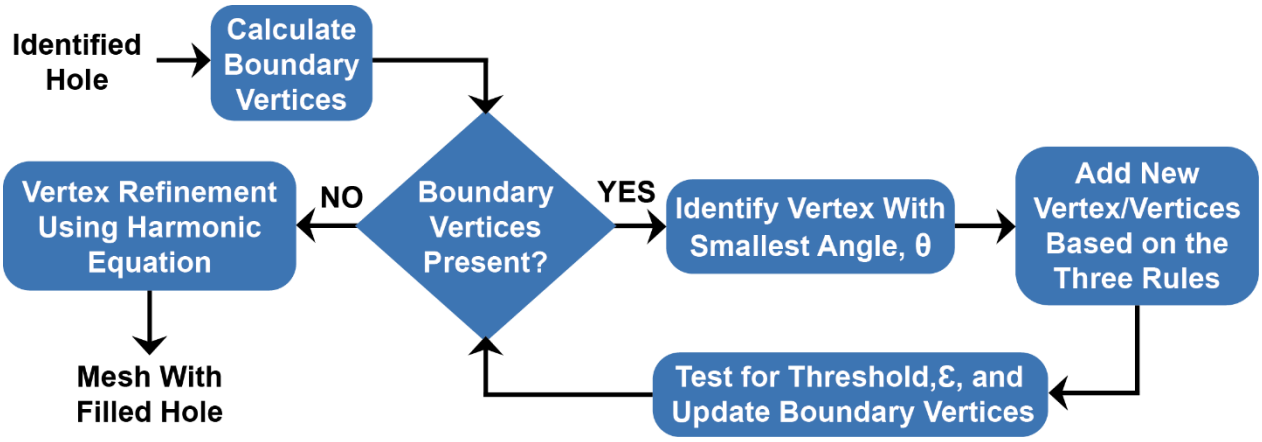

Figure 4.28. Algorithm flowchart for hole filling. Each identified hole is run through this.

The AFM technique uses a simple, iterative approach to generate a new patch. The boundary vertices of the hole v_i are identified, their edges calculated $(e_{i-1,i}, e_{i+1,i})$ and the angle between the edges θ_i. The algorithm starts with the vertex of the smallest θ, and then proceeds to each adjacent vertex adding new triangles (and vertices, if needed) to the mesh. After each addition, the vertices hidden by the newly formed triangle is removed from the boundary vertex set, and the new vertices are added to the set.

The positions of the new vertices are primarily based on three rules, depending on θ_i as shown in Figure 4.29. When $\theta_i \leq 75°$, the three vertices (v_{i-1}, v_i, v_{i+1}), are connected directly to form the new triangle. When $75° < \theta_i \leq 135°$, a new vertex v_n is added on the bisector of the edges $(e_{i-1,i}, e_{i+1,i})$, lying on the same plane formed by the two edges, with the average edge length of the edges. For $\theta_i > 135°$, two new vertices are added (v_{n1}, v_{n2}) on the trisector of the edges $(e_{i-1,i}, e_{i+1,i})$, with the average edge length of the edges.

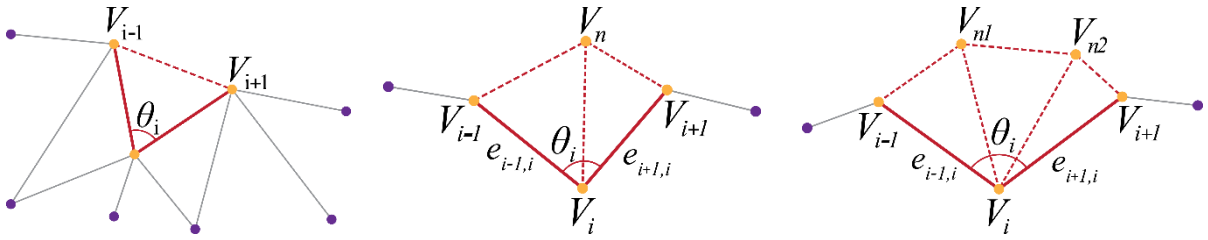

(a) (b) (c)

Figure 4.29. The three rules for new the vertex generation, depending on vertex angle θ_i: (a) for $\theta_i \leq 75°$, (b) for $75° < \theta_i \leq 135°$, and (c) for $\theta_i > 135°$. v_i refers to the vertex in focus with the associated angle θ_i, (v_{i-1}, v_{i+1}) refer to the two adjacent vertices, $(e_{i-1,i}, e_{i+1,i})$ refer to the two edges connecting the adjacent vertices to v_i and, v_n , (v_{n1}, v_{n2}) refer to the newly added vertices. These vertices were generated in the holes produced during DietSkan post-processing to achieve watertight meshes.

However, the addition of new vertices given by the above three rules could cause a vertex to be added within an already defined triangle or very close to an already existing vertex. While the former causes problems with mesh formation, the latter is also inefficient and produces a more cluttered mesh. This problem is addressed by selecting a threshold, ∈, to form a radius around all existing vertices. When a new vertex is generated, the distances to the surrounding vertices are calculated. If any distance is less than ∈, an existing one replaces the vertex. An example of such a scenario is shown in Figure 4.30. The generated vertex, v_{n2} is within the threshold distance from an existing vertex $v_e$and hence, the triangle is formed with v_e. In the case that there are two or more possibilities, the selection which would result in the closest triangle to an equilateral triangle is preferred.

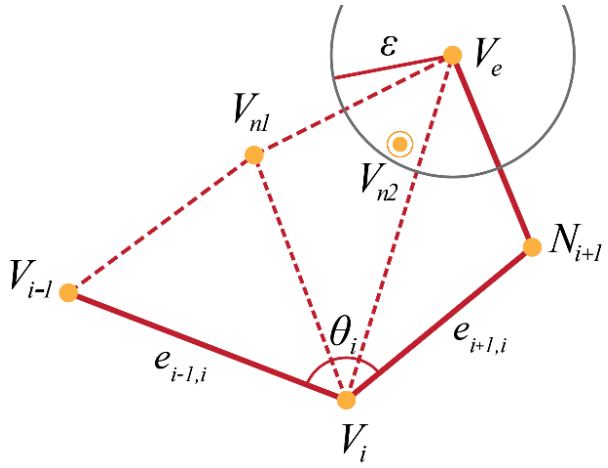

Figure 4.30. The threshold to check for overlaps and reduce mesh complexity where v_e is an existing vertex within a radius of ∈ to the proposed vertex v_{n2}. For the DietSkan application, larger values of ∈ were experimented with to simplify the mesh as much as possible to be computationally effective while retaining the general 3D geometry.

The generated patch is then refined to produce a more accurate filling. The refinement proposed, based on the Poisson equation, was not entirely implemented to reduce algorithm complexity. From analyzing some partially processed meshes, it was found that most holes produced from the mesh were planar due to the propensity of food lying flat on a plate or with insignificant vertical curvature. For this reason, a refinement of the vertices based on harmonic functions was done without performing the additional steps of solving for normal, triangle rotation and mesh reconstruction using the Poisson equation.

Given a triangle $T = (v_1, v_2, v_3)$, the discrete harmonic function is used to find a basic piecewise mapping to minimize the Dirichlet energy given in (18),

$$E = \frac{1}{2}\int_{S_T} \|grad_{\mathrm{T}} f\|^2 \qquad (18)$$

where S_T refers to the surface of triangle T, $grad_T$ refers to the gradient vector of the vertex within T, and f refers to an unknown scalar function.

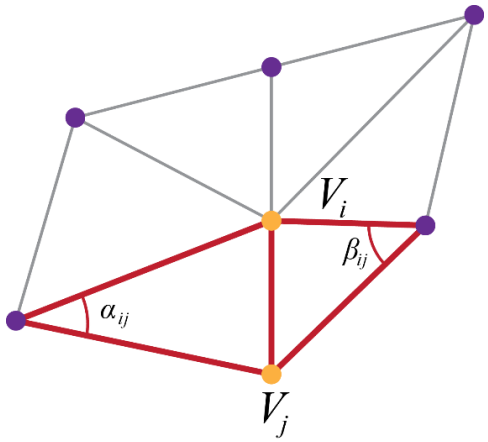

Figure 4.31. Angles and vertices for harmonic-based vertex calculation. The angles $(\alpha_{i,j}, \beta_{i,j})$ are used to calculate the gradient between vertices.

The harmonic function is applied to a set of vertices called the 1-ring vertices surrounding any given vertex in the generated mesh. 1-ring vertices are defined as the set of vertices directly adjacent to the vertex being examined. For the vertex v_i, the discrete Laplacian operator is given by (19):

$$\Delta f(v_i) = \sum_{v_j \in N_i} \frac{1}{2}(\cot \alpha_{i,j} + \cot \beta_{i,j})(f_i - f_j) \tag{19}$$

where f_i is one of the coordinates of v_i, $(\alpha_{i,j}, \beta_{i,j})$ are the two angles opposite to the edge $e_{j,i}$ and, N_i is the set of 1-ring vertices of v_i. Therefore, it can be shown that the minimization problem can be expressed as (20):

$$\sum\nolimits_{v_j \in N_i} \omega_{i,j} \left(f(v_j) - f(v_i)\right) = 0, \qquad v_i \in V_I \tag{20}$$

where $\omega_{i,j} = \cot \alpha_{i,j} + \cot \beta_{i,j}$. Solving for this linear system three times for each component (x, y, z), the newer vertices are generated, and the mesh is modified. As noted in the paper, by only performing this step, the resulting mesh is depressed, and it does not work well with items with larger curvatures.

4.2.3 Nutritional Data Calculations

The volume data of the leftover meal is then converted into nutritional data using available databases. Food density data were obtained from the Nutrition Coordination Center (NCC) [73], and the volume is converted to its estimated weight given by (21):

$$W = V * D \tag{21}$$

where *W* is the weight of the meal, *V* is the measured volume of the meal, and *D* is the density factor from the NCC database.

The estimated weight is then converted to nutritional data by looking up the nutritional information per gram of a given food item. The nutritional content per gram is multiplied by the weight of the food item found in the system, generating estimated nutritional information for each participant's reported consumption, as shown in (22),

$$CN\ (i) = W * \frac{ND}{g}(i) \tag{22}$$

where *CN* is calculated nutrient, *ND* is nutritional data (*i*), and it refers to each dietary component measured, such as calories or fat, *W* is the weight and g is the gram.

The calculated nutrient is then subtracted by the initially reported amount by the facility's kitchen using (23):

$$CoN = RN - CN\ (i) \tag{23}$$

where *CoN* is consumed nutrient, *RN* is reported nutrient, which is provided by the kitchen, and the *CN* is calculated nutrient of the left-over meal.

The consumed nutrient is then uploaded on to the patient's file to be accessed by the physician for an accurate prescription and overall diagnosis.

4.3 CHAPTER SUMMARY

The 3D-based VBM framework was used to develop the DDRS and the DietSkan system. The DDRS is a customized smartphone add-on, which enables depth estimation using a multilayer structured light plane reference. In addition to the depth estimation, the DDRS algorithm uses the following image processing steps to create a spatially closed 3D model: image segmentation, AutoDot detection (calibration), and 3D reconstruction.

The DietSkan system has a very similar process as the DDRS; however, the DietSkan system utilizes the advancements in ToF sensor technology to develop a more sophisticated algorithm to increase the adaptability of the system. The presented system showed improved adaptability to different hardware electronics as well as different environments. This feature opens the door for hospitals and consumer application uses.

Chapter 5. EXPERIMENRAL DESIGN OF THE DDRS AND THE DIETSKAN SYSTEMS.

5.1 EXPERIMENTAL DESIGN OF THE DDRS SYSTEM

To test the design of the DDRS system, the following four functions of the image processing algorithm were evaluated: 1) image segmentation, 2) AutoDot detection, 3) 3D reconstruction modeling, and 4) volumetric calculation.

5.1.1 Testing of the Image Segmentation Algorithm

In this section, the current status and results of the segmentation algorithm are described and analyzed. The initial image crop bounds the image to the white plate, the second image crop-bounds it to the object of interest. The saliency map is used to create an entirely segmented image on top of a black background [74]. The input and output pairs in Figure 5.1 demonstrate the results of running this algorithm on several test images.

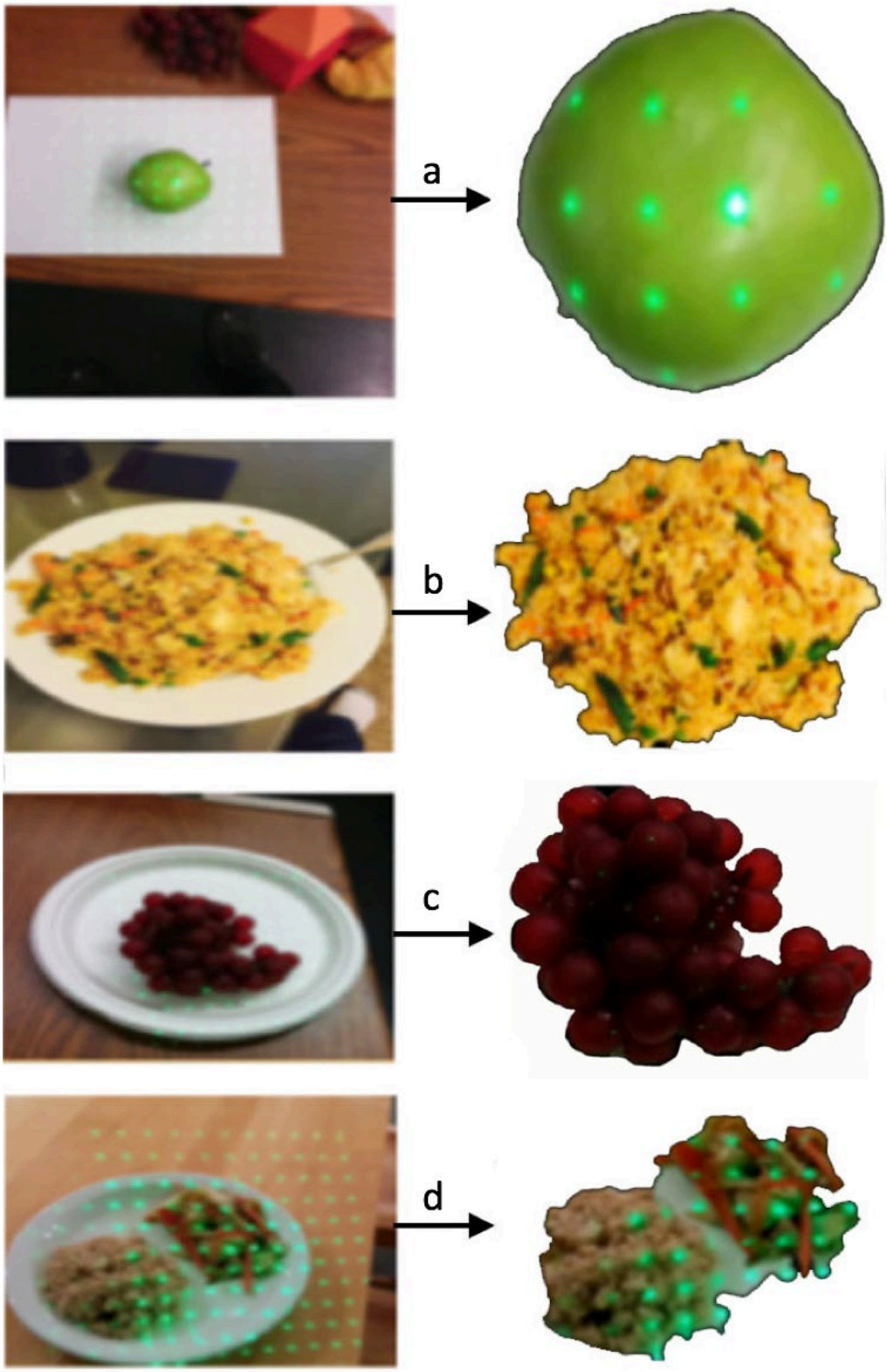

Figure 5.1. Demonstration of the algorithm's performance on multiple food items with different colors and shapes: a) green apple, b) yellow rice, c) grapes, d) white rice and red peppers.

The images in the left column of Figure 5.1 show the original samples from a video taken by a user. These images contain no pre-processing work, and, as a result, contain a lot of background noise—including the plate itself [75]. The right column of Figure 5.1 represents the final output of the segmentation algorithm for each food item.

As described previously, the algorithm is highly accurate for images with single food items—as shown in (a, b, and c) of Figure 5.1. However, in the last item (d) of Figure 5.1, an error is visible. Despite this, we have further optimized the accuracy of this algorithm using linear optimization to aid in segmentation cases with multiple objects.

To accurately measure the saliency mapping approach, we tested many different items, allowing comparisons of the calculated area to the area value yielded by an accomplished open-source algorithm called Simple Linear Iterative Clustering (SLIC) Superpixel Segmentation [76]. This algorithm was chosen to test against the DDRS segmentation algorithm because it has been thoroughly evaluated, producing accurate results that we can use to determine the accuracy of the DDRS algorithm.

First, we will look at the results from testing single objects on a white plate. Figure 5.2 shows the accuracy percentage of the absolute difference between the calculated segmented area using SLIC Superpixel Segmentation and measured the segmented area using the DDRS algorithm. The overall average error percentage for single items on a plate is 5%.

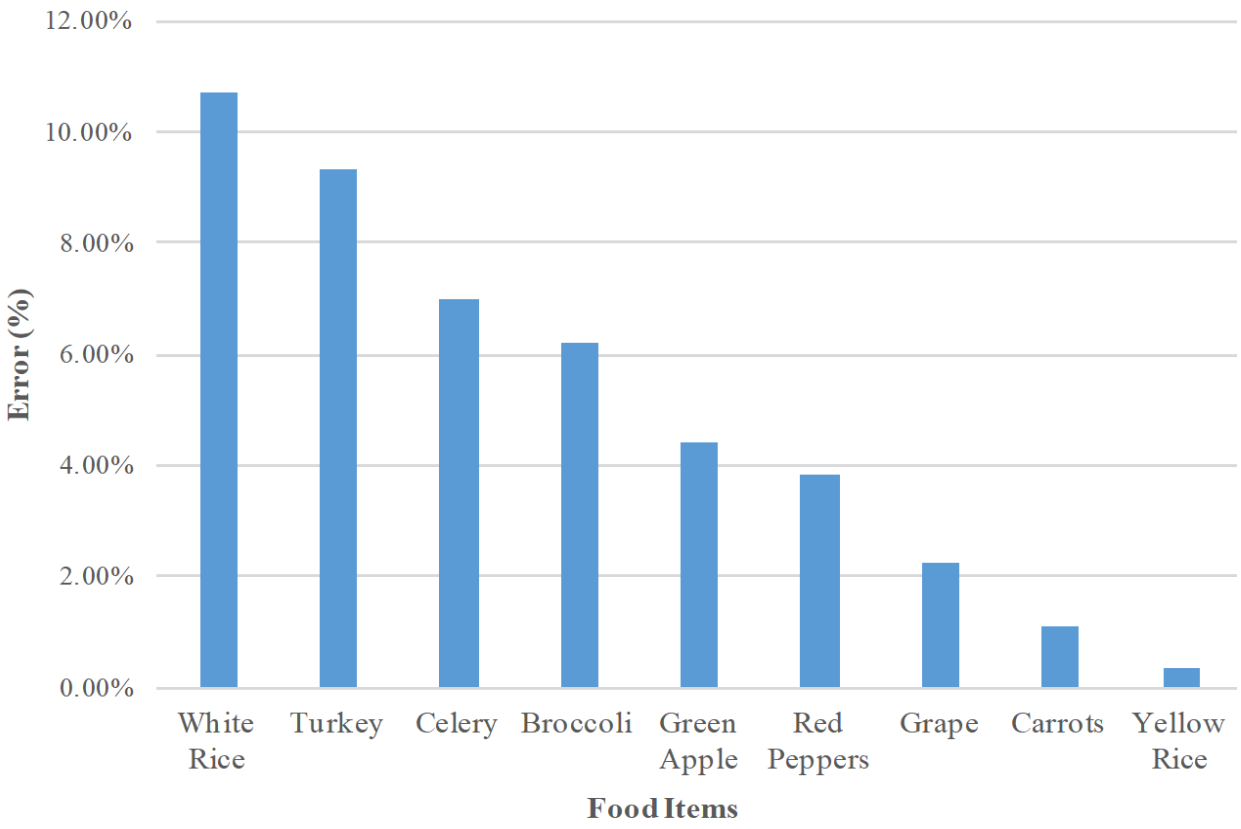

Figure 5.2. Percentage error of single item plates between the calculated segmented area using SLIC Superpixel Segmentation and measured segmented area using the DDRS algorithm.

Next, we look at the different tests conducted on the same food items, as presented in Figure 5.2. This time, however, we combine all the food items with another food object on the plate, similar to Figure 5.1 (d). Using the same method as the single food plates, we calculate the absolute percentage error using SLIC Superpixel. Figure 5.3 shows the percentage error for multiple food plates. The overall average error percentage for multiple items on a plate is 7.16%.

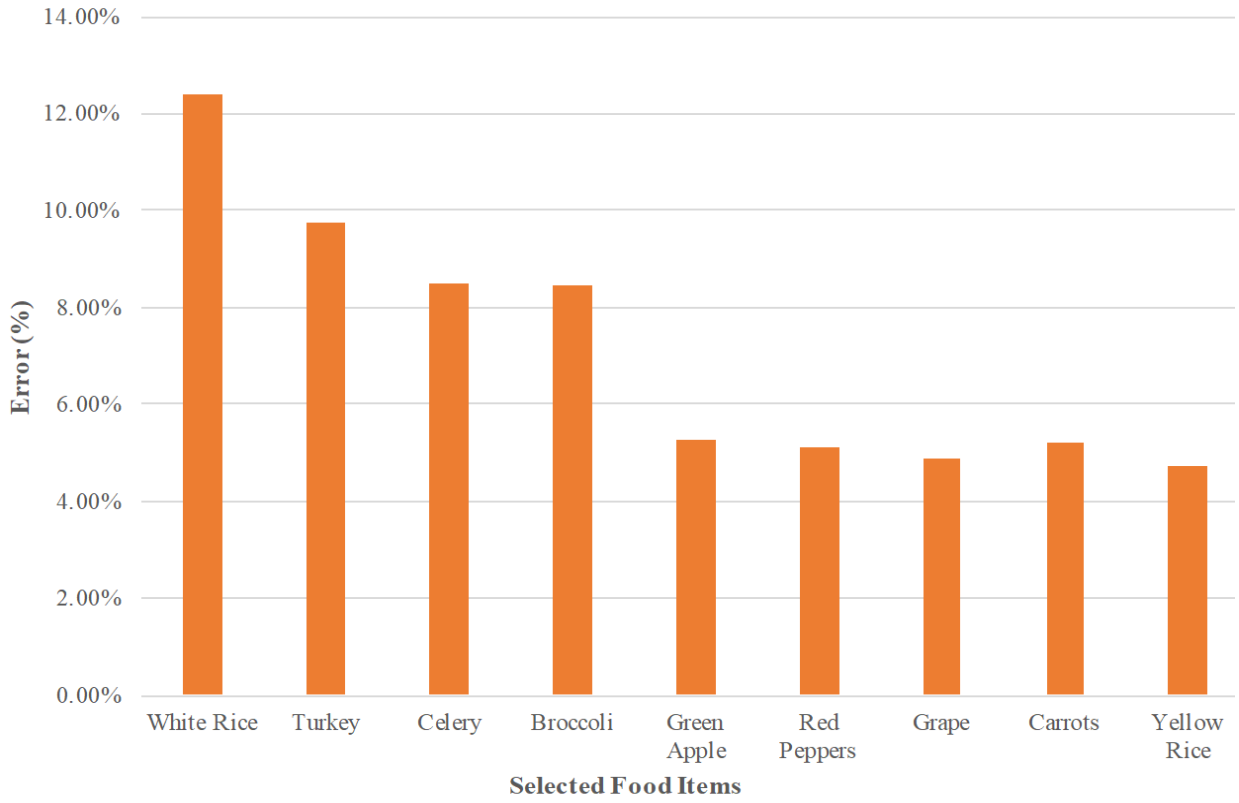

Figure 5.3. Percentage error of multiple food plates between the calculated segmented area using SLIC Superpixel and measured segmented area using the DDRS algorithm.

As seen in both Figure 5.3 and Figure 5.3, the percentage error is higher on multiple food plates compared to single food items. In both graphs, there is also a trend directly related to the color of the item being segmented. Figure 5.4 shows both single item plates and multiple food plates side by side to show this trend.

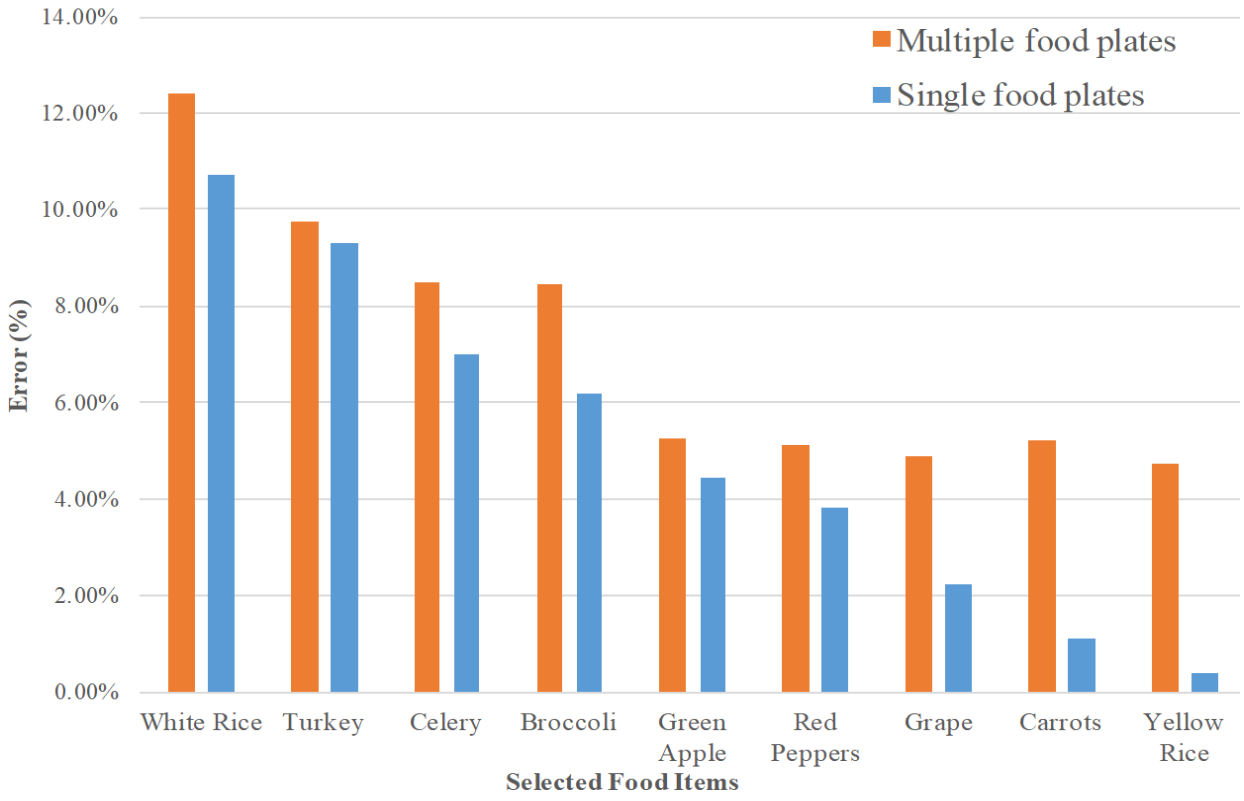

Figure 5.4. Percentage of error comparing several food items on a plate, where the error is determined by comparing the segmented area of DDRS and SLIC Superpixel Segmentation algorithms.

The sources of error come from the distinct color characteristics of the images, and the algorithm's static thresholding values. This can be attributed to the limitations discussed in Chapter 9.1. Figure 5.4 shows all the food items scanned to analyze the segmentation algorithm's performance. By analyzing the population of the data points and color characteristics of the scanned food items in Figure 5.5, we can observe that the food items in the near-white color category tended to have the highest errors in segmentation. Also, food items in the red category tended to have the lowest percentage of error.

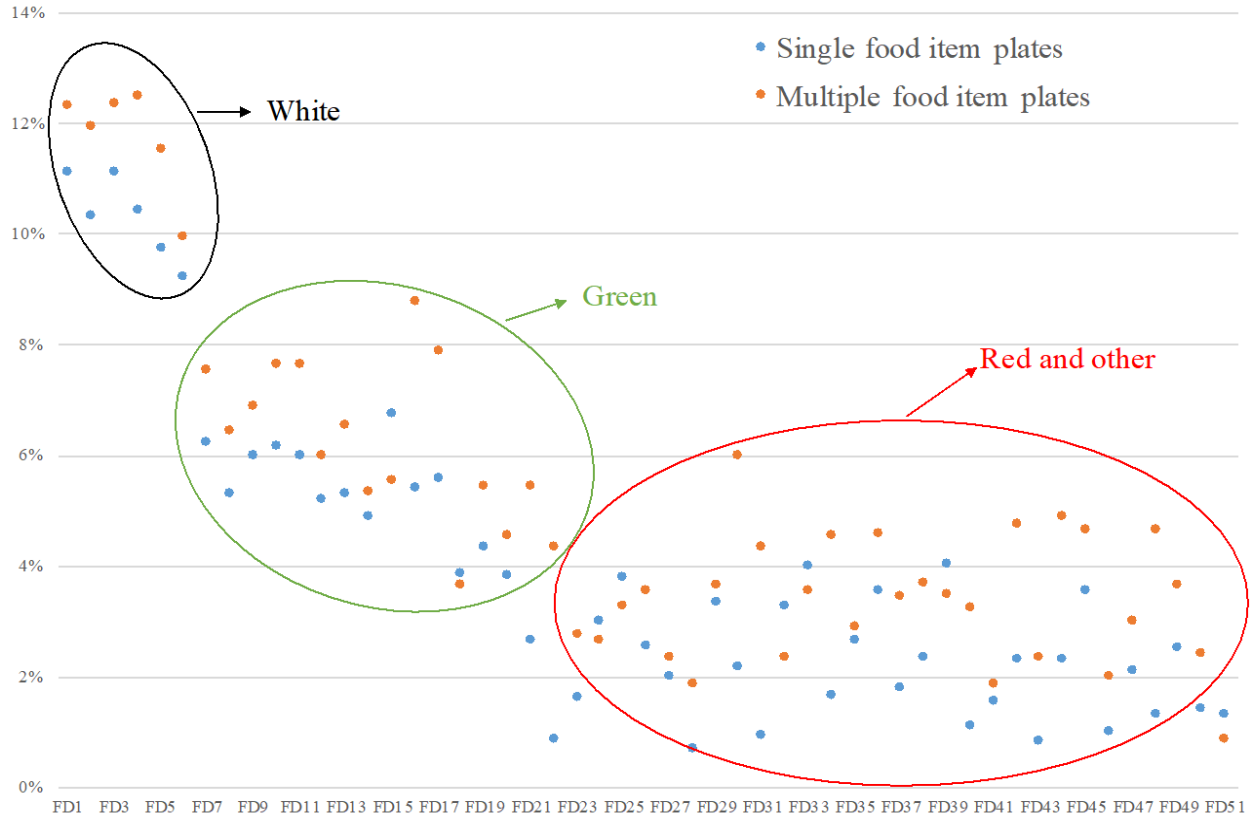

Figure 5.5. A larger sample size of percentage error calculated with both single and multiple food plates.

We then analyzed the data to find patterns that might indicate the greatest sources of this error, discovering that when different objects were combined and tested, the error was higher than when the same objects were tested individually. We also noticed that similarly colored objects had similar percentages of error.

From these results, it is evident that the algorithm is highly accurate, capable of segmenting a multi-food plate in less than a minute—especially when analyzing single-object images. This accuracy dropped, however, when segmentation was used on multiple-object images. With further investigation, we noticed some reoccurring patterns in images with low accuracy results, based on two main categories: the single-object vs. multiple-object images, and their corresponding object

colors. There was an overall error average of 9.34% for single objects, and 8.05% for multiple objects.

As for the color-based analysis, the segmentation of the white objects had the poorest volume measurement when compared to SLIC Superpixel Segmentation. Due to the similarity in color to the white serving plates, whiter foods can be misinterpreted as part of the background plate, and unnecessarily segmented from the image [77]. Thus, the color of the food plays a more important role than the number of food items in an image.

Another important result of this analysis was that the green objects were the second-highest percentage of error. This is primarily because the projected laser dots were green, which caused there to be a lack of contrast between the dots and the food items being measured. This shows that the hue of the object presents a limitation to the algorithm and that the static thresholds in the algorithm must be made dynamic to enhance the segmentation process.

5.1.2 Automatic Dot Detection

This section presents and analyzes the current results of running the AutoDot detection algorithm of the DDRS. The algorithm is tested by comparison of the accurate laser dot location in space and the detected one by the algorithm. Figure 5.6 shows the results of dot locations on a small subset of sample images used for initial testing.

Figure 5.6 shows the dots are detected more accurately when there is an apparent contrast between the dots and the color of the food. Some of the limitations are visible in (d), where several dots were not detected on the border.

The failure to detect dots on the border is due to the limitation of the static variables discussed in the analysis section. Several tests were run to compare the current algorithm to previous versions. The experiment was conducted on a group of objects using AutoDot detection, and then

the number of dots correctly detected was compared against the actual number of dots on the object recognized by a user.

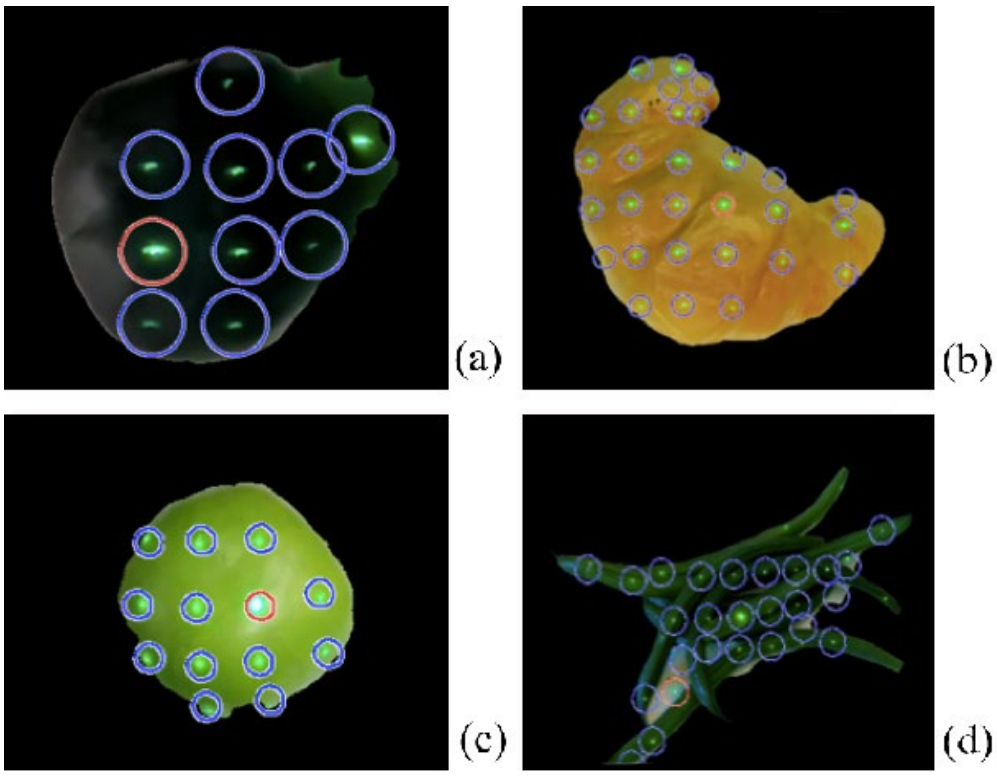

Figure 5.6. Preliminary results of the algorithm on (a) a pear, (b) a croissant, (c) an apple, and (d) green beans.

According to Figure 5.7, peaches have the highest percentage error among all tested objects. This is a result of the color, which enhances the green color of the laser dots. Also, the error percentage for stacked chips and scattered chips are relatively high. One possible reason is that the shape of the chips is very irregular compared to other measured foods. Many of the dots on the edge of the segmented image are not correctly recognized.

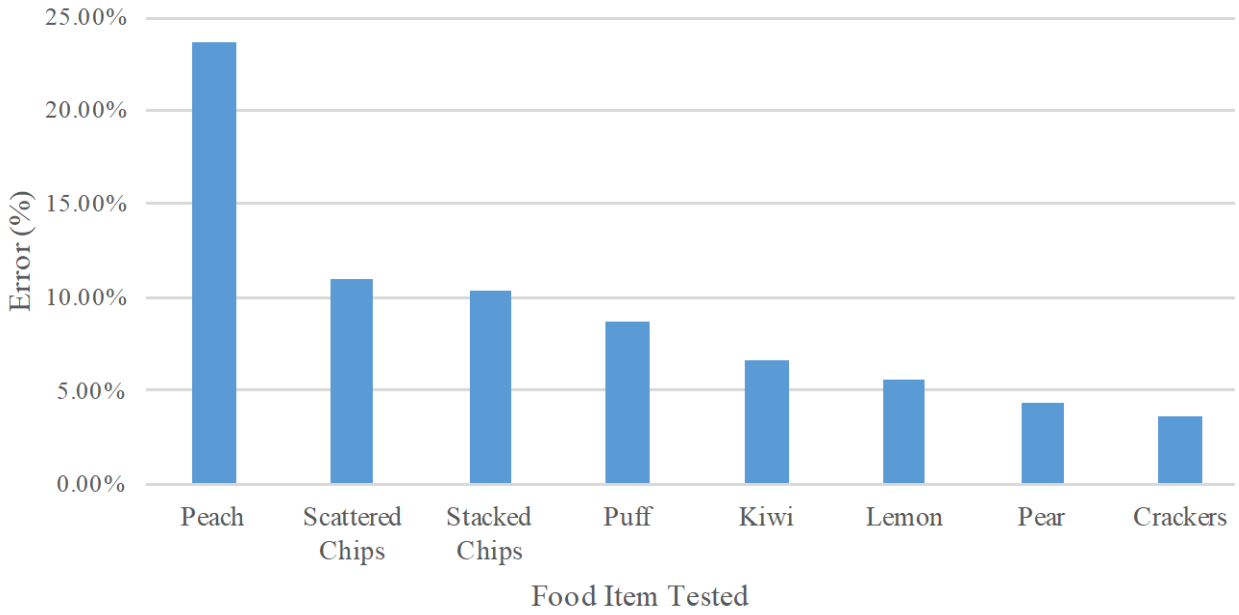

Figure 5.7. Percentage error of the number of dots detected compared to the manual dot detection.

Figure 5.9 shows the average pixel distance of the location computed by the algorithm versus the actual location pinpointed by manual entry, which has a mean of 123 pixels distance over 12 different pictures of food. Figure 5.8 displays the definition of the "distance" plotted in Figure 5.9. Three images were accurate with 0 distance error. In images of 1920x080 resolution, a 123-pixel difference is a difference of 6.4% compared to the length of an image. Reasons for this 6.4% deviation might include that the surface of food scatters different amounts of light, or that the food's color makes it hard to distinguish it from the green laser dot. However, to understand the performance of the AutoDot algorithm, the final results (volumes of multiple food items) while comparing them with the true measured volumes must be examined.

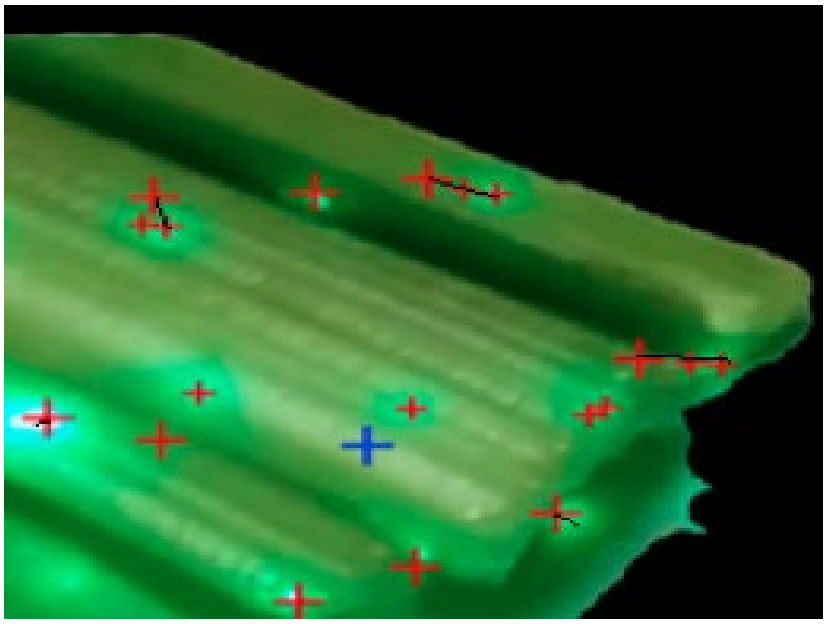

Figure 5.8. A bunch of celery; the black lines portray the deviation of auto-detected laser points.

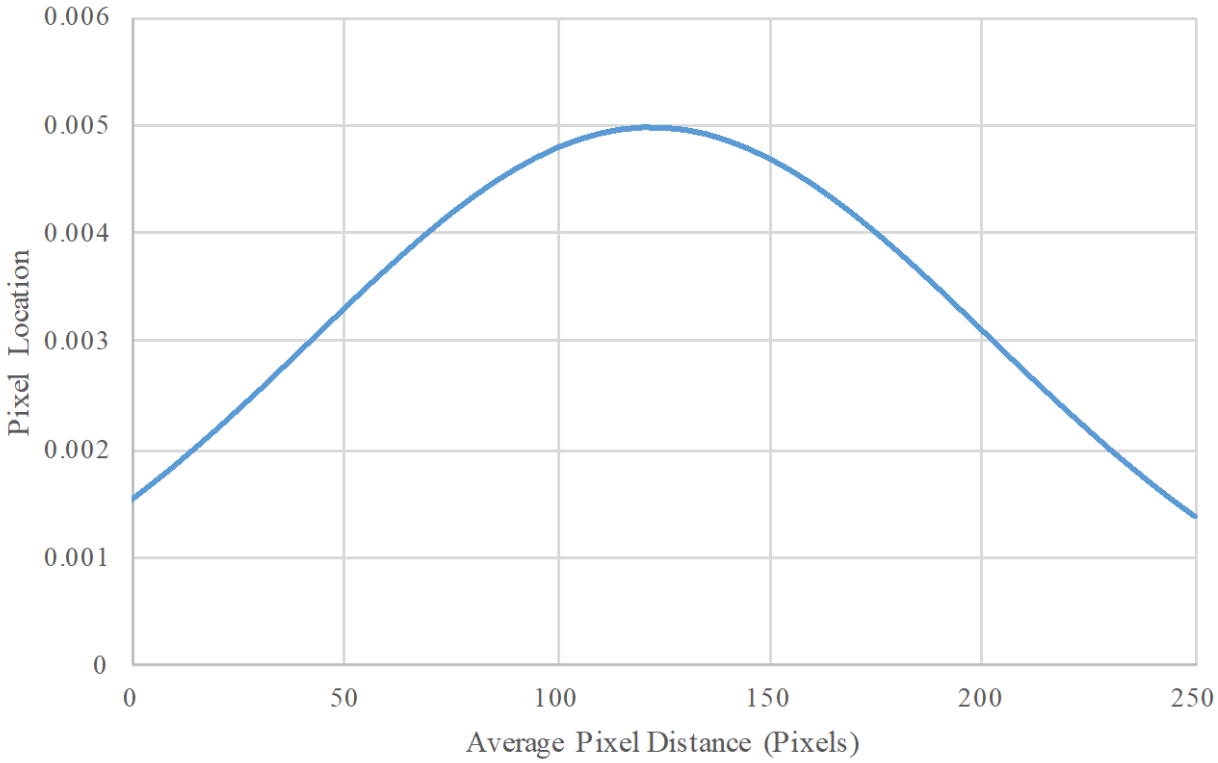

Figure 5.9. A sample of 12 different pictures presents the average pixel distance of the location calculated by the algorithm versus the actual location pinpointed by manual entry.

5.1.3 *Testing of the 3D Reconstruction Algorithm and Volumetric Calculation*

To better test the performance of the device and understand its compatibility in various cases, a more comprehensive study is needed. At this stage, the DDRS device can be used in a research environment. The preliminary results show a promising path for the ease and use of the structured light system in the dietary measurement devices.

Using a laser module in the DDRS device shows it can improve the accuracy of the volume estimation; however, it also introduces a safety hazard for the user. Projecting a 532 nm laser into an unprotected eye could be harmful or cause blindness. The user should take cautionary steps, such as avoiding looking at the laser module directly, avoiding pointing the laser at another person, as well as wearing protective eyeglasses as a precaution.

Figure 5.10 shows the performance of the DDRS algorithm by comparing the calculated volume using 3D reconstruction detection integration and measured volume using water displacement technique for high accuracy. The overall percentage error for the items tested in Figure 5.10 is around 11%; however, these tests were conducted in the lab using engineering students. To test the actual performance of the algorithm, a larger study to evaluate all possible scenarios must be conducted.

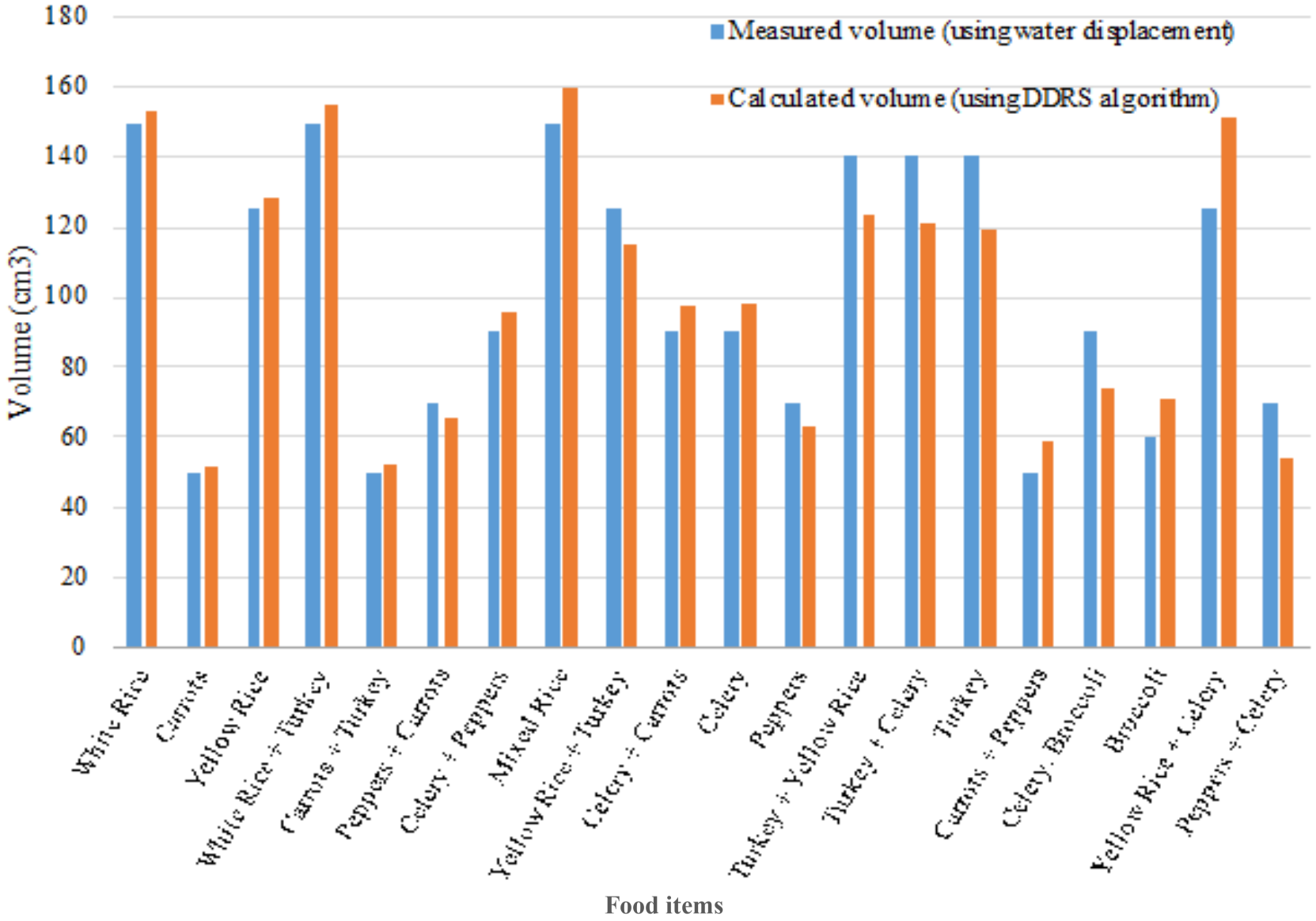

Figure 5.10. Measured volume using DDRS algorithms. Calculated volume using water displacement.

5.2 EXPERIMENTAL DESIGN OF THE DDRS SYSTEM

For testing, the DietSkan system performance was first evaluated separately using known shapes and objects. Once the pre-evaluation was done, system testing took place. Participants were asked to eat pre-prepared meals, and their nutritional intake was measured using the DietSkan system, the 24HR method, and MyFitnessPal.

The DDRS system calculates common nutritional metrics such as calories, carbohydrates, protein, sugar, and fats. Nutritional information was obtained from a collection of sites, as the spread of food items in the experiment were not all found on a single nutritional database. SelfNutritionData [78] and FatSecret [79] are used as both are needed to cover the entire scope of the foods tested. Both methods have nutritional data available in 100 g portions, which allows for easy conversion to per gram data.

5.2.1 Preliminary Testing

Before testing the scanner on a food plate, preliminary testing was conducted with known shapes and easily configurable objects to ensure the scanner was working as defined and identify its limits.

Known geometric shapes: The first stage of the testing involves scanning a known cube and a cone as known volume objects. The cube represented an object with prominent edges, while the cone was used to test the implementation on smooth surfaces. These objects were tested resting on a flat plate and were scanned individually.

Simple geometric shapes such as these rendered well, and the calculated volumes were accurate. For example, for the 7 cm^3 cube shown in Figure 5.11, the calculated volume after post-processing was only 3 cm^3 off.

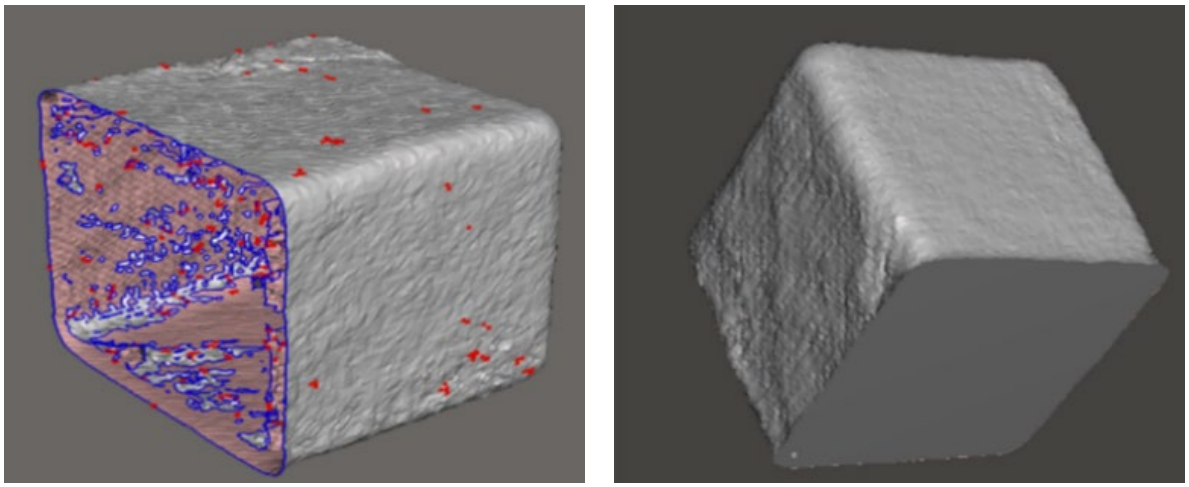

(a) (b)

Figure 5.11. This figure shows the raw 3D mesh of a cube (a) with an unclosed mesh on one side. Once the raw 3D mesh data is passed through the post-processing algorithm, all holes are closed (b), and volume is calculated. The volume error of (a) is 40%, and (b) is under 5%.

Model food items: Similar to the previous test, model food items (apple, pear, and croissant) made of plastic were used to validate the scanner's accuracy. These were scanned individually as well as with multiple models on a plate. Data compiled from twenty-four scans of these models showed a mean percent error of 6%.

The overall results show dependability on the model scanned. For example, the model of an apple had the highest error due to the incorrect estimation of the bottom surface by Meshmixer. Unlike simple geometric shapes, irregular surfaces were harder for the program to predict and resulted in more significant discrepancies. Figure 5.12 shows a 3D scan of an apple and a croissant models (plastic food) in mesh formation after post-processing to close any holes. To further avoid ambiguity and underestimation, the models are placed on a flat surface; however, both items were touching each other. The resulting scan captured the pose in detail, with surface details rendered well. However, during post-processing, the two models had to be split for individual volume estimation. This procedure introduced ambiguity in the region of intersection and required further

processing to be better resolved. The segmentation resulted in the volume of the croissant being estimated to within 5% while the apple was off by 14%.

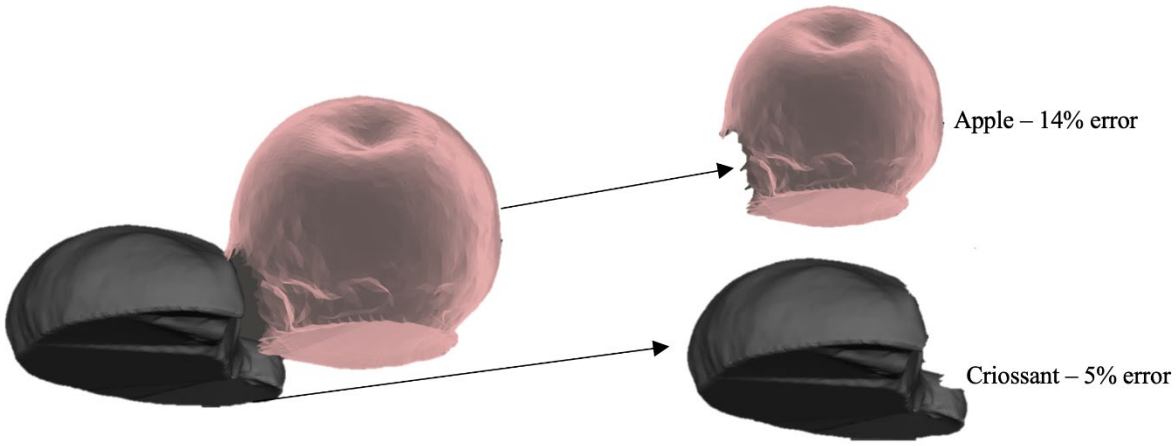

Figure 5.12. Scan with a model croissant and apple in contact with a well-captured surface mesh, as well as the boundary between them.

5.2.2 Comprehensive System Testing

The DietSkan system was utilized in a real-world scenario and simultaneously compared with the 24HR method using the Automated Self-Administered 24-Hour (ASA24) Dietary Assessment Tool and the MyFitnessPal application to test the overall system accuracy, performance, and ease of usability. Twelve randomly selected participants volunteered to consume a prepared plate of food and utilize the three dietary tracking methods to measure their nutritional intake. In all test cases, each plate contained one to three food items, with varying arrangements, including both touching and separated food items (see Figure 5.13.). There were three recipes prepared for the study, which were randomly matched to volunteers (while considering any allergies.) The three plates configurations were (Plate 1) chicken breast and vegetables, (Plate 2) garlic roasted vegetable pasta, and (Plate 3) meatloaf and mashed potatoes. The control measurement was obtained by manually measuring food volume using standard measuring cups. The accuracy of each method was obtained by comparing the control measurement.

(**a**) (**b**)

Figure 5.13. Participants using the DietSkan system during the comprehensive system testing with the prepared food. (a) A participant using DietSkan before eating, of Plate 2 with mixed food items and, (b) A participant scanning leftovers of Plate 3 with food items separate.

The participants were split into three different test groups with varying levels of pre-known information about the meal to identify the robustness of the system to user error and experience. Group A was given the exact recipe for the prepared food, Group B was given a list of recipes to pick one they considered most accurate, and Group C was served a plate with no information. The accuracy of the system was compared across the three groups to identify how well the system worked with user input with discrepancies. The participants then followed seven steps to measure their intake:

- Fill out the initial questions in the 24HR dietary recall survey.
- Fill out the initial questions in the DietSkan survey.
- Scan plate using the DietSkan scanner.
- Eat as much of the meal as they wanted.
- Complete the 24HR and DietSkan Surveys based on leftovers.
- Rescan leftovers with DietSkan scanner.
- Fill out the MyFitnessPal application.

The absolute error was determined as a better metric than percentage error per plate to evaluate the methods due to medication being prescribed as a function of overall nutritional intake, independent of the actual size of the meal. Table 5.1 demonstrates that the DietSkan system pulled ahead of the other two methods, producing a much smaller absolute error with a lower standard deviation, thereby giving a better indication of consumption. The 24HR method performed better than MyFitnessPal, although both had a considerably higher mean error and standard deviation. Calculating the overall percentage error for each method, yielded a 51% error for the 24HR method, a 73% error for MyFitnessPal, and only a 33% error for the DietSkan method. In addition to Table 5.1, the same methods were compared using the group performance, and the results are tabulated in Table 5.2.

Table 5.1. The actual volume for each meal with the associated measured and absolute errors for each method, in grams (g). For each trial, cells highlighted in green are the best result (lowest error) out of the three methods (DietSkan, 24HR, and MyFitnessPal). Cells highlighted in yellow are results that were not the best but still had an error of less than 10 g and, cells highlighted in red were results with errors above 10 g and did not have the lowest error amongst the three methods. These results contain data from all three groups (A, B, and C). Group C users were not made to use MyFitnessPal (taken into the assumption that they are not aware of any information about the plate), and these cells have been labeled NF (Not Found).

Actual Value (g)	**24hr (g)**		**MyFitnessPal (g)**		**DietSkan (g)**	
	Measured	Error	Measured	Error	Measured	Error
19	34	15	78	59	30	11
100	42	-58	52	-48	122	22
30	39	9	NF	NF	80	50
121	46	-75	NF	NF	94	-27
18	59	41	NF	NF	25	7
61	58	-3	156	95	62	1
46	49	3	68	22	39	-7
78	75	-3	56	-22	39	-39
61	44	-17	NF	NF	28	-33
86	24	-62	17	-69	104	18
14	129	115	NF	NF	7	-7
58	26	-32	50	-8	35	-23
84	13	-71	17	-67	94	10
Absolute Error (g)		389		390		255
Absolute Error (%)		51%		73%		33%
Standard Deviation (g)		34		28		14

Table 5.2. A subset of data from Table 5.1 taken to highlight variation in absolute error in grams (g) between each method, depending on the user groups, Group A, B, and C. Group C users were not made to use MyFitnessPal (taken into the assumption that they are not aware of any information about the plate), and these cells have been labeled NF (Not Found). The rows are marked by the plate consumed, and the values are color-coded with lower errors, colored green, and larger errors colored red.

Method	Group A	Group B	Group C	Plate
24HR	15	59	41	1
	3	3	9	2
	71	32	75	3
MyFitnessPal	59	48	NF	1
	95	22	NF	2
	67	8	NF	3
DietSkan	11	22	7	1
	1	7	50	2
	10	23	27	3

For the DietSkan system, average absolute error increased from 7 g to 17 g and 28 g for groups A, B, and C, respectively, and similarly for the 24HR method, error increased from 30 g to 31 g and 42 g. Apart from the lower absolute error, the DietSkan system also performed more uniformly across the three plates. MyFitnessPal was only performed by groups A and B as group C were not told what they were eating, making it difficult to enter information into the application accurately. MyFitnessPal had the highest error amongst group A users with an average error of 74 g but performed well amongst Group B users with a mean error of 26 g and a distribution very similar to the DietSkan system.

5.3 CHAPTER SUMMARY

There is a clear need to move toward automated dietary measurement for enhanced treatment such as cancer and diabetes. The presented system shows a higher performance level in both versions of the system, the DDRS, and the DietSkan. The evaluation of the image processing algorithm proves that it is possible to integrate accurate measurement using 3D imaging without significant disruptions to the user's dietary habit. The use of a straightforward interface, inexpensive equipment, and portable form-factor paves the way for modifying the pipeline, allowing users to participate in the process, relieving the medical staff of some of the load by automating the process.

Chapter 6. 3D RECONSTRUCTION AND VOLUME MEASUREMENT IN POST-OPERATIVE STOMA CARE MANAGEMENT

This chapter discusses the use of 3D reconstruction and volume measurement in post-operative Stoma care management. More specifically, the development of an electronic imaging system for home use for better preparation, application, and cutting of the wafer, as well as for remote monitoring of the stoma via images of the stoma and peristomal area for further analysis. The introduction of the Individualized Wafer Fitting System (WFS) into a home or hospital use can improve the quality of life, mobility, independence, mood, self-confidence, and the overall health of an ostomate. The WFS is a 3D scanning tool, which can generate optimal shapes, reducing incidents of bleeding and skin irritation, lowering the frequency of ostomy wafer and pouch changes, and improving an ostomate's daily confidence.

6.1 ABOUT STOMA

A stoma appliance is a connection to the body bag for the collection of intestinal output via an aperture in the patient's abdominal wall. The bag is attached to the skin using a wafer; many stomas have irregular shapes, making manual wafer fitting very difficult. Better post-operative wafer fitting has been identified as a critical step for stoma care improvement [9]. The ostomate (or the caregiver) is required to measure the diameter of the stoma accurately before fitting the appliance. A cutting error of as little as 2 mm can result in serious complications, including damaged blood vessels or profuse, recurrent bleeding [patient interview].

6.2 MOTIVATION

There are two million people worldwide with stomas [80]; the ostomate population is projected to increase yearly. Stomas are small openings in abdomens usually created after intestinal surgeries to divert digested food out of the body. Stoma appliances are used to collect, contain, and manage the output of the stoma in a safe and, ideally, odorless way. The stoma management process, also known as stoma care, is complicated and requires careful attention and precision. The stress and difficulty of managing a stoma are compounded by the old age of the ostomate population, who are, on average more than 60 years old. Proper stoma management is a critical aspect of an ostomate's health-related quality of life (HRQOL). Inadequate stoma management leads to skin irritation, bag leakage, limited mobility, diminished self-confidence, increased rates of depression, feelings of inadequacy for intimacy, pain, and a host of other physical and psychological complications (patient interview.)

A barrier or wafer protects the skin around the stoma, known as the peristomal skin, from direct contact with the stoma pouch or appliance. An adhesive is used to apply the wafer to this sensitive skin. Although there are standard, circular, and oval cut shapes for wafers, these wafers are not suited for irregularly shaped stomas. The diameter of the irregularly shaped stoma must be known so that the ostomate or the ostomate's caregiver can hand cut the wafer for proper fit. Throughout the year, the diameter of the stoma changes by a few millimeters due to visceral fat, healing, or abrasions, yet cutting errors of as little as 2 mm can result in serious complications, including damaged blood vessels or profuse, recurrent bleeding. Due to the low mobility and limited eyesight of some ostomates, properly fitting a stoma wafer is very difficult.

6.3 Background of 3D Measurement in Stoma Care Management

The traditional methods for assessing stoma characteristics are visual cues (e.g., color, shape, size) and physical measurement techniques (e.g., stoma measuring cards) [81]. These methods can be heavily subjective and lead to the irritating contact of bodily fluids with the peristomal skin. Because most of the indications of diminishing skin integrity are subtle, many patients miss the early warning signs (e.g., prolapse), potentially resulting in expensive corrective surgeries. It is often necessary for a nurse or specialized care provider to be closely involved in the care regimen to monitor the conditions of the stoma, as well as to administer treatments to minimize severe stoma-related health complications [82]. Ostomates with low mobility or vision are especially vulnerable to these complications and may have considerable difficulty accomplishing tasks associated with self-care [83].

Current stoma therapy appliances and techniques are typically invasive [82, 84], extensive [85, 86], and high-maintenance [81, 83, 87]. Proper stoma care requires consistent and vigilant attention to a number of detailed characteristics of the stoma, including size, shape, color, and protrusion [81]. Skin integrity is at risk when proper maintenance does not occur, often leading to patient discomfort [87].

Post-operative wafer fitting is typically conducted by trial and error. Due to changes in patient weight, size of the stoma, and the shape or condition of the peristomal area, regular measurement is required. Patients with cognitive, visual, or dexterity issues have persistent difficulty in preparing and fitting these wafers. The current industry standard circular-wafer with a hand-cut opening is unsuitable for a sizeable number of ostomates worldwide. Improper wafer fit can result in damaged blood vessels and profuse recurrent bleeding. Peristomal bleeding is hard to detect because the blood is not easily visible; it does not stain clothes, as it happens with other bleeding

events. Instead, blood accumulates in the ostomy pouch and is usually not discovered until much later, when the pouch starts to become full. This condition can result in up to half a liter of blood loss from a single incident. This blood loss is especially dangerous for post-chemotherapy cancer patients, who can be simultaneously anemic and neutropenic, often taking blood thinners to prevent post-surgery blood clotting.

There are several commercial methods to address these complications; however, no existing market solution includes automatic measurements for the patient to minimize manual trial and error measurements. Nu-Hope Laboratories, Inc., offers ostomates either precut or ready-to-cut wafers in two shapes (oval or circular). However, these wafers do not address the issues of precise shapes and are not always suitable for irregularly shaped stomas. ConvaTec Technologies and Hollister offer moldable adhesive wafers, but for these to work successfully, patients must press hard on the seal to make the mold fit. For some ostomates, this pressure is too uncomfortable or painful to be part of a life-long stoma care regimen. The wafer is also not a "floating flange," so ostomates cannot get their fingers behind the wafer to snap close the bag. Although these are good first steps, both types of wafers can cause pain around the stoma area; there have also been reports of stomach fluid dissolving the moldable wafer's material, leaving behind hard-to-clean residue.

6.4 Design and Development of the Image Processing Algorithm

6.4.1 Equipment Selection

The Individualized Wafer Fitting System (WFS) uses a novel visual measurement approach for the automated and accurate cutting of wafers around a stoma. Specifically, WFS improves the precision of wafer fit and the overall ease of stoma management. The system includes two elements: a 3D scanner and a camera display. The 3D scanner builds on our team's recently

developed portable laser scanner (Figure 6.1) for the measurement of 3D objects for nutritional studies [88-90].

Three-dimensional imaging is the cornerstone of a broad range of diagnostic (e.g., CAT scans) and post-operative care (e.g., fitting of prosthetic and orthotic appliances). However, so far, 3D imaging is predominantly used in clinical environments, not at home. The difficulty is that some, or all, of stoma care activities, must take place outside of the clinic, conducted either by patients or by caretakers in elderly care facilities. The use of a mobile phone enhanced by the 3D scanner allows for electronic imaging for better preparation, application, and monitoring of stoma wafers, as well as for creating images of the stoma and peristomal area for further analysis. Design decisions are made to minimize the incidents of bleeding and skin irritation, as well as for lowering the frequency of ostomy wafer and pouch changes.

6.4.2 3D Reconstruction

The WFS laser measurement unit is associated with a mobile phone platform that records and automatically transmits 3D image information to a database. The 3D model of the stoma provides patients, clinicians, and researchers with detailed information that is otherwise difficult to obtain; it is impossible to take a single photo of a protruding stoma and capture all needed areas of the stoma-to-skin interface (see Figure 6.2). Stereoscopic imaging is not used, as it produces an average error of 10% in size estimation due to difficulty in collocating pixels across two separate images and optical distortion at close distances.

By using a structured light scanning (photo and laser combined) approach, WFS constructs 3D surfaces based on positions of the laser grid dots. The WFS software is developed using MATLAB and Open Source Computer Vision (OpenCV) in Visual Studio [91]. The smartphone application provides a proper wafer shape in 95% of scans. Reference scans are taken from

commercially produced, three-dimensional stoma models that are currently in use for research and educational purposes. To determine the accuracy of the WFS software algorithms, we have gathered precise measurements of commercial plastic stomas and compared the corresponding scanned apertures to generate the percentages of error. Before optimization, this approach has produced an error of 5%. The ground truth measurements are conducted on plastic models of stomas with calipers of 1 μm resolution. This level of error is expected to be reducible after optimizations.

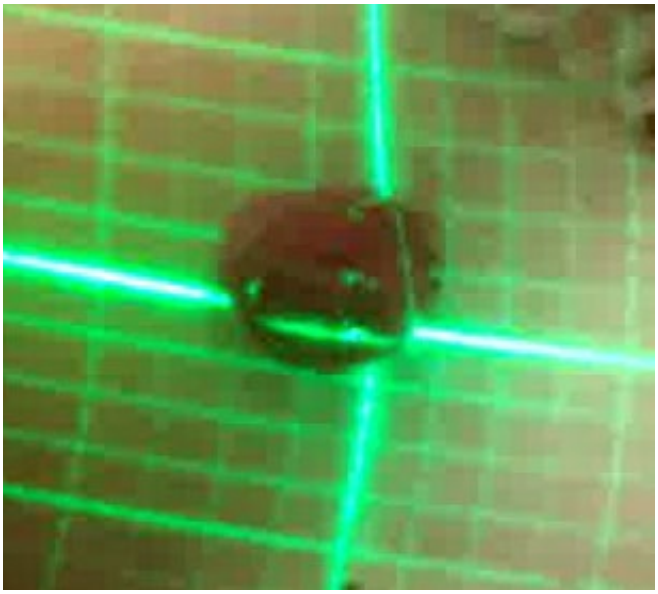

Figure 6.1. The laser grids projected onto the skin and stoma surface. The diffiraction lens is changed to a square model to increase visibility.

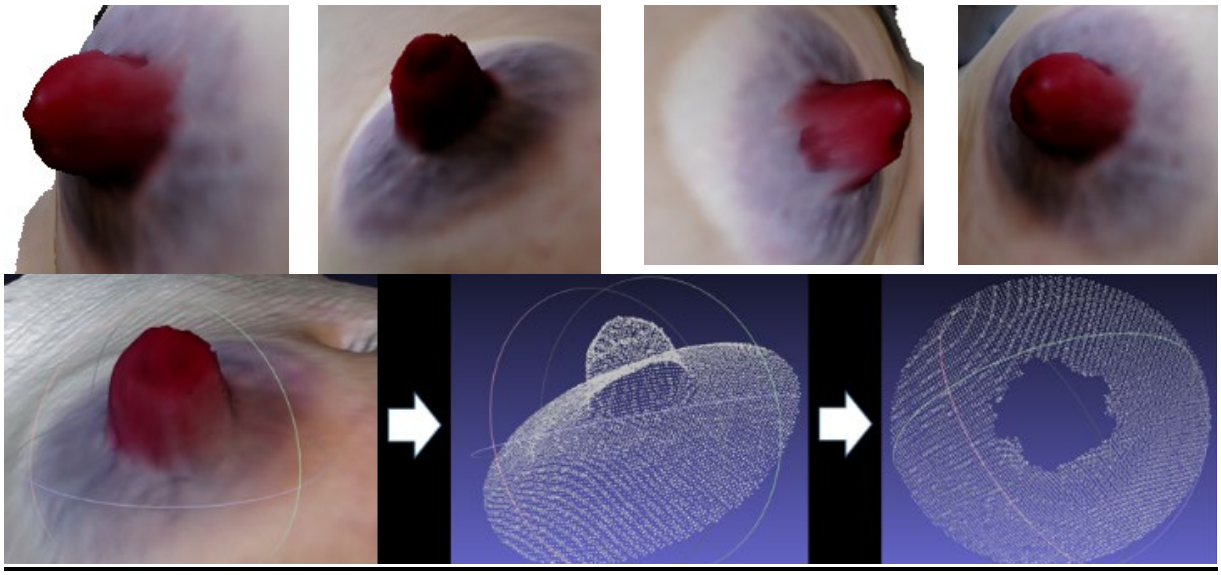

Figure 6.2. Several digital visualizations of a real stoma. Note that these representations are not photographs; they are actual 3D reconstructions overlaid with video data.

The WFS uses the following approach for accurate wafer cutting: the computer processes the 3D model of the stoma, an "ideal" aperture contour is generated, and the contour is used for precise wafer cuts (Figure 6.3). Having a 3D profile of the peristomal skin is useful for many clinical applications (e.g., for cutting wafers, selecting filler ring shapes, for monitoring skin healing). In future iterations of the device, generated 3D profiles may be used to enhance early detection of costly and dangerous stoma complications, which would minimize ostomy-related surgeries and therapy.

The acquired video sequence with projected laser grid patterns gives enough information to estimate the shape of the stoma and peristomal skin. Laser grid intersections can be detected in the video frames, and the depth maps can be generated from different viewing angles. A 3D model of the stoma can be reconstructed by fusing the depth maps. The output can be used to estimate the curvature of the skin, and, initially, a reference circle can be used for extracting the boundary information between the stoma and skin. In the 3D models, the circle appears to be round but is

elliptical in a lateral view. By combining the back-projection of an ellipse and the curvature from the laser grids, we obtain the exact boundary between the stoma and skin. A single image shows only part of the boundary; the rest is blocked from view. The splicing of video frames allows for the visualization of the entire boundary. The last step of 3D reconstruction is to calculate the real-world x and y values of the point cloud. The x and y values are chosen by the algorithm on the edge of stoma, the pixel locations of 2D points in the image, see (24) and (25). To detect the edge surrounding the stoma, we use two preset values of x and y to map the edge:

$$x_{ra} = (x_{cu} - \frac{x_{di}}{2}) / (\frac{x_{di}}{2}), \; x_{es} = tan\left(\frac{\theta}{2}\right) \cdot (z_{es}) \cdot (x_{ra}) + C_{xs} \tag{24}$$

$$y_{ra} = (y_{cu} - \frac{y_{di}}{2}) / (\frac{y_{di}}{2}), \; y_{es} = \frac{2}{3} tan\left(\frac{\theta}{2}\right) \cdot (z_{es}) \cdot (y_{ra}) + C_{ys} \tag{25}$$

where x_{cu} and y_{cu} are the x and y pixel values, x_{di} and y_{di} are the x and y (horizontal) dimension of the picture, θ is an angle of projection, which comes from the device, and C_{xs} and C_{ys} are the distances between the stoma and the device.

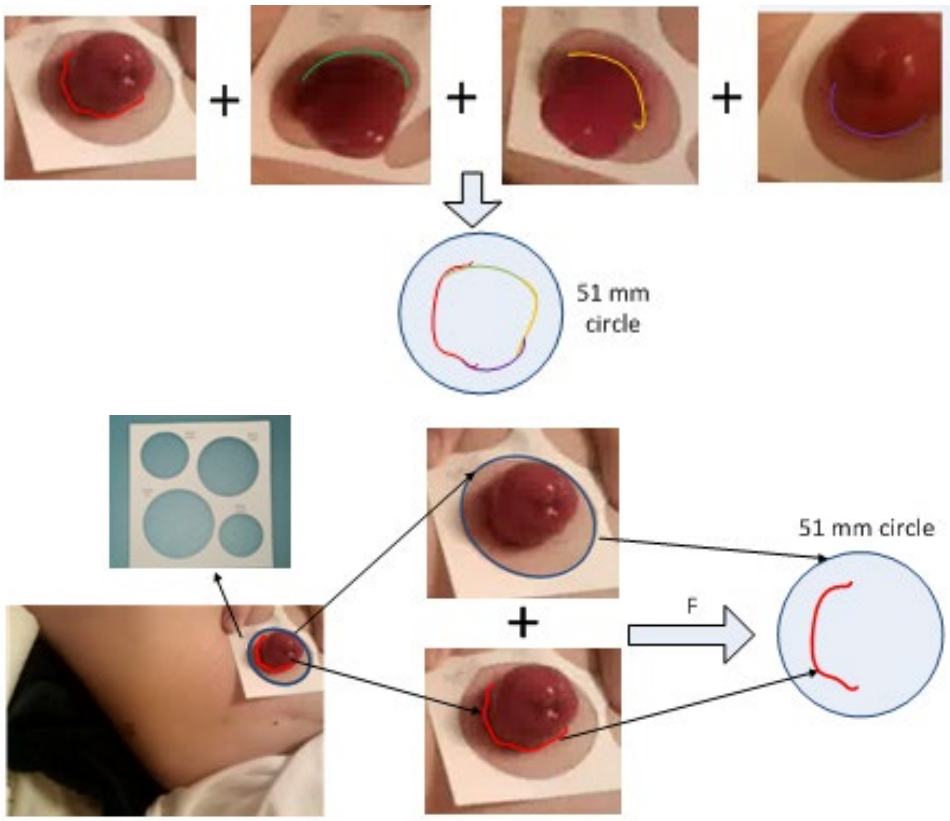

Figure 6.3. The mapping between the ellipse image, real reference, and reference image (51 mm) to find the transfer function, and, ultimately, plot the ideally-fitting aperture perimeter.

6.4.3 The Software Application

The WFS laser measurement unit is associated with a mobile phone platform that records and automatically transmits 3D image information to a database. There are strict measures to ensure the privacy and safety of all patients' information; these measures abide by HIPAA and health regulations, as well as standard patient protections and cybersecurity protocols. Since many patients with stomas are older and may struggle with technology, a user-friendly interface consisting of prominent, intuitive buttons (e.g., scan, tutorial, purchase, support) is emphasized. The font of a larger size and each button has a distinct color. Thus, the application is designed with

navigation easiness as the primary concern (see Figure 6.4 for a prototype). In the future, built-in tutorials can be featured to provide ostomates with the necessary information to use the application.

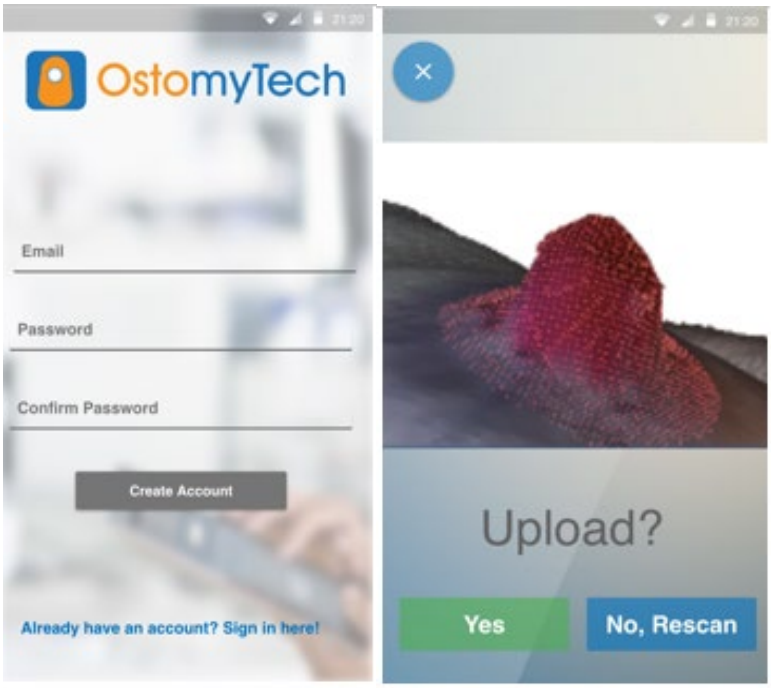

Figure 6.4. Prototype demonstration of the mobile application. Application buttons are large and color-coded for vision impaired and elderly users.

6.5 Evaluation of 3D Measurement in Stoma Care Management

Plastic stoma models of six different shapes were used to evaluate the system. Tests were conducted with four different stoma models in different lighting settings. The results were compared to manually measured data, which used tracings to divide the circumference into 36 10-degree slices. This allowed for the evaluation of both the overall average error and maximum error. The system satisfied both average error and maximum error requirements. If the average error is within an acceptable range (5%), but the maximum error is too high, then at that specific point on the tracing, tissue damage is almost inevitable. Figure 6.5 shows the maximum error, $Max\_Circ(\theta_1, \theta_2, \ldots, \theta_{36})$, as well as the average error, $\overline{\theta_n}$, on a traced layout of a stoma.

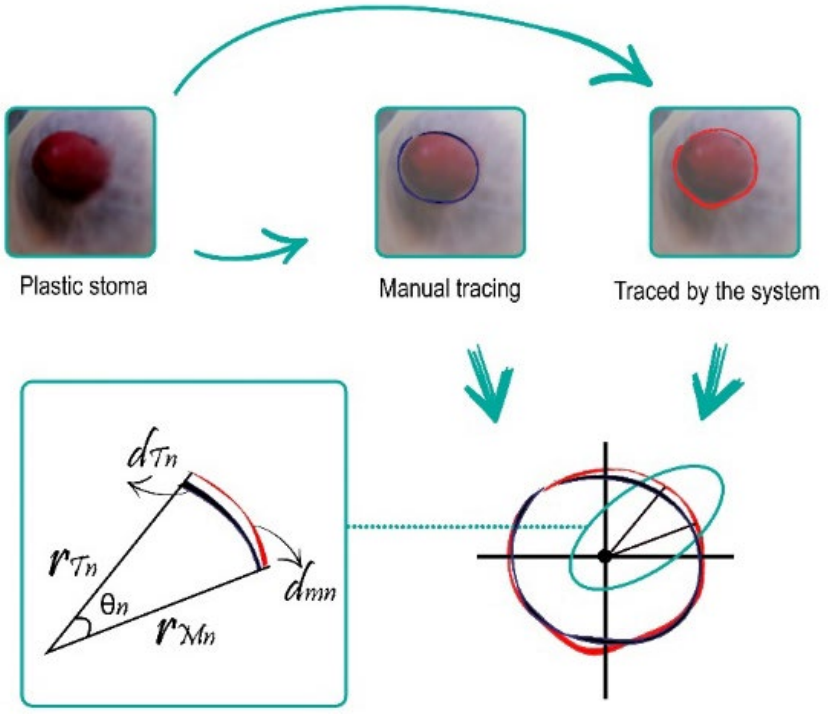

Figure 6.5. Evaluation process using small intervals theta to measure the difference between the control and measured perimeter

Figure 6.5 shows the error analysis and system evaluation process. If θ_n is the selected angle of 10 degrees for both the manually measured and calculated by the system

$$\theta_n = \frac{2\pi}{n}, \qquad n = 36 \tag{26}$$

The circumference of θ_n can be calculated via:

$$d_n = \theta_n \times r_n \tag{27}$$

Once the circumference has been calculated and measured, the error is calculated.

$$Error_n = \left|\frac{(d_{Mn} - d_{Tn}}{d_{Mn}}\right| \times 100 \tag{28}$$

$$Error_{Max} = \max(Error_1, Error_2, \dots, Error_{36}) \tag{29}$$

$$Error_{Avg} = average(Error_1, Error_2, \dots, Error_{36}) \tag{30}$$

where θ_n is the selected iterative angle for measuring the circumference in the smaller iterations, n is the number of iterations, which is set to 36 for the testing process, d_n is the selected circumference, which is measured by using θ_n, d_{Mn} is the manually measured circumference as a true measurement, $d_{Tn}$is the traced circumference measured by the system, $Error_{Mn}$ is the maximum error among the 36 circumference slices, and $Error_{avg}$ is the average error of the entire circumference.

Preliminary estimations demonstrate that the described approach can provide accuracy of about 5% error, which is consistent with the requirement mentioned previously. The system has also shown great potential in the visualization of the stoma for the physician to see irregularities and address bleeding.

The initial testing was conducted with four different stoma models with different sizes and shapes; the results were looked in two separate categories: 1- the time spent (T), 2- error compared to the manual measurements. Figure 6.6 shows the analysis of the average time spent to complete the measurement of stoma perimeter manually versus a 3D scan. The results show a decrease in the average time spent by 1.8 minutes. Figure 6.7 illustrates the analysis of the measurement accuracy. Each stoma is measured manually (MM1 and MM2) by two different researchers (one trained and one untrained) and then compared to the 3D scan measurement (3D1 and 3D2). The results show a 5% error rate compared to the average measurement difference.

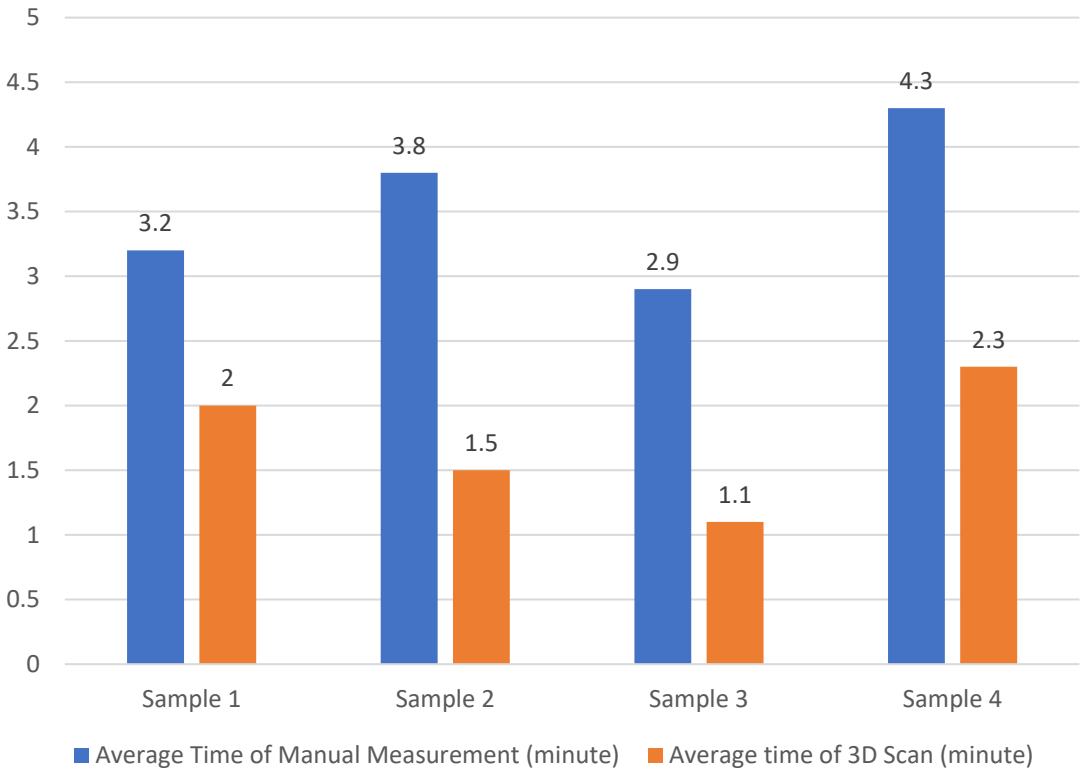

Figure 6.6. The average time of manual measurement vs. 3D scan in minutes.

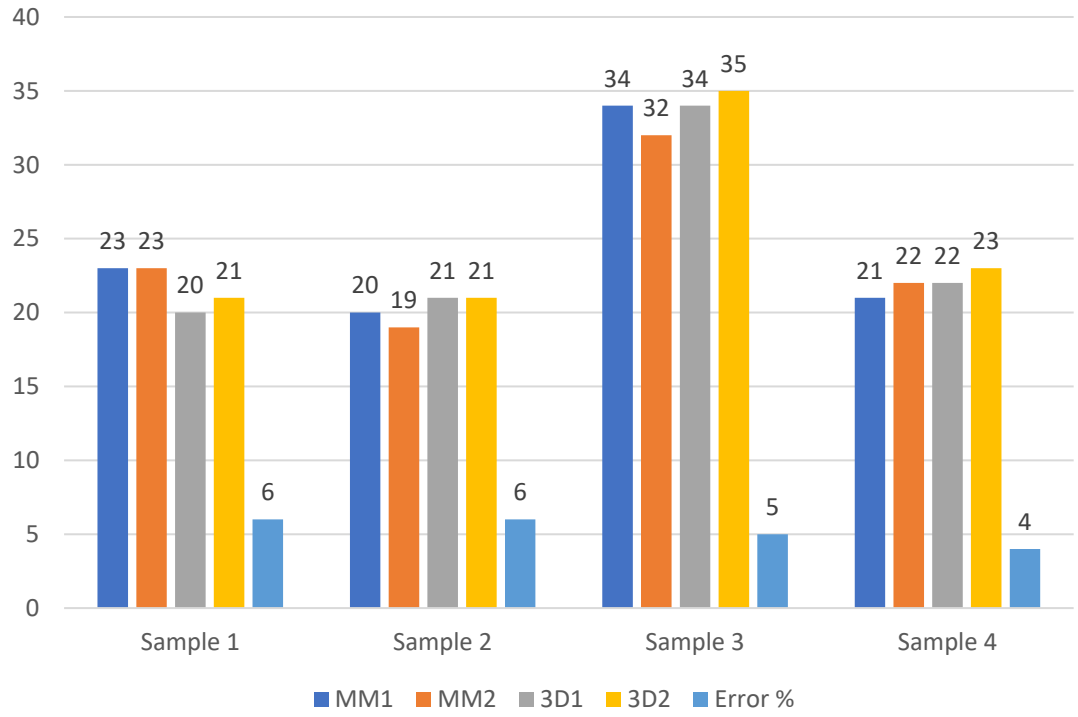

Figure 6.7. Average perimeter measurement of manual measurement (MM) vs. 3D scan (3D).

6.6 CHAPTER SUMMARY

Effective stoma care solutions emphasize self-care, which allows patients to reclaim their independence and rebuild their psychological well-being and self-image. An imaging-enabled system reduces the burden of self-care for ostomates, which is heavily encouraged by doctors and nurses after the initial period of hands-on care while reducing pain and bleeding episodes. This chapter discusses the development and testing of the Wafer Fitting System (WFS), which uses a novel visual measurement approach for the automated and accurate cutting of wafers around a stoma.

Chapter 7. SENSOR NETWORK AND LOCATION-BASED AUTOMATION IN AIR QUALITY MONITORING

Recently, the development of the dietary measurement techniques presented in this dissertation has been expanded to empower large-scale epidemiologic studies. Specifically, the location-based automation and cloud computing features presented in this thesis have been used to develop a wearable air quality monitoring system. Personal air quality monitoring requires compact, real-time, and low-cost instruments without the sacrifice of accuracy and reliability [92]. This chapter presents AeroSpec, a distributed air quality monitoring system, comprising of a network of mobile optical particle counter sensors, centralized stations for enhanced pollutant analysis, and software that allows real-time monitoring and mapping of both indoor and outdoor environments. The system was tested side-by-side with industry-standard devices and then laboratory rated. The results demonstrate that AeroSpec's data show an accuracy of 95% when compared to the certified industry-used systems.

7.1 MOTIVATION AND BACKGROUND

Exposure to particulate matter (PM) is associated with adverse health effects like asthma, cardiopulmonary diseases, and lung cancer, which are responsible for the premature deaths of about seven million people worldwide in 2014 [93]. Unhealthy air is especially hazardous to children and sensitive populations [94].

Low-cost, wearable PM exposure systems are used to study the health risks associated with poor air quality [95]. Currently, there are a variety of methods used to measure PM concentrations; however, these methods are expensive and only focus on larger particle sizes. In addition, the

detection of fine particles is expensive and time-consuming, which makes personal monitoring impractical at a larger scale.

7.2 THE AEROSPEC SYSTEM

The AeroSpec system consists of a PM optical particle counter (OPC) sensor, a communication module, a smartphone (which includes a GPS sensor, wireless connection via a cellular, and a Wi-Fi chip), a database server to store and process the data on the cloud, and the main particle-sizer and particle concentration analysis algorithm (which runs on the cloud servers). Figure 7.1 shows the overall system, the device in use, and the components inside. The AeroSpec system utilizes the OPC sensor, a suction fan, and a photodiode. Other sensors [96], [97], archival $PM_{2.5}$, ammonia concentration, and bioaerosol collectors are being incorporated into this modular platform [98, 99].

A customized smartphone app allows the AeroSpec hardware to upload the captured data to the cloud and to calculate the particle sizing, particle counting, and particle concentration for $PM_{0.3}$, $PM_{0.5}$, $PM_{0.7}$, $PM_{1.0}$, $PM_{2.5}$, and $PM_{10.0}$.

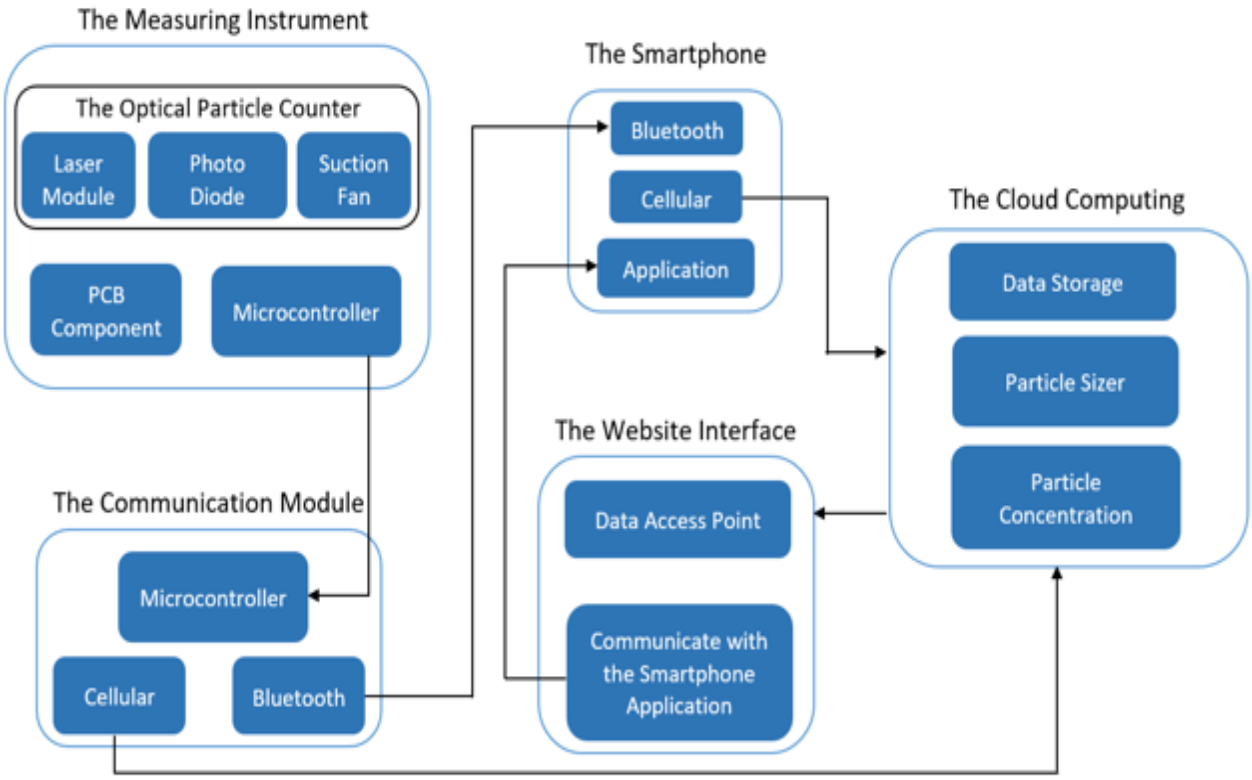

Figure 7.1. The AeroSpec networking system diagram.

7.2.1 The Functional Design

The system value of this project is for large populations affected by poor air quality, overall health, and productivity. The approach can be used in other applications, including monitoring industrial emissions and building health and security applications. The technology can be used in support of several NIH and WHO initiatives, such as Environmental Epigenetics, Global Environmental Health, Environmental Influences on Child Health Outcomes (ECHO), Exposure Biology, and the National Nanotechnology Initiative. There is also a need to evaluate the effect of PM exposure on cancer and neurological diseases. Obtaining PM concentration of the indoor air quality via personal exposure is a crucial step in analyzing the effects of spending long periods of time in and indoor environment.

Particulate Matter (PM) measurement: The OPC sensor measures the concentration of particles and organizes it using a present protocol. For the AeroSpec system, the Plantower PM sensor was selected due to its portability and low-cost. The Plantower sensor has ten pins, but for the purpose of this study, only use five pins were selected. The first two pins are for the +5V power, two are for the ground, and two are for transmitting and receiving (TX, RX). The transmit pin is connected directly to the ATmega328P's serial RX port, and both power and ground pins are connected to the +5V and GND of the ATmega328P, respectively. The ATmega328P provides power for the entire system and can be powered by Universal Serial Bus (USB) or the external power supply.

Data received from the Plantower sensor will be directly transmitted over the Bluetooth serial connection with additional information appended at the end of the message. Table 7.1 shows the communication protocol for the Plantower sensor. The start of the message can be determined by looking for the fixed sequence of four bytes, which are 0x42, 0x4d, 0x00, and 0x1C. The information transmitted over Bluetooth is defined in the following table. The table is copied from the Plantower sensor datasheet with exception to the extra data appended to the end of the message.

Table 7.1. Communication protocol from the Plantower Sensor.

Data	**Description**
Data 1	PM_1 concentration ($\mu g/m^3$)
Data 2	$PM_{2.5}$ concentration ($\mu g/m^3$)
Data 3	PM_{10} concentration ($\mu g/m^3$)
Data 4	PM_1 concentration under atmospheric environment
Data 5	$PM_{2.5}$ concentration under atmospheric environment
Data 6	PM_{10} concentration under atmospheric environment
Data 7	Number of particles with a diameter beyond 0.3 µm in 0.1 L of air
Data 8	Number of particles with a diameter beyond 0.5 µm in 0.1 L of air
Data 9	Number of particles with a diameter beyond 1.0 µm in 0.1 L of air
Data 10	Number of particles with a diameter beyond 2.5 µm in 0.1 L of air
Data 11	Number of particles with a diameter beyond 5.0 µm in 0.1 L of air
Data 12	Number of particles with a diameter beyond 10 µm in 0.1 L of air

Printed circuit board (PCB) and electronics: The AeroSpec PCB design shown in Figure 7.2 has both DC power jack and USB port so that the device can be powered through both ports. Also, because the OPC has a USB port, the user can re-program code on the ATmega328P microcontroller if the user wants to extend the functionality of OPC or implement a different data analysis strategy. Figure 7.3 and Figure 7.4 demonstrate the first prototype of the AeroSpec hardware.

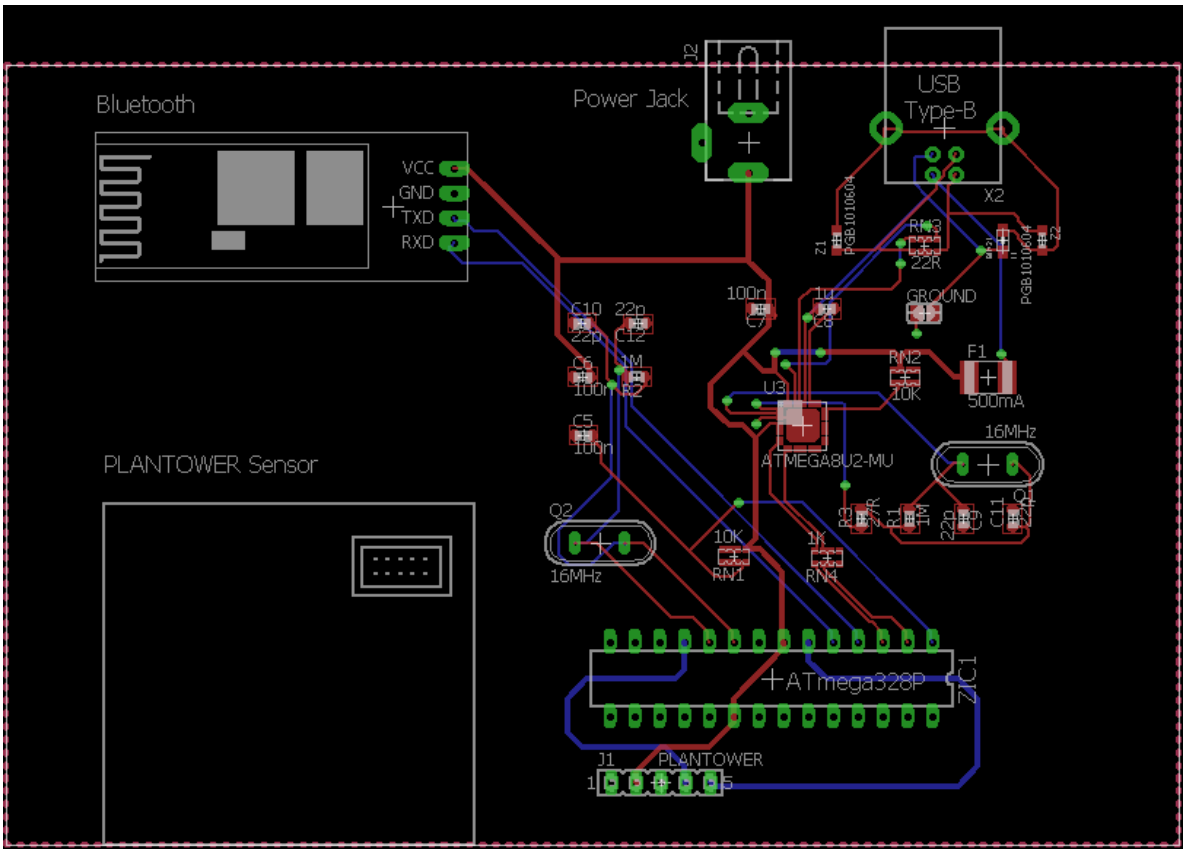

Figure 7.2. PCB layout of the sensor board is demonstrating the design of the electronic components.

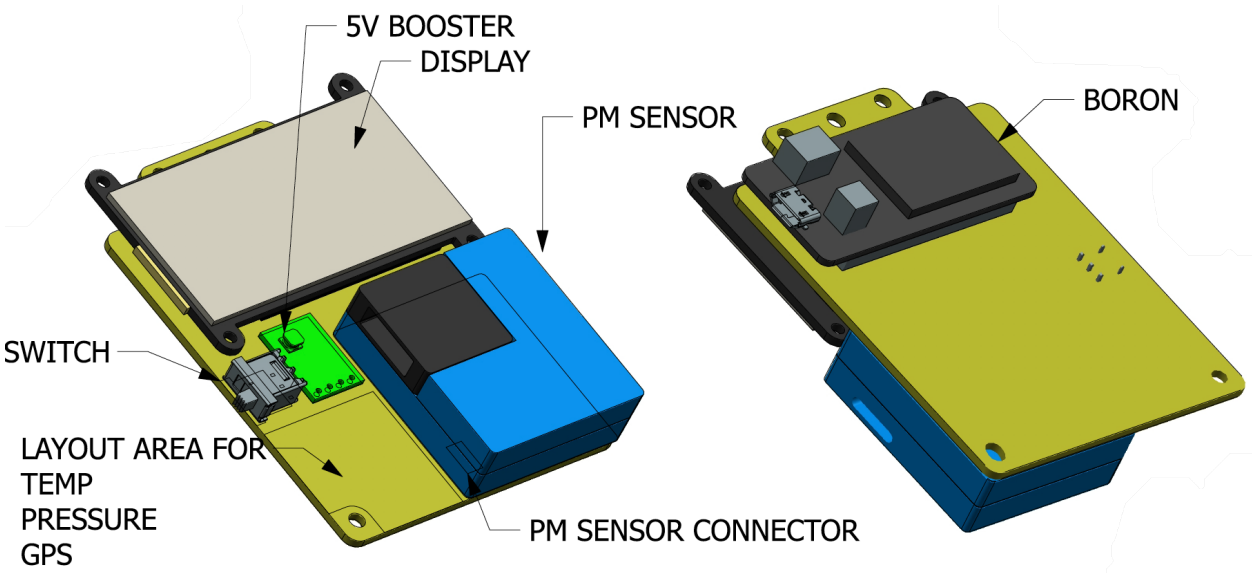

Figure 7.3. The 3D modeling of the hardware component with the main electronics is highlighted.

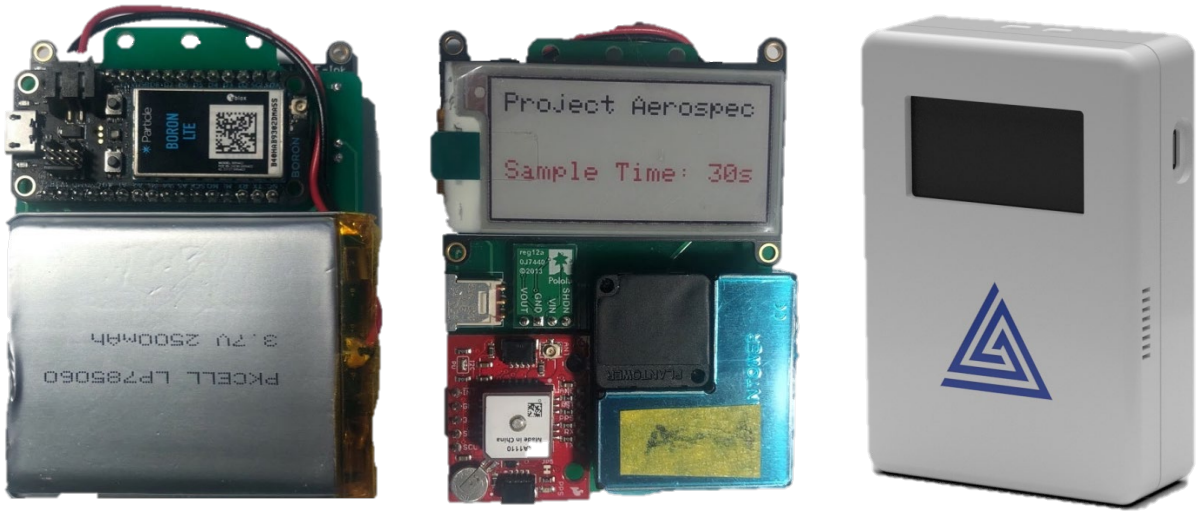

Figure 7.4. The first AeroSpec device fully assembled. From the left, backside of the board, front-side of the board with the LCD, and the 3D printed enclosure of the device.

Calibration: Hardware calibration is a requirement to create a training model for the PM sensor. The calibration requires access to temperature and humidity data. Task-based and personal 8-hr time-weighted average (TWA) was used to calculate the R-value shown in (31).

$$8hr\ TWA = \frac{T_1 C_1 + T_2 C_2 + \cdots + T_n C_n}{8hr} \tag{31}$$

where T is time, C is concentration, and TAW is time-weighted average.

There are different concentration breakpoints to calculate AQI for different particles like $PM_{1.0}$, $PM_{2.5}$, PM_{10}, etc. The concentrations of these particles are converted to AQI value. The concentration breakpoints for different particles are shown in Figure 7.5

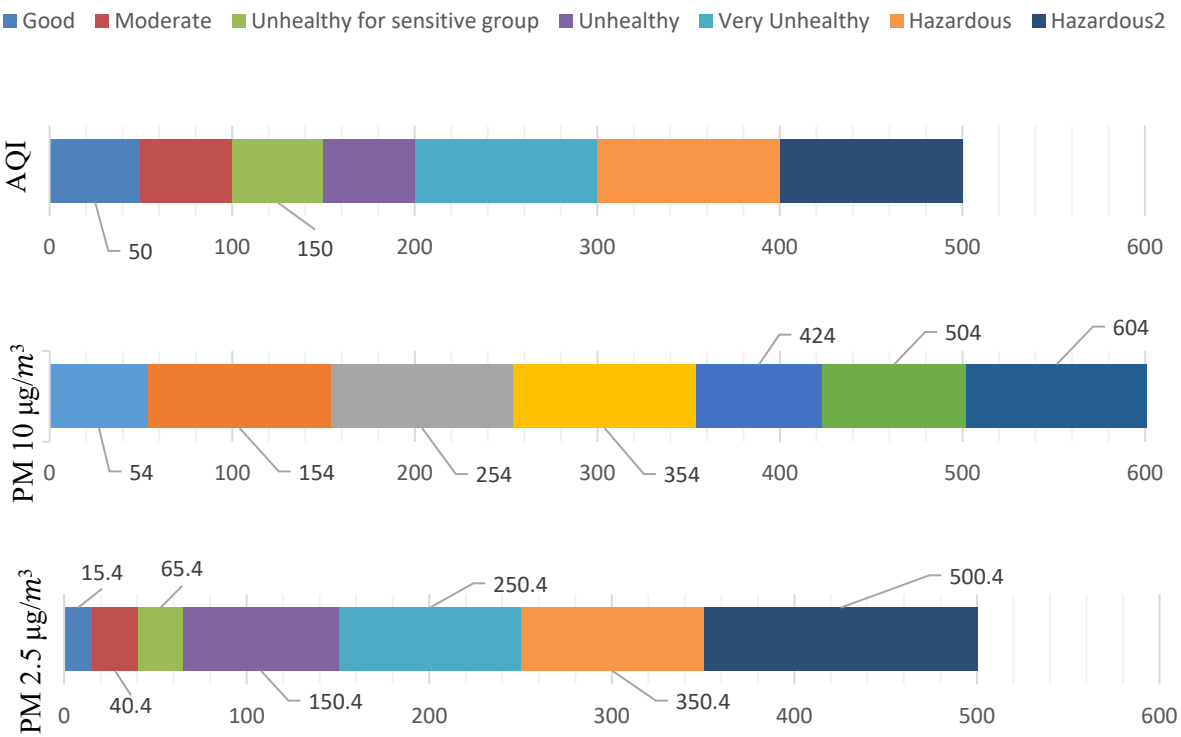

Figure 7.5. AQI ranges based on the concentration of different types of particles.

Database Design: One of the main sections of the AeroSpec system framework is the database structure and networking. The focus is directed toward the creation of a live air-quality map for the facility using personal exposure devices. This step requires a secure one-to-one communication protocol for individual sensors and server compatibility with the facility's data structure. Figure 7.6 shows the architectural design used to develop the AeroSpec system. The structure is used to deploy our algorithm and data structure and connect to the facility database for

a seamless transition. Using Amazon Web Services (AWS) ensures the protection of the data, as well as the necessary bandwidth to transfer data within the specifications.

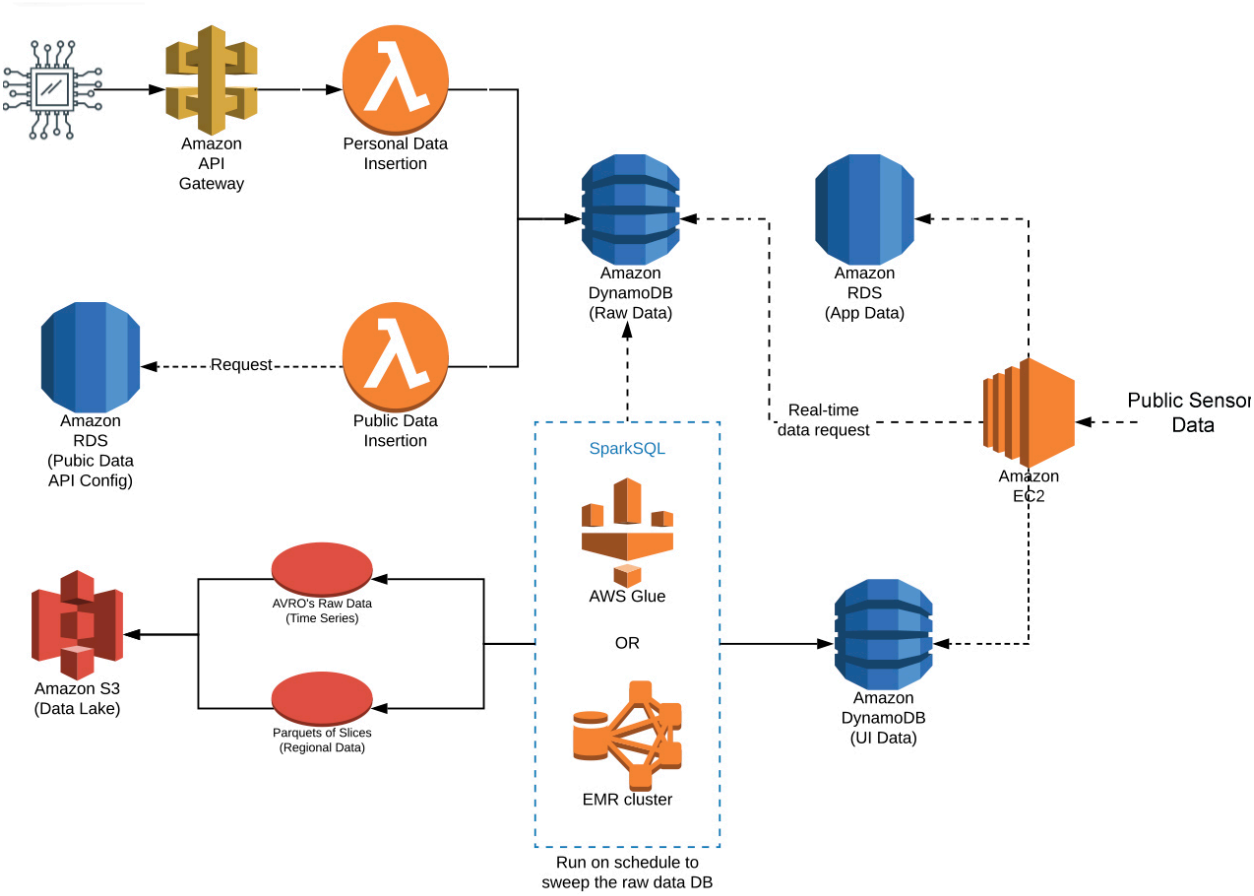

Figure 7.6. The AWS IoT architectural design of the AeroSpec cloud computing machine.

Smartphone application: the smartphone application used for this system is called AeroSpec, which has been developed specifically for this system to read the data from the system. AeroSpec reads the data from Bluetooth and can plot the AQI values and the particle concentration values. Figure 7.7 shows the graphs for both PM concentration (color-coded based on AQI standards) and PM sizing.

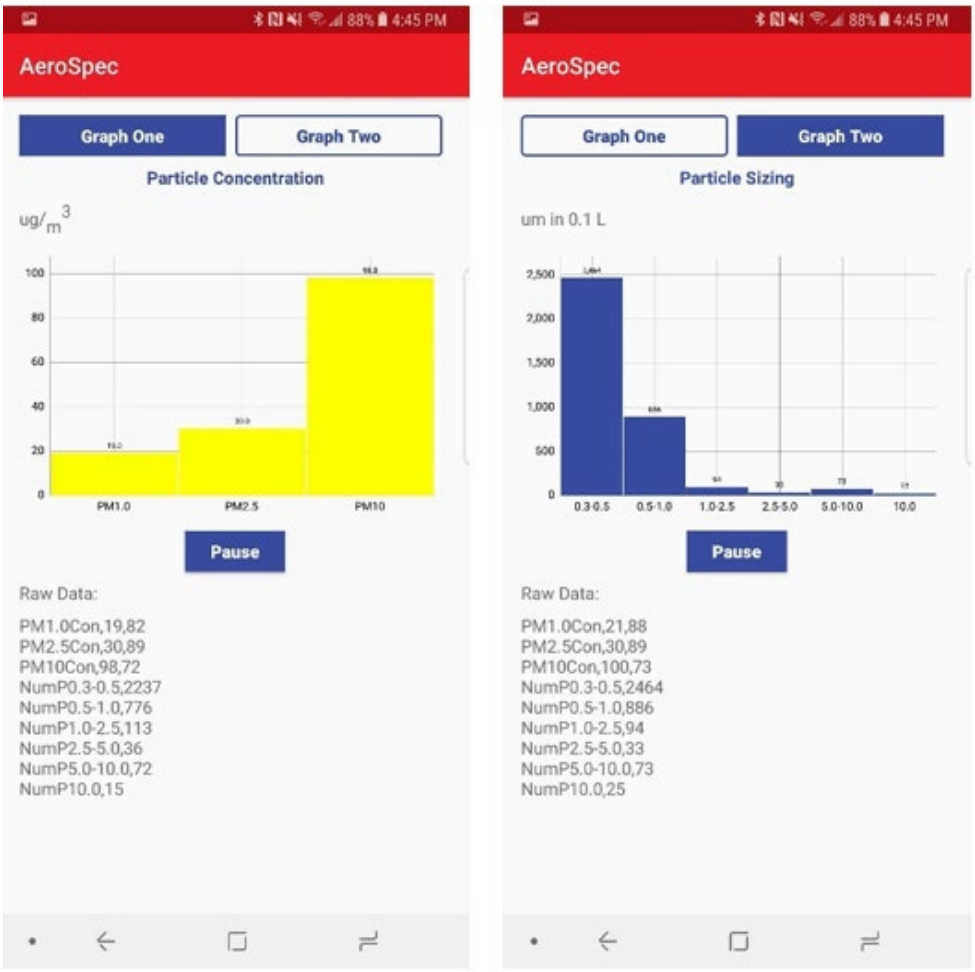

Figure 7.7. Screenshots of the AeroSpec application demonstrating both particle concentration and particle sizing.

The smartphone application is validated using the standard Android Core App Quality. The tests were done to verify AeroSpec meets the specifications, which shows the data from the sensors were able to be read and displayed on the application properly. Testing was done by running through some of the listed Core App Quality tests. Through testing, AeroSpec was verified to accurately and reliably read data from the AeroSpec hardware every 0.8 seconds. There were issues in meeting some of the Core App Quality tests, but they did not interfere with the core functionality of the application.

7.2.2 *The Experimental Design*

Validation of the AeroSpec system includes testing location tracking (i.e., indoor, outdoor), air quality data accuracy, and data transmission reliability. The AeroSpec system has been tested in different deployment scenarios, but, more importantly, it was put to the test as a mobile system side-by-side lab-certified particle concentration equipment. The location tracking data was also compared with the state-of-the-art GPS modules used in current smartphones. Figure 7.8 shows the user interface of the AeroSpec's web portal, showing the floor map of the Clean Energy Institute in Seattle, WA, USA. The highlighted locations are tracked using the GPS unit; all areas matched the areas found by the smartphones.

To validate the accuracy of the air quality data, the particle concentration data was converted to AQI (Air Quality Index). There are different concentration breakpoints to calculate AQI for different particles, such as $PM_{0.3}$, PM $_{0.5}$, $PM_{0.7}$, $PM_{1.0}$, $PM_{2.5}$, and $PM_{10.0}$. The *AQI* was calculated using (32) and the concentration data obtained.

$$AQI = \left(\frac{(PM_{obs} - PM_{min})(AQI_{max} - AQI_{min})}{PM_{max} - PM_{min}}\right) + AQI_{min} \tag{32}$$

where PM_{obs} means observed 24-hour average concentration in $\mu g/m^3$. PM_{min} means the minimum concentration of *AQI* color category that contains PM_{obs}. PM_{max} is the maximum concentration of *AQI* color category that contains PM_{obs}. AQI_{max} refers to maximum *AQI* value for a color category that corresponds to PM_{obs} and AQI_{min} means minimum *AQI* value for a color category that corresponds to PM_{obs}.

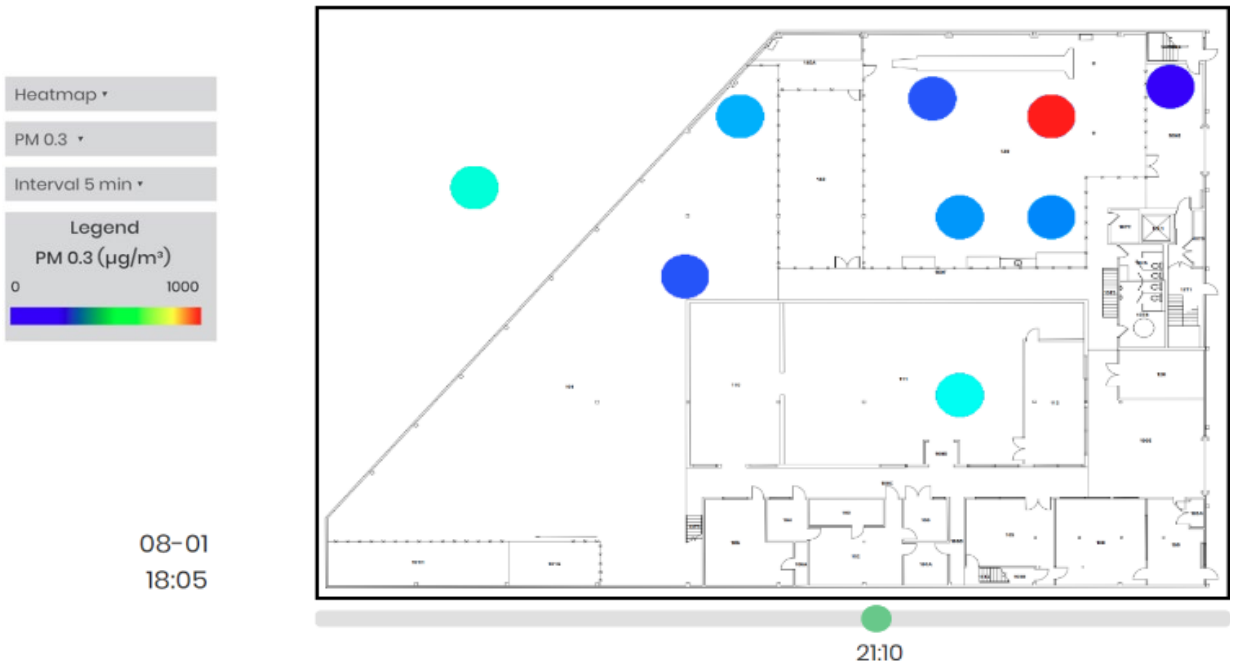

Figure 7.8. A snapshot of a real-time sensor network output. Here, the sensors are stationary and record localized pollution associated with indoor processes.

The AeroSpec algorithm reads AQI values calculated in the ATmega328P chip over serial communication. The algorithm reads the ASCII value of AQI and converts it to characters. This calculated value is then plotted on the graph in real-time, as shown in Figure 7.9 and Figure 7.10. This data is taken from a single AeroSpec unit by a subject walking around the factory floor and uploading data in real-time.

The data transmission of the system was validated with upload rates of 0.8 minutes to 10 minutes. The results show neither delays nor data loss in all of the uploads.

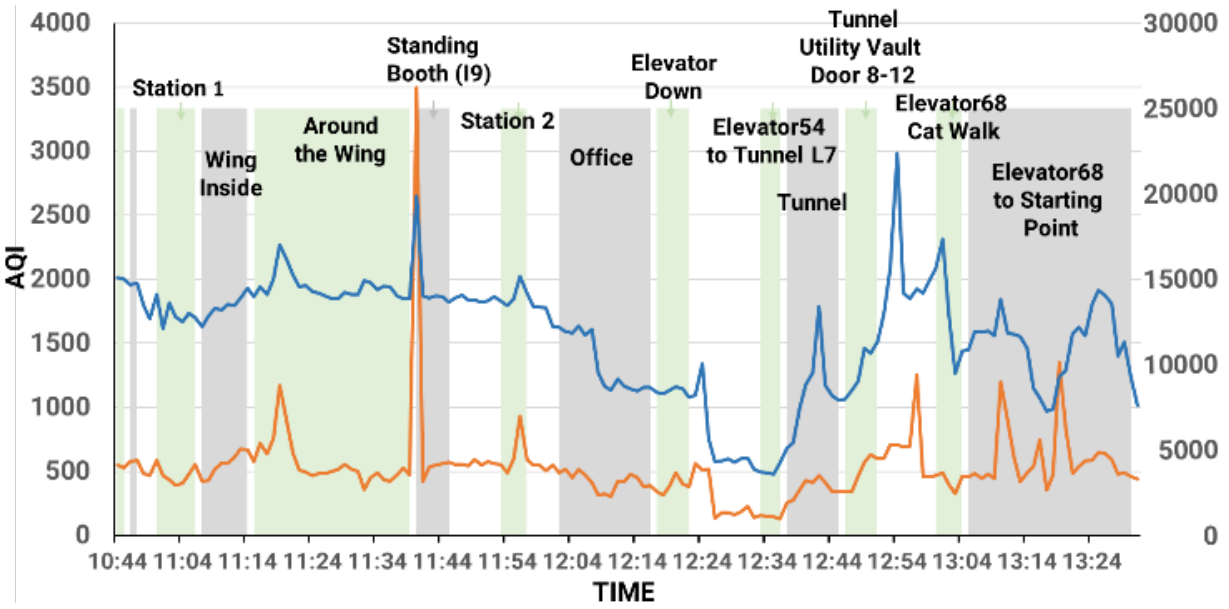

Figure 7.9. Micron particle detection using the AeroSpec system. The unit is moved inside a selected factory floor while it detects in real-time.

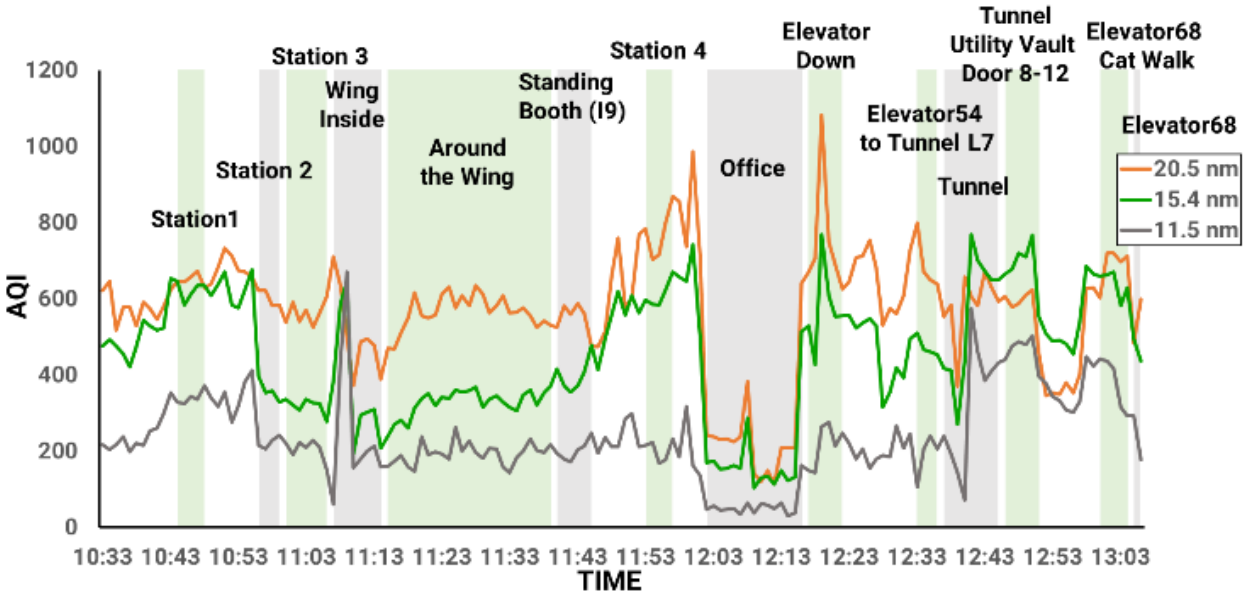

Figure 7.10. Nanoparticle detection using laboratory rated testing equipment. The unit is moved inside a selected factory floor while it detects in real-time.

7.3 DISCUSSION

Location-based tracking and cloud computing enables the system to capture geolocation, meteorological data, and transfer them in real-time to the cloud. By analyzing this data, the system alarms the user to avoid further exposure and introduces intervention techniques for daily exposure. PM concentrations are known to vary significantly [100, 101]. Hence, time- and size-resolved PM measurements are more informative than traditional total PM weight measurements for assessing negative health effects. The U.S. Environmental Protection Agency (EPA) has adopted the PM_{10} and $PM_{2.5}$ criteria for monitoring air quality [102, 103]. However, the low spatial density of fixed monitoring sites makes personal exposure assessment challenging [104].

Tests were performed to verify that AeroSpec met the specifications and showed that the air quality data from AeroSpec hardware was able to be read and displayed on the smartphone application and web portal properly. These tests were done by running through the listed Core App Quality tests. After testing, AeroSpec was verified to accurately and reliably read data from the Plantower system every 0.8 minutes to 10 minutes with a response rate of less than 1 second to alarm its user of any hazardous exposure. The accuracy of the data was within 5% of the expensive lab certified equipment.

Traditional PM instruments are large and expensive; thus, they have limited use in high spatial and temporal resolution mapping applications; these applications instead demand compact, low-cost sensors with reliable performance. While there is an increasing number of sensor technologies being developed every year, their use in health research has been hindered by the lack of available ready-to-use data management, validation and analysis tools, and hardware and software solutions. The AeroSpec has significant advantages over existing low-cost devices. It allows for the sizing

of individual particles and data averaging of other compact PM sensors and reduces the errors associated with PM optical properties [97].

7.4 CHAPTER SUMMARY

Fine and ultrafine PM exacerbate asthma and cause cardiovascular and respiratory diseases. The particle detection devices are expensive and bulky, limiting their application in wearable devices. This chapter presented the use of location-based automation in air quality management applications. Knowing the location of the PM exposure enables the researcher or physician to create personalized intervention strategies. The AeroSpec system utilizes a modular set of environmental sensors to capture personal PM exposure accurately and to upload and analyze the results using cloud computing in near real-time. The user can access the information via a phone or web portal. The GPS sensor of the system allows tracking of the device to create the heat map of an outdoor or indoor location. The results show a 95% accuracy when compared to the lab-certified equipment.

Chapter 8. DATABASE MANAGEMENT AND LOCATION-BASED AUTOMATION IN ENVIRONMENTAL DISEASE SURVEILLANCE

In Chapter 7, the use of location-based automation and cloud computing features adapted from the dietary measurement was evaluated in the field of personal air quality monitoring. This chapter discusses another epidemiological application in environmental disease tracking. Specifically, the location-based automation and cloud computing features presented in this thesis have been used to develop a novel web-based system called the Electronic Environmental Surveillance System (EESS). The EESS includes a corresponding geolocation-tracking and Quick Response (QR) and generates a mobile and web application to engage and track participants throughout the collection and the analysis of the data. The EESS initial evaluation was completed by going through a beta study using a novel sampling and concentration system: the bag-mediated filtration system (BMFS) [105-107]. The BMFS is used in detecting poliovirus in the three remaining polio-endemic countries: Afghanistan, Pakistan, and Nigeria. The beta study was done using 15 volunteers; each volunteer used the EESS application at two different locations around the greater Seattle area.

8.1 MOTIVATION

The application of environmental surveillance to public health issues is becoming more prevalent with increased access to global positioning systems (GPS) and programs which aid in disease tracking. However, disease tracking can be hindered by collection at incorrect or improperly reported locations. Longitudinal data from inconsistent sites can confound the verification of elimination. Also, manual reporting and management of the data have caused

processing delays and inefficiency. There are instances where sampling does not occur at the designated sampling location, resulting in incorrect information about environmental diseases [108-110]. Geospatial data, since the utilization of it in the London cholera epidemic of 1854, has been instrumental in tracking, surveilling, and aiding in eliminating environmental diseases.

8.2 Background of Environmental Disease Surveillance

Sampling methodology and data collection have been a focus on related efforts to track water-based diseases. In these studies, water samples were collected from specific locations, often in rural villages or communities. The geographic location of the samples was critical to the data integrity and analysis of results. The date and time window in which the samples were collected was an additional requirement. This information was recorded along with water samples and transported to a lab for analysis in each related study.

In Rural India, community water sources are monitored for human and animal fecal contamination, which eliminates the spread of disease particularly harmful to children and infants. Water samples were collected across rural coastal communities in Odisha State in India from both water sources and households. A 500 mL water sample from a household and 20 liters of 2L samples from a corresponding water source were collected within a 3-hour window and transported to a lab facility within 8 hours. The location of the water source was crucial to analyze sample results against those taken from the household. In Southeastern Brazil, 117 water samples were collected from a mixed rural-urban watershed to analyze the protozoan parasite Cryptosporidium. The sample site was a catchment which served as a major source of drinking water for both humans and livestock. Sample locations were identified where stream tributaries met, and 2L samples were taken monthly [111].

Water sampling collected in the study of fecal contamination in India presents challenges in accurately sampling water at the correct location. Reaching rural villages and communities could prove difficult when mapping water sources to household drinking water. A 3-hour time window is an additional constraint that could result in hasty water sampling at an alternative location for convenience. The water sampling conducted in Brazil could face difficulty in accurately tracking sample location as well. Technicians may sample from the incorrect location if they are unfamiliar with rural terrain. A monthly sampling time could result in different technicians conducting sampling, which further adds uncertainty to the accuracy of the sample location [112].

Integration of the EESS automates the data collection process of similar studies, such as tracking polio. The EESS initial evaluation was completed by being integrated into a novel sampling and concentration system: the bag-mediated filtration system (BMFS.) The EESS would prevent incorrectly or improperly reported locations of the water sample sites. The information collected in this study is verified and logged into the database automatically sorted.

8.3 Electronic Environmental Surveillance System (EESS)

8.3.1 The Functional Design

The Electronic Environmental Surveillance System (EESS) consists of a smartphone or a tablet, which includes a GPS sensor and wireless connection via a cellular and a Wi-Fi chip, a database server to store and process the data on the cloud, and the main EESS processing algorithm. Although the system and methods described here were specifically built to help track poliovirus cases, the same system could easily be modified so that other disease tracking studies could employ the same tactics. Previous records were kept using a paper-based frequency questionnaire written by hand using pen and paper. The switch to electronic methods of recording

is expected to be more accurate, more comfortable to keep track of, easier to use, and more organized. Figure 8.1 shows the overall design of the EESS system.

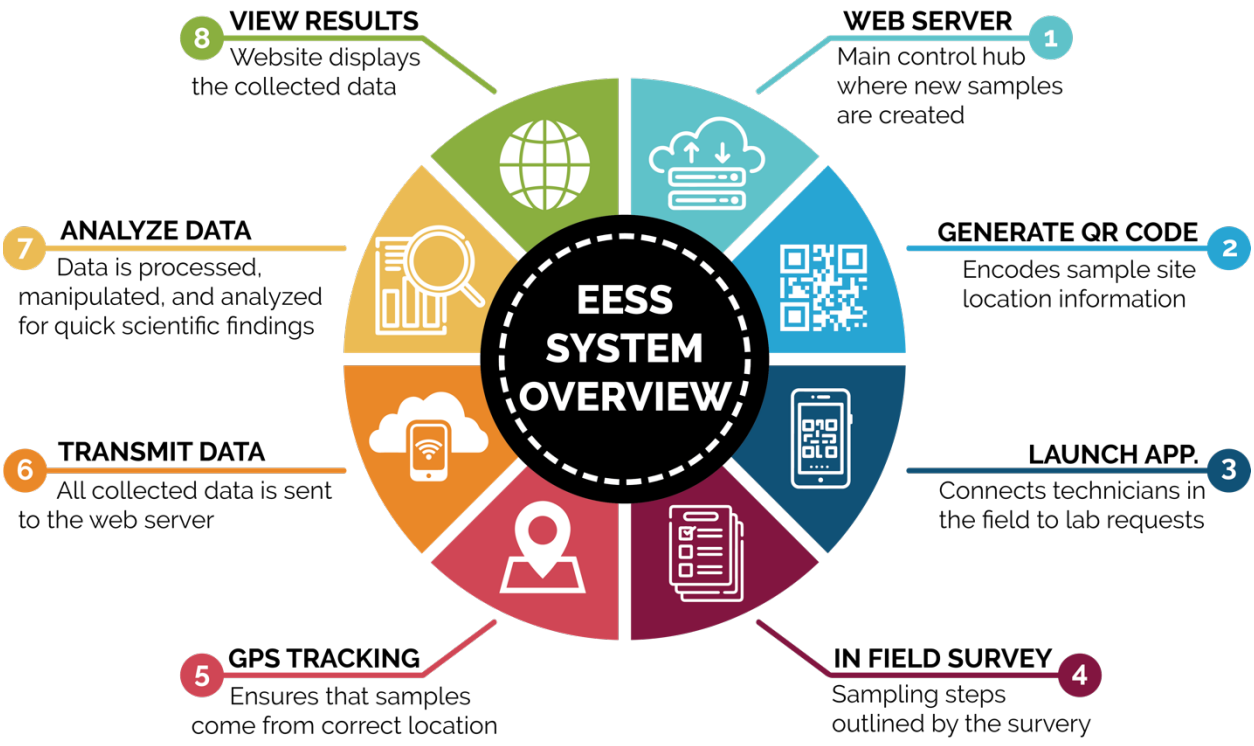

Figure 8.1. Overview of the entire system. The website generated QR codes scanned by field users during the questionnaire stage of the sampling. The smartphone application allows automatic capture of location during the survey.

The main system is composed of a web server and a mobile application. The web server is the main control hub, from which new cases can be created and assigned, and data can be viewed. The mobile application is used to collect sample data from testing locations (using the GPS sensor) and connect to the webserver to display the collected data. Figure 8.2 shows the theoretical functional design of the EESS system.

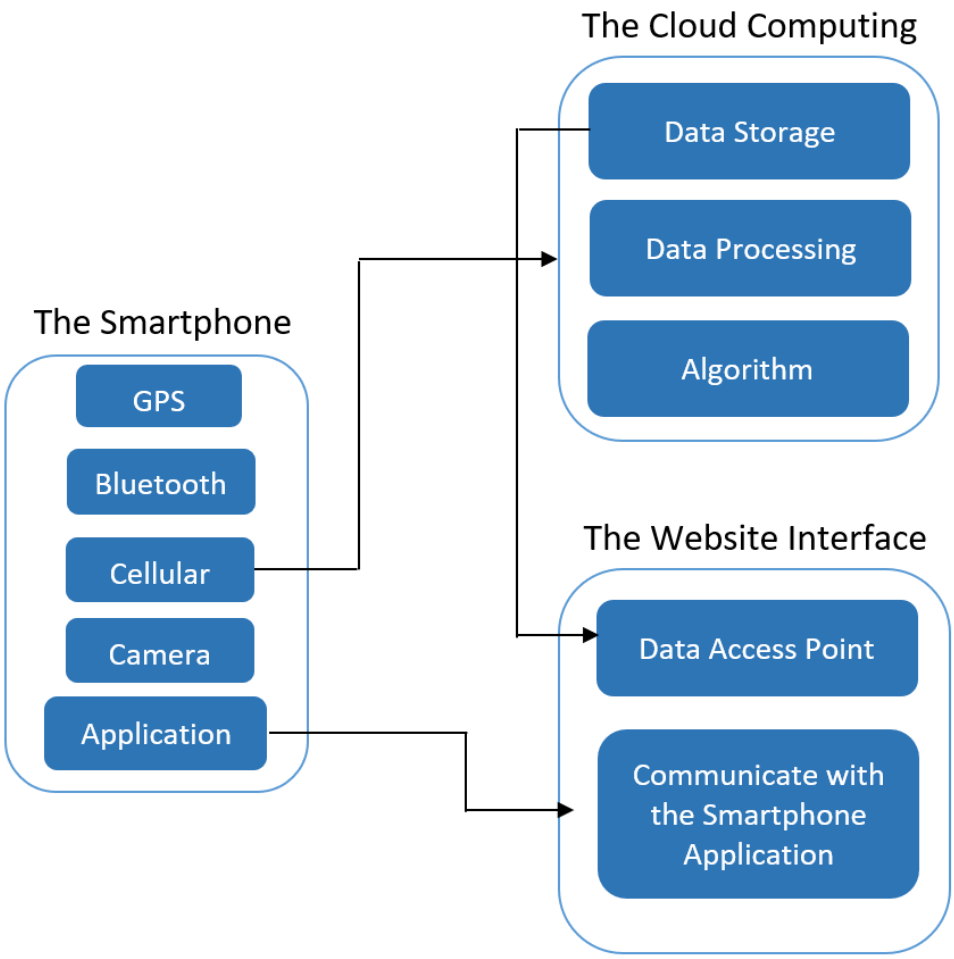

Figure 8.2. The EESS functional design flowchart.

The objective of this study is to develop a novel location-based data processing mobile system, which would automate a majority of data collection and processing by tracking geolocation and time. The smartphone application was developed for Android devices with Assisted GPS (A-GPS), to ensure that the application would be supported by the devices that were already in use by field testers. The application implements a step-by-step survey system for data collection, to simplify the overall process for the field agent and increase data efficiency for the researcher.

The data collection process begins once the tester has arrived at the testing site. Each tester possesses an Android tablet, thus eliminating the need for a login process. Before any testing can begin, first, the smartphone application needs to check the status of the GPS tracking. If GPS tracking is not available (e.g., Airplane Mode is enabled, no signals in rural areas), the application's functions are disabled, and the user will be notified to record geolocation manually. To begin the sampling process, the QR code that is attached to the filter housing is scanned at each step of the BMFS sampling process using the mobile application. The tester then selects which step they have just completed, and GPS coordinates are automatically gathered by the device when a successful scan occurs. The QR code contains information about the identity of the tester, the case number, and the expected testing location. A survey corresponding to the selected step is presented for the tester to fill out. Questions may refer to current/past weather, air temperature, and sample pH. The surveying continues through lab analysis, with similar survey questions being asked at each processing stage. All collected data is stored locally on the device until Wi-Fi is detected. Once detected, the application will automatically push the data up to the webserver.

The smartphone application is written in Java, which is one of the most widely used programming languages in application development [113]. Android Studio is an officially integrated development environment for Google's Android operating system and was used to develop the application [114]. As a result, the application uses frameworks and libraries from default Android Studio settings. The main code of the application includes implementations for network control, data transfer, and QR code production. Each of these codes is essential for the application. The Java code for network control detects which network the device is connected to, and the Java code for QR codes verifies the user's location and time zone by reading data from the QR code.

Additional data is collected as the user follows the instructions on the application. Eventually, the user is asked to input results from their research. A separate Java class manages the data from the QR code and the user's inputs. This data is either stored in the device or sent to the webserver, depending on the Wi-Fi connection. Figure 8.3 summarizes where the information is collected and how the application manages the data.

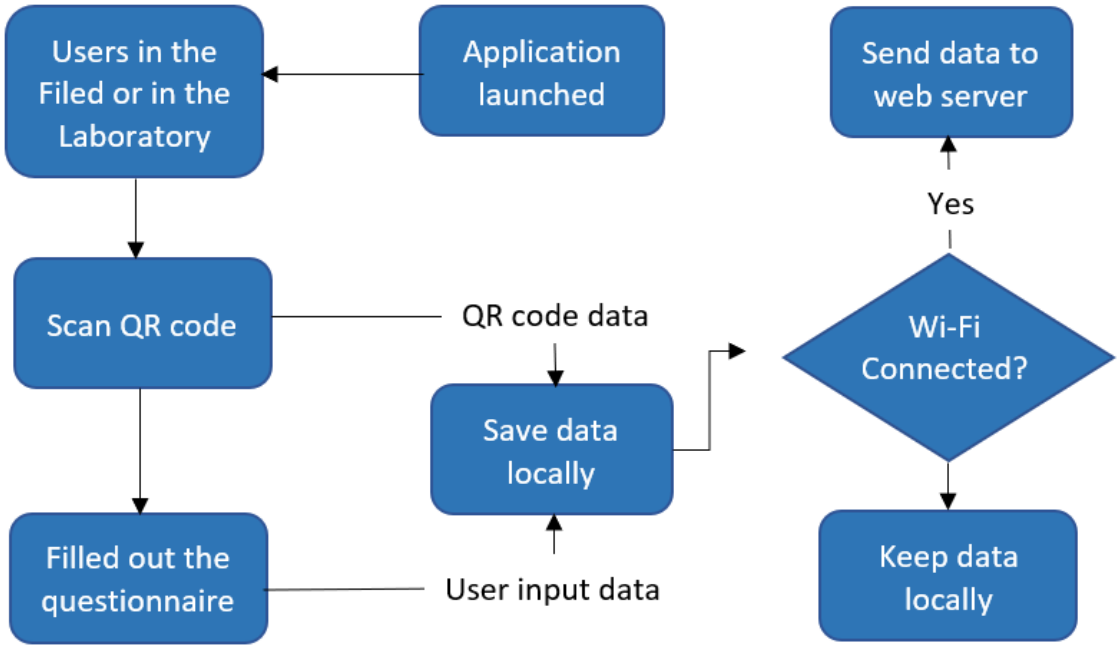

Figure 8.3. Flowchart of logic in Java code. The flowchart shows how the data is being managed while the user is using the application.

For the User Interface (UI), the focus was to make it as simple as possible. The UI does not have a verification or login page because these applications will only be installed on devices that are confirmed to be used by researchers in the research study. Hence, the UI is built with an assumption that the user is familiar with the content of the research. An example of the UI is given in Figure 8.4.

Figure 8.4. An example of the UI used in the mobile application.

The implementation of the web server includes multi-level access for different types of users, a computational algorithm, and the web interface. The server access includes four different types of accounts: IT, administrator, moderator, and user. Those with an IT account can view data and create any sample cases in any location. Users with an administrator account can create sample cases and view data from multiple countries or a region, e.g., the Middle East. Moderators can create sample cases and view data for multiple cities within a country, and the regular user account

will be able to view data for multiple sites within a single city. The main features of the web server include 1) multi-access level user accounts (IT, administrator, moderator, or user,) 2) sample identification (ID) codes, 3) new testing city and site location database, 4) Quick Response (QR) generator, and 5) post-processing algorithm. Additional implemented features include interaction and communication through the web interface with the mobile devices, as well as a report generation to generate comma-separated values (CSV) files. By using the report generation function, any users with the ability to view data can sort and request data that fit specific criteria, including date, GPS coordinates, users assigned to a sample case, city, and region. Administrators and moderators begin by creating new case studies by submitting sample identification (ID) codes and the testing site's location. Sample ID codes and testing site location information is encoded within a QR code, which is printed out and affixed to a corresponding BMFS filter housing. The date, time, GPS coordinates (latitude and longitude), and any notes from previously collected data are viewed through the website.

The website was built using various programming languages. Hypertext Markup Language (HTML5) is used to structure web pages [115]. Cascading Style Sheets (CSS3) is used to design the website and is in charge of the website's presentation. JavaScript takes care of the communication between front-end user input and the back-end data. The framework for the website is Laravel5.4, which is a robust, elegant, and scalable framework [116]. As a result, the interface and the main structure come from the standard Laravel framework. The website is using a My Structured Query Language (MySQL) database, which is a database that is used worldwide when building the back-end of the website [117]. PHP Data Objects (PDO) database layer, which is a compatible database layer, ensures that the data is secure [118]. With this layer, it is easier for

developers to fetch or query data because the layers allow the developer to be less dependent on the database itself. Figure 8.5 shows the back-end data flow design

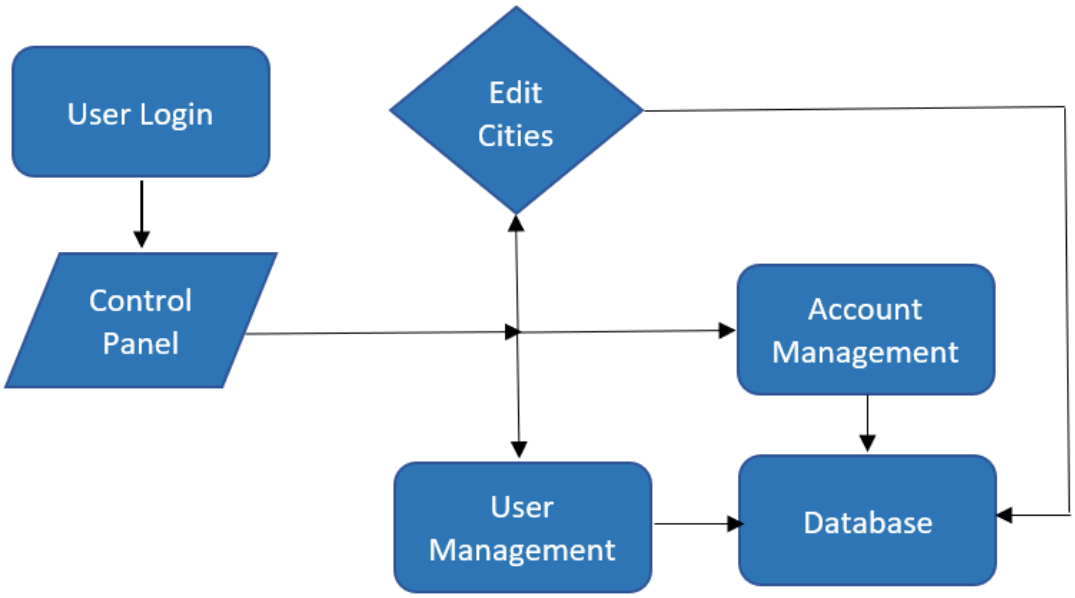

Figure 8.5. Back-end data flow of the website. Every data input, such as new city locations or research questionnaires, gets saved into the server.

The testing scheme consists of two main tests: a test for the mobile and web application functionalities, and a test for GPS accuracy. The purpose of the mobile and web application test was to determine the accuracy and reliability of mobile and web applications. Both applications should be fully functional by themselves (e.g., the mobile application correctly uploads the data onto the server; the web application can sort and filter data correctly). To implement the beta test on the mobile application, the following was necessary: (1) A minimum of 10 beta testers with no involvement or any prior knowledge of the app and web development, (2) a 1-hour group training session for all testers, (3) two specific text case scenarios for each tester, (4) an Android smartphone or tablet with the mobile application installed for each tester, and (5) a physical (paper) copy of the field survey with pre-filled questions and a physical copy of the field survey with blank questions for each user.

8.3.2 The Experimental Design

The first step in testing the system involves loading the application onto tablets used during the studies. The next step is for administrators and/or moderators to create studies using the website. The QR code encodes information such as country, city, site, and sample ID. Once the QR code is scanned, the collected data can be associated with the correct study.

Once field and laboratory data have been collected, it is automatically sent to the servers when Wi-Fi has been detected. From there, IT, administrators, and/or moderators will be able to view and download the desired data. As shown in Figure 8.5; users can filter data by adding tags. Possible tags include the location name (continent, country, state, etc. name), site name (city, landmark, etc. name), case study number, and date range of the gathered data.

This study included tracking fifteen different subjects who reported data from their homes and offices. In each location, the volunteers answered questions with given answers into their Androids. The questions are split into five sections: BMFS sample preparation, the start of settling, the start of filtration, the end of filtration, and the preparation of shipment to the lab. This data was automatically stored and sent to the database.

After they finished, volunteers were asked to fill out a usability form evaluating their experience with the app. These questions included how long they estimated it would take to fill out the chain of custody commands at either location, the ease of use on a bipolar scale, and whether they thought it was easier to use the second time at a different location. Lastly, participants were asked about any thoughts they had on ways to improve the application.

Volunteers were recruited from the Fred Hutchinson Cancer Research Center and the University of Washington Department of Environmental and Occupational Health Sciences and their families.

8.3.3 Discussion

Similar to traditional dietary measurement techniques, in tracking participant responses, researchers in disease surveillance, use manual and handwritten notes. The location-based automation and cloud computing allows for the automation of data collection. Twenty different data points were taken for each sample, and each participant had four samples done (one at home and one at work with written and mobile measurements for each location). Thus, there were 80 data points taken for each of 15 participants or a total of 1200 data points. (With four observed errors in the data, our error rate comes out to be 4/1200 or 0.33%.)

Furthermore, minor differences were seen in the location data reported across the written and mobile platforms, shown in Figure 8.6. An interactive map of the location data at home and work for the volunteers can be found in [119]. This data shows that for testing sites that are located within approximately 5 miles of one another, location tracking may be less accurate in determining whether volunteers are performing analysis in the correct locations. However, the system accuracy is above the threshold to be applied towards most cases of environmental surveillance, where testing sites are located many miles apart.

Across the fifteen volunteers, participants reported a lower average sampling time when using the mobile application in comparison to manual recording.

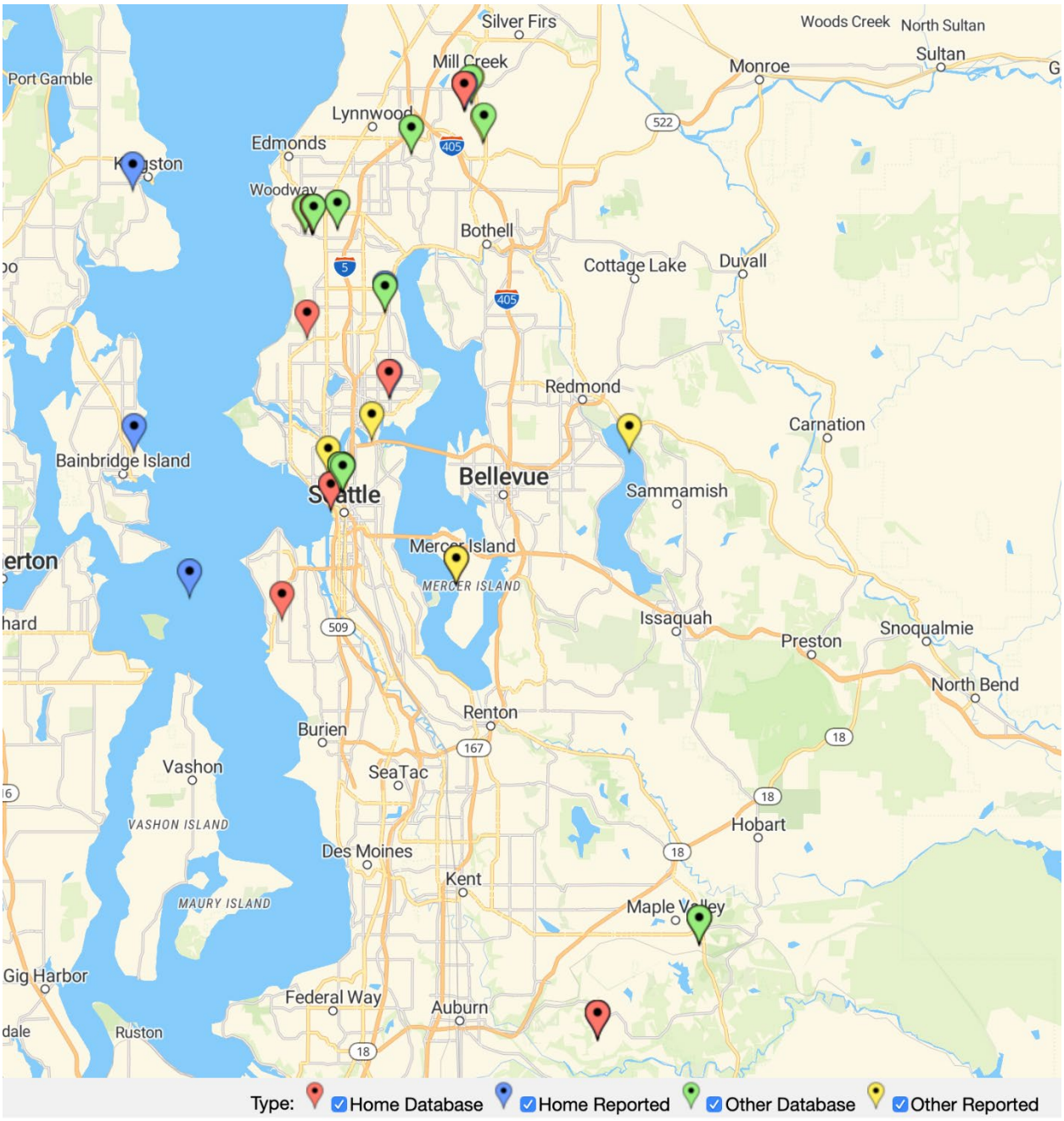

Figure 8.6. Representation of the locations for each. Red and green pins show the first location using the EESS system, blue and yellow show the second location captured using an off the shelf GPS sensor.

8.4 CHAPTER SUMMARY

Effective location-based environmental surveillance systems allow automating the data collection processes while keeping the efficiency consistently high. Location-based data processing allows meteorological data to be captured and processed to automate the data collection, and produce self-processing algorithm and data management. This chapter discussed the development and testing of the Electronic Environmental Surveillance System (EESS), which is based on the database and location-based automation design of the dietary measurement technique presented in this thesis. The developed EESS system design showed improvement in data accuracy and data acquisition time when compared to paper-based solutions. System evaluation was conducted by integrating the EESS system into a polio surveillance system called Bag-Mediated Filtration System (BMFS). The preliminary results have shown consistency of 99% in data transfer and location tracking, and initial user testings have received a very positive feedback. The system is working with WHO for the deployment of the EESS in Dhaka and Kenya.

Chapter 9. LMITATIONS AND FUTURE WORK

9.1 LIMITATIONS OF 3D MEASUREMENT TECHNIQUES

9.1.1 Limitations of 3D measurement in Dietary Assessment Techniques

9.1.1.1 Limitations of the DDRS Approach

Automatic Dot Detection: Two possible limitations of the algorithm occur with dark-colored liquids, such as wine, and foods with very high reflectivity. These objects do not show the laser dots very well, and it is challenging to detect the dots with the current algorithm. However, the limitations depend on the hardware, for instance, on the luminance of the lasers.

Segmentation: Another limitation of this algorithm is the use of static thresholding variables throughout the software, specifically, when the object is relatively small regarding pixels and the structuring element constant in the erosion is large. In this case, some of the dots near the edges are not captured. Characteristics of the images must be analyzed to determine how to make these threshold values dynamic.

This limitation can be explored in numerous ways. One way is to replace the static thresholding values of the algorithm with dynamic values. The thresholding check is repeated multiple times throughout the algorithm; thus, it has a significant impact on the accuracy of the results. The current static thresholding values are set to values that were determined through testing on various images and resulted in consistently accurate and stable results. While we expect these fixed values to yield reasonable results on simple images, the algorithm is likely the cause for less reliable results on more complex images.

Another way to bypass this limitation could be to enhance the auto-segmentation section of the algorithm. The current version of the algorithm is shown to yield highly accurate results for images with only a single object. The auto-segmentation algorithm could be expanded to detect

the presence of multiple objects from the plate, and, as a result, to create multiple separately segmented images, each with a single food object in them. We expect this expansion of the auto-segmentation process to improve the current version of the algorithm immediately.

Additionally, the saliency map has very high accuracy when images are manually cropped to contain just the food. This is because manual cropping by a user provides a tightly bound image around the food as compared to the original. Hence, one place where the current auto-segmentation process could be improved is in the second stage. This stage performs a rough segment of the image with larger structuring elements instead of a tight bound, before passing the segmented image to the HSV filter. A more accurate method could be designed to crop the image from the first crop of the plate to the second crop of the food using either edge detection or color segmentation. This might present less noise than the current HSV thresholding done in the second crop, thus passing on a more certain crop to the saliency mapping function.

9.1.1.2 Limitations of the DietSkan Approach

The DietSkan system was effective in increasing the accuracy of current methods in dietary tracking. The scanner was useful for obtaining accurate volumetric estimations through 3D reconstruction and boosted the accuracy of the nutritional data filled by the medical staff. From the results, it is seen that the DietSkan system had an overall lower absolute error when compared to the 24HR method and MyFitnessPal. Importantly, it was also able to consistently achieve a smaller error, indicated by the low standard deviation.

The DietSkan was tested in a hospital setting and utilized the hospital's kitchen database to automate the calculation process. While the database access improves the quality of the results, it limits the DietSkan's adaptability to other dietary measurement applications.

9.1.2 Limitations of the Wafer Fitting System (WFS) Approach

The Wafer Fitting System has shown great potential in a laboratory or controlled setting. However, many limitations are considered, cost, complexity as a home-use system, and the learning curve, especially for the elderly, who are the primary demographic of WFS. There are barriers to elderly smartphone usage [120], but there is growing success in reducing these barriers (e.g., improving phone interface accessibility [121], simplifying user interaction with the phone [122]). Traditional non-technology approaches that use mirrors, hand-cut wafers, and other high-vision, high-dexterity tools are not elderly-friendly, either. Different users required different solutions in almost every field and every market. There will be some patients who will not adopt a technology-based system.

9.2 FUTURE WORK

9.2.1 3D measurement Techniques

9.2.1.1 Dietary Assessment

Further study in utilizing different 3D measurement techniques showed improvement in performance and robustness. Newer algorithms, such as the one discussed in [123], suggest that it may be possible to get better results by distinguishing between different hole sizes and performing the appropriate filling method. While hole size alone might not be enough for automatic mesh fixing, additional characteristics of the mesh and boundary, such as the type of hole formed (simple or complex), as well as some known information about the item, may help in improving this step. Development in making the scanning process more autonomous would also improve the usability and accuracy of the system with the added benefit of solving some of the problems faced during mesh formation. One such method would be to find the means to automate the segmentation

process. Algorithms to separate food items from the plate, as well as each other automatically, would increase the accuracy and usability of the system.

Complete system automation would entail the above steps, as well as automating the hole-filling processing, to make the system entirely devoid of human input except for edge cases. Such a system also opens the possibility of the system being modified to be directly used by patients with training instead of only medical/nutritional staff. This would relieve some burden from the medical team while maintaining the requisite quality for proper treatment.

Finally, to establish the actual real-world performance of the DietSkan system, larger-scale studies have to be conducted. For this purpose, the possibility of performing a beta study at the Harborview Medical Center, Seattle, WA, USA, is being explored. The DietSkan system would be integrated with the current system in place. The field evaluation would also allow better understanding for real-life scenarios with more feedback from staff and patients.

9.2.1.2 Wound Care Management

Future directions for the wound care management system include addressing the challenges of information security by adding functionality so that 3D profiles of the stoma (as well as other relevant data) generated during regular self-care will be safely transferred to their medical care professional. This information can then be used to support digital and longer-distance stoma monitoring and stoma care. The ability to monitor the status of the stoma remotely could allow for the identification of early warning signs of the many stoma complications that occur.

9.2.2 Location-Based Data Processing

Location tracking has become one of the most crucial data in both research and consumer products. The importance of geolocation allows the understanding of different behaviors and environmental impact-driven patterns. Achieving meaningful geolocation-related patterns in

behavior is possible by using location-based data processing. With the rapid improvement of artificial intelligence (AI), IoT, and smart devices, the location-based data processing will become more advanced and sophisticated in the near future. This dissertation presents a location-based use case in dietary assessment techniques in the hospital. Future work will include the use of geolocation to automatically narrow down the choices of meals purchased outside of a home using a variety of online food databases.

In addition to dietary applications, the author has done preliminary work on two other location-based data processing application: 1- air quality monitoring, and 2- disease tracking. The air quality monitoring system, AeroSpec, uses GPS data to create a realtime heat map of personal exposure with a high resolution using a network of sensors. It is crucial to know the exact location of any pollution source for the purpose of elimination or maintenance. The AeroSpec team is currently working with Boeing to conduct a large scale study of air quality effects around airports. Another current work funded by the Bill and Malinda Gates Foundation looks at location-based data processing in disease tracking. Specifically, the Electronic Environmental Surveillance System (EESS) used GPS data and data processing to create a disease distribution and pattern detection technique. The team is currently working to collaborate with the World Health Organization (WHO) for the evaluation of the system in Poliovirus tracking in rural areas.

Chapter 10. CONCLUSIONS

In recent years, 3D measurement techniques have entered both research and consumer industries. 3D measurement techniques improve on traditional approaches by proposing advanced and sophisticated sensors, high-quality cameras, and image processing techniques to reduce performance limitations and user burden. However, due to the high cost, complexity, and adaptability of different use cases, current 3D measurement techniques are not commonly used in industrial applications, such as dietary assessment and wound care management. In this contribution, a novel 3D measurement is presented to address the limitations of dietary assessment and wound care management fields. Specifically, this dissertation investigates the use of 3D reconstruction techniques in the volumetric calculation of an object.

Current advancements in 3D scanning technologies show great promise for 3D reconstruction tools. However, the lack of more advanced reference-based and volumetric measurement solutions has brought significant research and development efforts into assistive image processing algorithms.

The objectives discussed in this study were: 1- improving the accuracy of volumetric measurement compared to existing techniques, 2- designing and developing a depth sensor for volumetric analysis, and 3- evaluating and testing for dietary and wound care management applications. This dissertation attempted to achieve these objectives by designing a 3D measurement technique, which leads to the development of the Digital Dietary Recorder System (DDRS), the DietSkan system, and the Wafer Fitting System (WFS). The DDRS and the DietSkan system were both tested in the dietary assessment field, and the WFS was tested in the post-operative stoma care management field.

The findings of this contribution demonstrated that the use of low-cost depth sensors in 3D measurement applications drastically improved the quality of automated volumetric measurement techniques. Using a multi-layered image processing algorithm to eliminate the unwanted background and create a closed spatial model is a required step in calculating volumetric data.

Ultimately, the long-term success or failure of 3D-based measurement will depend on the technologies' key advantages, including depth sensing, vision sensing, and machine learning. When 3D-based analysis finds a place in hospitals and medical clinics for dietary assessment, it is likely that 3D-based analysis will spread to other applications, such as for wound care management.

BIBLIOGRAPHY

[1] M. Woodward, *Epidemiology: Study Design and Data Analysis, Third Edition*. CRC Press (in en), 2013, p. 844.

[2] M. Garcia *et al.*, "Global cancer facts & figures 2007," *Atlanta, GA: American cancer society,* vol. 1, no. 3, p. 52, 2007.

[3] M. B. Schulze, S. Liu, E. B. Rimm, J. E. Manson, W. C. Willett, and F. B. Hu, "Glycemic index, glycemic load, and dietary fiber intake and incidence of type 2 diabetes in younger and middle-aged women," (in en), *Am J Clin Nutr,* vol. 80, no. 2, pp. 348-356, 2004/08/01/ 2004. [Online]. Available: http://www.ncbi.nlm.nih.gov/pubmed/15277155.

[4] "National Diabetes Statistics Report | Data & Statistics | Diabetes | CDC," (in en-us), 2020/04/21/T06:47:18Z 2020. [Online]. Available: https://www.cdc.gov/diabetes/data/statistics/statistics-report.htmlfiles/309/statistics-report.html.

[5] J.-S. Shim, K. Oh, and H. C. Kim, "Dietary assessment methods in epidemiologic studies," *Epidemiology and Health,* vol. 36, 2014/07/22/ 2014, doi: 10.4178/epih/e2014009.

[6] S. Makhsous, J. Gentsch, J. Rollins, Z. Feingold, and A. Mamishev, "DietSkan: Food Volume Estimation for Dietary Intake Analysis Using 3D Mesh Scanning," *International Journal of Engineering & Technology,* vol. 7, no. 4.38, pp. 1368-1371, 2018 2018.

[7] S. Makhsous, "High Accuracy Mobile 3D Scanning Using Structured Laser Beam Patterning," Master Thesis, University of Washington, Seattle WA, 2016. [Online]. Available: http://hdl.handle.net/1773/38037

[8] S. Makhsous, H. M. Mohammad, J. M. Schenk, A. V. Mamishev, and A. R. Kristal, "A novel mobile structured light system in food 3D reconstruction and volume estimation," *Sensors,* vol. 19, no. 3, p. 564, 2019 2019.

[9] S. Makhsous, A. Zielinski, and A. V. Mamishev, "Post-Operative Stoma Management Based on 3D Image Reconstruction and Pattern Recognition," *FSDM,* vol. 309, pp. 794-801, 2018 2018, doi: 10.3233/978-1-61499-927-0-794.

[10] S. Makhsous, M. Bharadwaj, B. E. Atkinson, I. V. Novosselov, and A. V. Mamishev, "DietSensor: Automatic Dietary Intake Measurement Using Mobile 3D Scanning Sensor for Diabetic Patients," *Sensors,* vol. 20, no. 12, p. 3380, 2020.

[11] H.-C. Chen *et al.*, "Model-based measurement of food portion size for image-based dietary assessment using 3D/2D registration," *Measurement Science and Technology,* vol. 24, no. 10, p. 105701, 2013.

[12] H.-C. Chen *et al.*, "Saliency-aware food image segmentation for personal dietary assessment using a wearable computer," *Measurement Science and Technology,* vol. 26, no. 2, p. 025702, 2015 2015.

[13] S. L. Lim, K. C. B. Ong, Y. H. Chan, W. C. Loke, M. Ferguson, and L. Daniels, "Malnutrition and its impact on cost of hospitalization, length of stay, readmission and 3-year mortality," (in English), *Clinical Nutrition,* vol. 31, no. 3, pp. 345-350, 2012/06/01/ 2012, doi: 10.1016/j.clnu.2011.11.001.

[14] N. C. I. Nih, "24-hour Dietary Recall (24HR) At a Glance | Dietary Assessment Primer," 2016/10/19/21:24:24 2016. [Online]. Available: https://dietassessmentprimer.cancer.gov/profiles/recall/.

[15] R. Almaghrabi, G. Villalobos, P. Pouladzadeh, and S. Shirmohammadi, "A novel method for measuring nutrition intake based on food image," in *2012 IEEE International Instrumentation and Measurement Technology Conference Proceedings*, 2012/05// 2012, pp. 366-370, doi: 10.1109/I2MTC.2012.6229581. [Online]. Available: files/324/6229581.html

[16] M. C. Ocké, "Evaluation of methodologies for assessing the overall diet: dietary quality scores and dietary pattern analysis," (in en), *Proceedings of the Nutrition Society,* vol. 72, no. 2, pp. 191-199, 2013/05// 2013, doi: 10.1017/S0029665113000013.

[17] F. E. Thompson and A. F. Subar, "Chapter 1 - Dietary Assessment Methodology," in *Nutrition in the Prevention and Treatment of Disease (Fourth Edition)*, A. M. Coulston, C. J. Boushey, M. G. Ferruzzi, and L. M. Delahanty Eds.: Academic Press, 2017, pp. 5-48.

[18] L. Soares-Miranda *et al.*, "Physical Activity and Heart Rate Variability in Older Adults: The Cardiovascular Health Study," (in en), *Circulation,* p. CIRCULATIONAHA.113.005361, 2014/05/05/ 2014, doi: 10.1161/CIRCULATIONAHA.113.005361.

[19] J. Shang *et al.*, "A mobile structured light system for food volume estimation," in *2011 IEEE International Conference on Computer Vision Workshops (ICCV Workshops)*, 2011/11// 2011, pp. 100-101, doi: 10.1109/ICCVW.2011.6130229.

[20] R. J. Carroll *et al.*, "Taking Advantage of the Strengths of 2 Different Dietary Assessment Instruments to Improve Intake Estimates for Nutritional Epidemiology," (in en), *Am. J. Epidemiol.,* p. kwr317, 2012/01/24/ 2012, doi: 10.1093/aje/kwr317.

[21] L. Baroni, L. Cenci, M. Tettamanti, and M. Berati, "Evaluating the environmental impact of various dietary patterns combined with different food production systems," *European journal of clinical nutrition,* vol. 61, no. 2, pp. 279-286, 2007.

[22] R. Micha, J. L. Peñalvo, F. Cudhea, F. Imamura, C. D. Rehm, and D. Mozaffarian, "Association between dietary factors and mortality from heart disease, stroke, and type 2 diabetes in the United States," *JAMA,* vol. 317, no. 9, pp. 912-924, 2017.

[23] D. Coro, A. Hutchinson, S. Dahlenburg, S. Banks, and A. Coates, "The relationship between diet and cognitive function in adult cancer survivors: a systematic review," *Journal of Cancer Survivorship,* pp. 1-19, 2019.

[24] A. Schatzkin *et al.*, "A comparison of a food frequency questionnaire with a 24-hour recall for use in an epidemiological cohort study: results from the biomarker-based Observing Protein and Energy Nutrition (OPEN) study," *Int J Epidemiol,* vol. 32, no. 6, pp. 1054-1062, 2003/12/01/ 2003, doi: 10.1093/ije/dyg264.

[25] G. H. Beaton *et al.*, "Sources of variance in 24-hour dietary recall data: Implications for nutrition study design and interpretation," (in English), *American Journal of Clinical Nutrition (USA),* 1979 1979. [Online]. Available: http://agris.fao.org/agris-search/search.do?recordID=US8045959files/483/search.html.

[26] G. Villalobos, R. Almaghrabi, B. Hariri, and S. Shirmohammadi, "A personal assistive system for nutrient intake monitoring," in *Proceedings of the 2011 international ACM workshop on Ubiquitous meta user interfaces*, 2011, pp. 17-22.

[27] P. Pouladzadeh, S. V. B. Peddi, P. Kuhad, A. Yassine, and S. Shirmohammadi, "A virtualization mechanism for real-time multimedia-assisted mobile food recognition application in cloud computing," *Cluster Comput,* vol. 18, no. 3, pp. 1099-1110, 2015.

[28] P. Pouladzadeh, S. Shirmohammadi, and A. Yassine, "Using graph cut segmentation for food calorie measurement," in *2014 IEEE International Symposium on Medical Measurements and Applications (MeMeA)*, 2014: IEEE, pp. 1-6.

[29] F. Kong and J. Tan, "DietCam: Automatic dietary assessment with mobile camera phones," *Pervasive and Mobile Computing,* vol. 8, no. 1, pp. 147-163, 2012/02/01/ 2012, doi: https://doi.org/10.1016/j.pmcj.2011.07.003.

[30] F. Kong, H. He, H. A. Raynor, and J. Tan, "DietCam: Multi-view regular shape food recognition with a camera phone," *Pervasive and Mobile Computing,* vol. 19, pp. 108-121, 2015/05/01/ 2015, doi: https://doi.org/10.1016/j.pmcj.2014.05.012.

[31] B. L. Six *et al.*, "Evidence-based development of a mobile telephone food record," *Journal of the American Dietetic Association,* vol. 110, no. 1, pp. 74-79, 2010.

[32] A. J. Harray *et al.*, "A Novel Dietary Assessment Method to Measure a Healthy and Sustainable Diet Using the Mobile Food Record: Protocol and Methodology," (in en), *Nutrients,* vol. 7, no. 7, pp. 5375-5395, 2015/07/03/ 2015, doi: 10.3390/nu7075226.

[33] J. Chae *et al.*, "Volume estimation using food specific shape templates in mobile image-based dietary assessment," in *IS&T/SPIE Electronic Imaging*, 2011, vol. 7873: SPIE, p. 8.

[34] N. Khanna, C. J. Boushey, D. Kerr, M. Okos, D. S. Ebert, and E. J. Delp, "An overview of the technology assisted dietary assessment project at Purdue University," in *2010 IEEE International Symposium on Multimedia*, 2010: IEEE, pp. 290-295.

[35] F. Zhu *et al.*, "The use of mobile devices in aiding dietary assessment and evaluation," *IEEE journal of selected topics in signal processing,* vol. 4, no. 4, pp. 756-766, 2010.

[36] S. M. Ayaz, D. Khan, and M. Y. Kim, "Three-Dimensional Registration for Handheld Profiling Systems Based on Multiple Shot Structured Light," *Sensors,* vol. 18, no. 4, p. 1146, 2018. [Online]. Available: https://www.mdpi.com/1424-8220/18/4/1146.

[37] T. Peng, Z. Zhang, Y. Song, F. Chen, and D. Zeng, "Portable System for Box Volume Measurement Based on Line-Structured Light Vision and Deep Learning," *Sensors,* vol. 19, no. 18, p. 3921, 2019. [Online]. Available: https://www.mdpi.com/1424-8220/19/18/3921.

[38] T. Guzsvinecz, V. Szucs, and C. Sik-Lanyi, "Suitability of the Kinect Sensor and Leap Motion Controller—A Literature Review," (in en), *Sensors,* vol. 19, no. 5, p. 1072, 2019/01// 2019, doi: 10.3390/s19051072.

[39] O. Wasenmüller and D. Stricker, "Comparison of Kinect V1 and V2 Depth Images in Terms of Accuracy and Precision," Cham, 2017: Springer International Publishing, in Computer Vision – ACCV 2016 Workshops, pp. 34-45.
[40] P. Fürsattel *et al.*, "A Comparative Error Analysis of Current Time-of-Flight Sensors," *IEEE Transactions on Computational Imaging,* vol. 2, no. 1, pp. 27-41, 2016.
[41] S. Shirmohammadi and A. Ferrero, "Camera as the instrument: the rising trend of vision based measurement," *IEEE Instrumentation & Measurement Magazine,* vol. 17, no. 3, pp. 41-47, 2014.
[42] G. M. Frank Chen and S. Mumin, "Overview of three-dimensional shape measurement using optical methods," *Opt. Eng,* vol. 39, pp. 10-21, 2000.
[43] J. A. Jalkio, R. C. Kim, and S. K. Case, "Three dimensional inspection using multistripe structured light," *Opt. Eng,* vol. 24, no. 6, p. 246966, 1985.
[44] E. N. Malamas, E. G. Petrakis, M. Zervakis, L. Petit, and J.-D. Legat, "A survey on industrial vision systems, applications and tools," *Image and Vision Computing,* vol. 21, no. 2, pp. 171-188, 2003.
[45] G. Zhang, Z. Liu, J. Sun, and Z. Wei, "Novel calibration method for a multi-sensor visual measurement system based on structured light," *Opt. Eng,* vol. 49, no. 4, p. 043602, 2010. [Online]. Available: https://doi.org/10.1117/1.3407429.
[46] S. Zhang and P. S. Huang, "Novel method for structured light system calibration," 2006, vol. 45: SPIE, p. 8.
[47] J. Shang *et al.*, "Dietary intake assessment using integrated sensors and software," 2012 2012, vol. 8304, pp. 830403-830403-11, doi: 10.1117/12.907769. [Online]. Available: http://dx.doi.org/10.1117/12.907769
[48] E. E. Stone and M. Skubic, "Fall detection in homes of older adults using the Microsoft Kinect," *IEEE journal of biomedical and health informatics,* vol. 19, no. 1, pp. 290-301, 2014.
[49] S. Shukor, M. A. S. Muda, A. Ali, and J. Johari, "Analysis of Mobile 3D Depth Sensors in Capturing and Modelling Indoor Scene," in *2019 IEEE International Conference on Automatic Control and Intelligent Systems (I2CACIS)*, 2019: IEEE, pp. 235-240.
[50] R. A. Clark *et al.*, "Instrumenting gait assessment using the Kinect in people living with stroke: reliability and association with balance tests," *Journal of neuroengineering and rehabilitation,* vol. 12, no. 1, p. 15, 2015.
[51] H. Essen *et al.*, "A multimodal sensor system for runway debris detection," *International Journal of Microwave and Wireless Technologies,* vol. 4, no. 2, pp. 155-162, 2012.
[52] P. Plantard, E. Auvinet, A.-S. L. Pierres, and F. Multon, "Pose estimation with a kinect for ergonomic studies: Evaluation of the accuracy using a virtual mannequin," *Sensors,* vol. 15, no. 1, pp. 1785-1803, 2015.
[53] T. T. Nguyen, D. C. Slaughter, N. Max, J. N. Maloof, and N. Sinha, "Structured light-based 3D reconstruction system for plants," *Sensors,* vol. 15, no. 8, pp. 18587-18612, 2015.
[54] C. Wang, Z. Liu, and S.-C. Chan, "Superpixel-based hand gesture recognition with kinect depth camera," *IEEE transactions on multimedia,* vol. 17, no. 1, pp. 29-39, 2014.
[55] "Structure Sensor - 3D scanning, augmented reality, and more for mobile devices." [Online]. Available: http://structure.io/files/633/structure.io.html.
[56] P. L. George and E. Seveno, "The advancing-front mesh generation method revisited," *International Journal for Numerical Methods in Engineering,* vol. 37, no. 21, pp. 3605-3619, 1994, doi: 10.1002/nme.1620372103.
[57] "3D CAD Design Software." [Online]. Available: http://www.solidworks.com/ files/350/www.solidworks.com.html.
[58] G. Zhang, Z. Liu, J. Sun, and Z. Wei, "Novel calibration method for a multi-sensor visual measurement system based on structured light," 2010, vol. 49: SPIE, p. 12.
[59] H. Bazargani and R. Laganiere, "Camera calibration and pose estimation from planes," *IEEE Instrumentation & Measurement Magazine,* vol. 18, no. 6, pp. 20-27, 2015/12// 2015, doi: 10.1109/MIM.2015.7335834.
[60] C. Laser, "Green FLEXPOINT® 532 nm - FLEXPOINT® Dot and Line Lasers." [Online]. Available: https://www.lasercomponents.com/us/product/green-flexpoint-532-nm/.
[61] U. o. Minnesota, "Nutrition Data System for Research – Nutritional Analysis Software - ndsr87072 - University of Minnesota Office for Technology Commercialization," 2016/05/02/23:00:33 2016. [Online]. Available: http://license.umn.edu/technologies/ndsr87072_nutrition-data-system-for-research-nutritional-analysis-software.

[62] C. Yang, L. Zhang, H. Lu, X. Ruan, and M.-H. Yang, "Saliency Detection via Graph-Based Manifold Ranking," in *Proceedings of the IEEE Conference on Computer Vision and Pattern Recognition*, 2013 2013, pp. 3166-3173. [Online]. Available: http://www.cvfoundation.org/openaccess/content_cvpr_2013/html/Yang_Saliency_Detection_via_2013_CVPR_paper.html. [Online].

[63] J. Hyyppa, O. Kelle, M. Lehikoinen, and M. Inkinen, "A segmentation-based method to retrieve stem volume estimates from 3-D tree height models produced by laser scanners," *IEEE Transactions on Geoscience and Remote Sensing,* vol. 39, no. 5, pp. 969-975, 2001/05// 2001, doi: 10.1109/36.921414.

[64] L. Zhang, N. Snavely, B. Curless, and S. M. Seitz, "Spacetime faces: High-resolution capture for~ modeling and animation," in *Data-Driven 3D Facial Animation*: Springer, 2008, pp. 248-276.

[65] "*National Diabetes Statistics Report, 2017*," Centers for Disease Control and Prevention, US Department of Health and Human Services, Atlanta, GA, 2017.

[66] A. M. Egan and S. F. Dinneen, "What is diabetes?," *Medicine,* vol. 42, no. 12, pp. 679-681, 2020/02/05 2014, doi: 10.1016/j.mpmed.2014.09.005.

[67] S. L. Lim, K. C. B. Ong, Y. H. Chan, W. C. Loke, M. Ferguson, and L. Daniels, "Malnutrition and its impact on cost of hospitalization, length of stay, readmission and 3-year mortality," vol. 31, no. 3, pp. 345-350, 2012. [Online]. Available: http://www.sciencedirect.com/science/article/pii/S0261561411001993.

[68] "STRUCTURE by OCCIPITAL." https://structure.io/ (accessed 14 March 2020.)

[69] "Autodesk Meshmixer." http://www.meshmixer.com/ (accessed 14 March 2020.)

[70] J. Podolak and S. Rusinkiewicz, "Atomic Volumes for Mesh Completion," in *Symposium on Geometry Processing*, 2005: Citeseer, pp. 33-41.

[71] E. Pérez, S. Salamanca, P. Merchán, and A. Adán, "A comparison of hole-filling methods in 3D," (in English), vol. 26, no. 4, p. 885, 2016, doi: https://doi.org/10.1515/amcs-2016-0063.

[72] W. Zhao, S. Gao, and H. Lin, "A robust hole-filling algorithm for triangular mesh," *The Visual Computer,* vol. 23, no. 12, pp. 987-997, 2007/12/01 2007, doi: 10.1007/s00371-007-0167-y.

[73] "Nutrition Coordinating Center (NCC)." http://www.ncc.umn.edu/ (accessed 4 March 2020.

[74] J. C. Bezdek, L. O. Hall, and L. P. Clarke, "Review of MR image segmentation techniques using pattern recognition," *Medical Physics,* vol. 20, no. 4, p. 4, 1993 1993. [Online]. Available: http://ee.sharif.edu/~miap/Files/MedPhy%201993%20Review%20MR%20Segmentation.pdf.

[75] T. van Lankveld, M. van Kreveld, and R. Veltkamp, "Identifying rectangles in laser range data for urban scene reconstruction," *Computers & Graphics,* vol. 35, no. 3, pp. 719-725, 2011/06// 2011, doi: 10.1016/j.cag.2011.03.004.

[76] Y. J. Zhang, "A survey on evaluation methods for image segmentation," *Pattern Recognition,* vol. 29, no. 8, pp. 1335-1346, 1996/08/01/ 1996, doi: 10.1016/0031-3203(95)00169-7.

[77] A. Banno, T. Masuda, T. Oishi, and K. Ikeuchi, "Flying Laser Range Sensor for Large-Scale Site-Modeling and Its Applications in Bayon Digital Archival Project," (in en), *International Journal of Computer Vision,* vol. 78, no. 2-3, pp. 207-222, 2007/11/22/ 2007, doi: 10.1007/s11263-007-0104-6.

[78] "SELF Nutrition Data." https://nutritiondata.self.com/ (accessed 4 March 2020.

[79] "FatSecret." https://www.fatsecret.com/calories-nutrition/ (accessed 4 March 2020.

[80] S. Faury, M. Koleck, J. Foucaud, K. M'Bailara, and B. Quintard, "Patient education interventions for colorectal cancer patients with stoma: A systematic review," *Patient education and counseling,* vol. 100, no. 10, pp. 1807-1819, 2017.

[81] D. Krasner, "Six steps to successful stoma care," (in eng), *RN,* vol. 56, no. 7, pp. 32-7, Jul 1993. [Online]. Available: http://www.ncbi.nlm.nih.gov/pubmed/8332834.

[82] J. C. Duchesne, Y. Z. Wang, S. L. Weintraub, M. Boyle, and J. P. Hunt, "Stoma complications: a multivariate analysis," (in eng), *Am Surg,* vol. 68, no. 11, pp. 961-6; discussion 966, Nov 2002. [Online]. Available: http://www.ncbi.nlm.nih.gov/pubmed/12455788.

[83] H. C. Benjamin, "Teaching the stoma care routine to a patient with low vision," (in eng), *Br J Nurs,* vol. 11, no. 19, pp. 1270, 1272, 1274-7, Oct 24-Nov 13 2002. [Online]. Available: http://www.ncbi.nlm.nih.gov/pubmed/12419982.

[84] H. Thompson, J. North, R. Davenport, and J. Williams, "Matching the skin barrier to the skin type," (in eng), *Br J Nurs,* vol. 20, no. 16, pp. S27-30, Sep 8-22 2011. [Online]. Available: http://www.ncbi.nlm.nih.gov/pubmed/22096806.

[85] P. Black, "Choosing the correct stoma appliance," (in eng), *Br J Nurs,* vol. 18, no. 4, pp. S10, S12-4, Feb 26-Mar 11 2009. [Online]. Available: http://www.ncbi.nlm.nih.gov/pubmed/19462592.

[86] J. Burch, "Stoma care-related skin problems and solutions," (in eng), *Br J Nurs,* vol. 20, no. 21, p. 1358, Nov 24-Dec 7 2011. [Online]. Available: http://www.ncbi.nlm.nih.gov/pubmed/22241425.
[87] C. Rudoni, "Peristomal skin irritation and the use of a silicone-based barrier film," (in eng), *Br J Nurs,* vol. 20, no. 16, pp. S12, S14, S16 passim, Sep 8-22 2011. [Online]. Available: http://www.ncbi.nlm.nih.gov/pubmed/22096803.
[88] J. Shang, E. Johnson, K. Sundara-Rajan, A. Teredesai, A. Kristal, and A. Mamishev, "Dietary Intake Assessment Using Integrated Sensors and Software," *IS&T/SPIE Electronic Imaging 2012,* 2012 (accepted)
[89] J. Shang *et al.*, "A pervasive Dietary Data Recording System," in *IEEE International Conference on Pervasive Computing and Communications Workshops (PERCOM Workshops)*, 21-25 March 2011 2011, pp. 307-309.
[90] S. Semple, et al., , "Using a new, low-cost air quality sensor to quantify second-hand smoke (SHS) levels in homes," *Tobacco control,* pp. tobaccocontrol-2013-051188, 2013.
[91] Mathworks. "MATLAB - MathWorks." https://www.mathworks.com/products/matlab.html (accessed.
[92] Y. Liu, B. Lan, J. Shirai, E. Austin, C. Yang, and E. Seto, "Exposures to Air Pollution and Noise from Multi-Modal Commuting in a Chinese City," *International journal of environmental research and public health,* vol. 16, no. 14, p. 2539, 2019.
[93] C. A. Pope *et al.*, "Particulate air pollution as a predictor of mortality in a prospective study of US adults," *American journal of respiratory and critical care medicine,* vol. 151, no. 3, pp. 669-674, 1995.
[94] The Qatari Air Quality Monitoring Project. "Air Pollution in Doha, Qatar." https://aqicn.org/country/qatar/ (accessed.
[95] C. A. Pope III and D. W. Dockery, "Health effects of fine particulate air pollution: lines that connect," *Journal of the air & waste management association,* vol. 56, no. 6, pp. 709-742, 2006.
[96] T. Njalsson and I. Novosselov, "Design and Optimization of a Compact Low-cost Optical Particle Sizer," *Journal of Aerosol Science,* 2018.
[97] E. Austin, I. Novosselov, E. Seto, and M. G. Yost, "Laboratory evaluation of the Shinyei PPD42NS low-cost particulate matter sensor," *PloS one,* vol. 10, no. 9, p. e0137789, 2015.
[98] J. Y. He and I. V. Novosselov, "Design and evaluation of an aerodynamic focusing micro-well aerosol collector," (in English), *Aerosol Science and Technology,* vol. 51, no. 9, pp. 1016-1026, 2017/09/02 2017, doi: 10.1080/02786826.2017.1329515.
[99] J. He *et al.*, "Evaluation of micro-well collector for capture and analysis of aerosolized Bacillus subtilis spores," *PloS one,* vol. 13, no. 5, p. e0197783, 2018.
[100] M. Elbayoumi, N. A. Ramli, and N. F. F. Md Yusof, "Spatial and temporal variations in particulate matter concentrations in twelve schools environment in urban and overpopulated camps landscape," *Building and Environment,* vol. 90, pp. 157-167, 8// 2015, doi: http://dx.doi.org/10.1016/j.buildenv.2015.03.036.
[101] M. M. Patel *et al.*, "Spatial and Temporal Variations in Traffic-related Particulate Matter at New York City High Schools," *Atmospheric environment (Oxford, England : 1994),* vol. 43, no. 32, pp. 4975-4981, 2009, doi: 10.1016/j.atmosenv.2009.07.004.
[102] *Directive 2008/50/EC of the European Parliament and of the Council of 21 May 2008 on ambient air quality and cleaner air for Europe,* EU, 2008.
[103] (1997a). *40 CFR Parts 50 - Reference Methods for the Determination of Fine Particulate Matter as PM2.5 in the Atmosphere (Appendix L)*.
[104] A. J. Cohen *et al.*, "Urban air pollution," *Comparative quantification of health risks: global and regional burden of disease attributable to selected major risk factors,* vol. 2, pp. 1353-1433, 2004.
[105] C. S. Fagnant, N. K. Beck, M.-F. Yang, K. S. Barnes, D. S. Boyle, and J. S. Meschke, "Development of a novel bag-mediated filtration system for environmental recovery of poliovirus," (in en), *Journal of Water and Health,* vol. 12, no. 4, pp. 747-754, 2014/12/01/ 2014, doi: 10.2166/wh.2014.032.
[106] N. A. Zhou *et al.*, "Evaluation of the bag-mediated filtration system as a novel tool for poliovirus environmental surveillance: Results from a comparative field study in Pakistan," *PloS one,* vol. 13, no. 7, 2018.
[107] C. S. Fagnant *et al.*, "Improvement of the bag-mediated filtration system for sampling wastewater and wastewater-impacted waters," *Food and environmental virology,* vol. 10, no. 1, pp. 72-82, 2018.
[108] M. Bates, "Tracking Disease: Digital Epidemiology Offers New Promise in Predicting Outbreaks," *IEEE pulse,* vol. 8, no. 1, pp. 18-22, 2017.
[109] K. Touray *et al.*, "Tracking Vaccination Teams During Polio Campaigns in Northern Nigeria by Use of Geographic Information System Technology: 2013–2015," *The Journal of Infectious Diseases,* vol. 213, no. suppl_3, pp. S67-S72, 2016, doi: 10.1093/infdis/jiv493.

[110] V. M. Gammino *et al.*, "Using Geographic Information Systems to Track Polio Vaccination Team Performance: Pilot Project Report," *The Journal of Infectious Diseases,* vol. 210, no. suppl_1, pp. S98-S101, 2014, doi: 10.1093/infdis/jit285.
[111] A. Schriewer *et al.*, "Human and Animal Fecal Contamination of Community Water Sources, Stored Drinking Water and Hands in Rural India Measured with Validated Microbial Source Tracking Assays," *The American Journal of Tropical Medicine and Hygiene,* vol. 93, no. 3, pp. 509-516, 2015, doi: https://doi.org/10.4269/ajtmh.14-0824.
[112] R. C. Andrade, R. K. X. Bastos, P. D. Bevilacqua, and R. V. Andrade, "Cryptosporidium genotyping and land use mapping for hazard identification and source tracking in a small mixed rural–urban watershed in Southeastern Brazil," *Journal of Water and Health,* vol. 17, no. 1, pp. 149-159, 2018, doi: 10.2166/wh.2018.143.
[113] S. Chapman, "Introduction to JavaScript," 2017/09/12/ 2017. [Online]. Available: https://www.thoughtco.com/what-is-javascript-2037921.
[114] Google. "Android Studio and SDK Tools | Android Studio." https://developer.android.com/studio/index.html?gclid=Cj0KCQjwp_DPBRCZARIsAGOZYBSK1CwScvOUtxKcviqd7rNX4wpyOkC4M-CSF8GJm6oCwERFqqf0L4YaAsd2EALw_wcB (accessed.
[115] G. Marshall, "HTML5: what is it?," 2017/09/28/ 2017. [Online]. Available: http://www.techradar.com/news/internet/web/html5-what-is-it-1047393.
[116] E. Barnes, "Laravel 5.4 Is Now Released." [Online]. Available: https://laravel-news.com/laravel-5-4.
[117] K. Lee, "What Is MySQL Workbench?." [Online]. Available: http://smallbusiness.chron.com/mysql-workbench-36016.html.
[118] E. Wurzer, "Why you Should be using PHP's PDO for Database Access," 2012/01/25/ 2012. [Online]. Available: https://code.tutsplus.com/tutorials/why-you-should-be-using-phps-pdo-for-database-access--net-12059.
[119] S. Makhsous. "EESS Validation Map." Easy Map Maker. https://www.easymapmaker.com/map/6db5477e3705bc90b0d474c4785e0cd6 (accessed.
[120] H. M. Mohadisdudis and N. M. Ali, "A study of smartphone usage and barriers among the elderly," in *2014 3rd International Conference on User Science and Engineering (i-USEr)*, 2-5 Sept. 2014 2014, pp. 109-114, doi: 10.1109/IUSER.2014.7002686.
[121] F. Arab, Y. Malik, and B. Abdulrazak, "Evaluation of PhonAge: An Adapted Smartphone Interface for Elderly People," in *Human-Computer Interaction – INTERACT 2013*, Berlin, Heidelberg, P. Kotzé, G. Marsden, G. Lindgaard, J. Wesson, and M. Winckler, Eds., 2013// 2013: Springer Berlin Heidelberg, pp. 547-554.
[122] Y. Hamano and N. Nishiuchi, "Usability Evaluation of Text Input Methods for Smartphone among the Elderly," in *2013 International Conference on Biometrics and Kansei Engineering*, 5-7 July 2013 2013, pp. 277-280, doi: 10.1109/ICBAKE.2013.54.
[123] C. Feng, J. Liang, M. Ren, G. Qiao, W. Lu, and S. Liu, "A Fast Hole-Filling Method for Triangular Mesh in Additive Repair," *Applied Sciences,* vol. 10, no. 3, p. 969, 2020. [Online]. Available: https://www.mdpi.com/2076-3417/10/3/969.